DESIGN, SIMULATION, AND OPTIMIZATION OF AN RGB POLARIZATION INDEPENDENT TRANSMISSION VOLUME HOLOGRAM

by

Adoum Hassan Mahamat

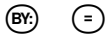

A Dissertation Submitted to the Faculty of the

COLLEGE OF OPTICAL SCIENCES

In Partial Fulfillment of the Requirements
For the Degree of

DOCTOR OF PHILOSOPHY

In the Graduate College

THE UNIVERSITY OF ARIZONA

2016

THE UNIVERSITY OF ARIZONA
GRADUATE COLLEGE

As members of the Dissertation Committee, we certify that we have read the dissertation prepared by Adoum Hassan Mahamat
entitled Design, Simulation, and Optimization of an RGB Polarization Independent Transmission Volume Hologram
and recommend that it be accepted as fulfilling the dissertation requirement for the Degree of Doctor of Philosophy.

James Schwiegerling — Date: 17 December 2015

Yuzuru Takashima — Date: 17 December 2015

Thomas Milster — Date: 17 December 2015

Frank. A. Narducci — Date: 17 December 2015

Date: 17 December 2015

Final approval and acceptance of this dissertation is contingent upon the candidate's submission of the final copies of the dissertation to the Graduate College.
I hereby certify that I have read this dissertation prepared under my direction and recommend that it be accepted as fulfilling the dissertation requirement.

Dissertation Director: James Schwiegerling — Date: 17 December 2015

ACKNOWLEDGEMENTS

Throughout the work of this dissertation, I was truly fortunate to be able to interact with many people that generously helped me technically and professionally. Without their generous support and belief in me, this would not have been possible.

First of all, I would like to thank my joint advisors, Professor J. Schwiegerling, and Dr. F. A. Narducci for their advice and support during this project.

My appreciation is also towards Dr. Frank Narducci for taking his time to advise me through this, despite his busy schedule and to my supervisor Mr. P. Reimel and Mr. Brian Concannon for providing me with this research project.

I would like to acknowledge my committee members Prof. T. Milster, and Prof. Y. Takashima for their dedication and support.

I cannot be thankful enough for my beloved parents, Haoua Mahamat and Hassan Mahamat Souleyman, who have provided me all the emotional support and motivation that I needed to reach this point in my life and for all of my siblings Acham, Iye, and Souleyman.

Last but not least, I gratefully acknowledge the financial support provided to me by the Naval Innovative Science and Engineering (NISE) program (sec 219) to make this work possible.

DEDICATION

This work is dedicated to my entire family, specially my late brother Abouke, sister Mariam, and my wife Terumi.

Contents

Contents – *Continued*

List of Figures

List of Figures – *Continued*

List of Figures – *Continued*

List of Figures – *Continued*

List of Tables

ABSTRACT

Volume phase holographic (VPH) gratings have been designed for use in many areas of science and technology such as optical communication, medical imaging, spectroscopy and astronomy. The goal of this dissertation is to design a volume phase holographic grating that provides diffraction efficiencies of at least 70% for the entire visible wavelengths and higher than 90% for red, green, and blue light when the incident light is unpolarized. First, the complete design, simulation and optimization of the volume hologram are presented. The optimization is done using a Monte Carlo analysis to solve for the index modulation needed to provide higher diffraction efficiencies. The solutions are determined by solving the diffraction efficiency equations determined by Kogelnik's two wave coupled-wave theory. The hologram is further optimized using the rigorous coupled-wave analysis to correct for effects of absorption omitted by Kogelnik's method. Second, the fabrication or recording process of the volume hologram is described in detail. The active region of the volume hologram is created by interference of two coherent beams within the thin film. Third, the experimental set up and measurement of some properties including the diffraction efficiencies of the volume hologram, and the thickness of the active region are conducted. Fourth, the polarimetric response of the volume hologram is investigated. The polarization study is developed to provide insight into the effect of the refractive index modulation onto the polarization state and diffraction efficiency of incident light.

Chapter 1

Introduction

1.0.1 History of Holography

In 1894 Lippmann (Lippmann, 1897) developed a reflection hologram on a photographic plate by interfering a reference wave and a reflected wave coming from a reflector placed behind the photographic plate. Five decades after Lippmann, Gabor (Gabor, 1949) came up with a new technique that includes the principle of reconstruction where his main goal was to developed an imaging method by recording and reconstructing back scattered electrons from a scene. At the time, Gabor recorded his holograms on silver halide, which are highly absorptive materials and significantly reduced the efficiency in the back diffracted orders. Gabor's hologram generated multiple diffraction orders due to the unavailability of coherent illumination sources. In 1962, Denisyuk (Denisyuk, 1963) came up with an improved version of Lippmann's technique by implementing his diffraction process based on Bragg's condition (Bragg, 1912). In his configuration, the signal and reference beams are illuminated in the opposite sides of the recording medium; thus he also generated a reflection hologram.

1.0.2 Volume Holograms in Dichromated Gelatin

In most applications where optical detectors or imaging systems are used, the acquired information is intensity data and does not contain phase information; however propagating waves contain both amplitude and phase information. A volume holo-

gram is a three dimensional record of the amplitude and phase information of an electromagnetic wave within a material. The recording of the phase and amplitude of a wave is done by interfering two coherent waves within the material. The diffraction in a volume hologram is characterized by several factors (Campbell, 1994):

- high diffraction efficiency
- sensitivity to reconstruction wavelength and angular misalignment
- polarization dependence of the diffraction efficiency

Recalling that volume holograms are 3-D records, they need to be recorded in special materials depending on their applications to avoid undesired features into the diffraction orders.These materials are used to record the spatial intensity modulation generated by the interference between the two beams. The spatial intensity modulation is then converted into a refractive index modulation. For that reason the material chosen as recording medium must be controllable in terms of noise and change in material properties.

Dichromated gelatin (DCG) is the preferred material for recording volume holographic grating (Shankoff, 1968; Sheel, 1990). It is homogeneous, flexible, and has spatial resolutions that range between 100 and 5000 lines per millimeter (Newell, 1987). In addition, DCG provides a large refractive index modulation, negligible absorption, and low scattering (Schutte and Stojanoff, 1997). However, due to its flexibility, extra care and control of parameter is needed when making a hologram using DCG thin film. The exposure time, exposure energy, and the chemical development during the fabrication of a volume hologram, may affect the spectral and

angular response, as well as the magnitude of the diffraction efficiency of the final holographic optical element.

1.1 Motivation:

Currently most holographic optical elements are designed based on Bragg's condition (Bragg, 1912) for diffraction. Bragg's condition is the basis of holographic design, and is used to design volume holograms as well as surface relief gratings. Upon use of the Bragg angle to illuminate the hologram with the reference wave, one can reconstruct the signal wave. Furthermore, the diffraction efficiency at different wavelengths can be optimized by just changing the angle of incidence; however the maximum diffraction efficiency is obtained at the Bragg angle, and falls off very fast when away from the Bragg resonance. The quick fall off in the diffraction efficiency away from the Bragg wavelength leads to the need for different volume holograms for different wavelengths, and applications. Thus, the motivation for the topic of this dissertation is driven by two important factors: the design of a single transmission volume hologram that is optimized to increase the percentage of the diffraction efficiencies for wavelengths away from the Bragg wavelength, and the reduction of cost by having a single volume hologram for use in multiple projects to do multiple tasks.

The volume hologram studied in this dissertation is optimized to produce diffraction efficiencies higher than 70% for all wavelengths in the visible spectrum and higher than 90% for the red, green, and blue wavelengths, in the first order of forward diffraction, when the incident wave is unpolarized.

1.2 Outline of the Dissertation:

The work presented in this dissertation is divided into five different chapters. The background and formulation in Chapter 2 provides the necessary information to familiarize the reader with the coupled-wave analyses used to predict the diffraction by volume holograms, and the generalized ellipsometry used to predict the polarization signature of the hologram. This chapter includes the formulation of Kogelnik's two wave coupled-wave analysis (Kogelnik, 1969; Mihaylova, 2013a,b), the formulation of the rigorous coupled-wave analysis (Moharam and Gaylord, 1981; Moharam et al., 1995b,a; Gaylord and Moharam, 1982; Moharam et al., 1981; Gaylord and Moharam, 1981) for the case of an un-slanted transmission volume hologram, and the generalized ellipsometry (Azzam and Bashara, 1974, 1975; de Smet, 1975).

Chapter 3 addresses the design, optimization, and simulation of the spectral and angular response of diffraction efficiencies of the volume hologram using planar diffraction. This chapter goes further into determining the fabrication tolerances needed to be considered in order to produce a hologram that delivers the required diffraction efficiencies.

Chapter 4 presents the holographic optical element's writing process, the experimental data measurement, and a comparison between the measured and simulated diffraction efficiencies. Chapter 5 investigates the polarization signature of the volume hologram, incorporating depolarization effects due to spectral band limitation. The polarization signature of hologram is studied via determination of the coherent Jones-Mueller matrices at each wavelength; and the incoherent Mueller matrix via convolution of the individual Jones-Mueller matrices with a kernel representing the spectral bandwidth of the polarization measurement device.

In the final section, Chapter 6, an outline and description of future work on the design of the volume holographic grating will be discussed. The future work includes the formulation and modeling of the volume hologram based on the interference between a reference plane wave and a spherical signal wave.

Chapter 2

Background Theory and Formulations

2.1 Introduction

Electromagnetic theory is one of most powerful tools used for studying properties of light diffracting through surface relief and volume holographic gratings. It is used in many fields to study propagation and diffraction in different regions of the electromagnetic spectrum. There are several electromagnetic theory models; some of these include the finite element model, the rigorous coupled-wave analysis, and kogelnik's two-wave coupled-wave analysis. However this dissertation will base all its studies on two models, Kogelnik's coupled wave theory (Kogelnik, 1969; Mihaylova, 2013a,b) and the rigorous coupled-wave analysis (RCWA) (Moharam and Gaylord, 1981; Moharam et al., 1995b,a; Gaylord and Moharam, 1982; Moharam et al., 1981; Gaylord and Moharam, 1981). The reason for the use of these two methods is because, Kogelnik's coupled-wave analysis is the simplest and accurate enough, and to our knowledge the RCWA is the most accurate of all. Both theories are derived from Maxwell's equations.

Kogelnik's coupled wave theory is the most commonly used method to predict diffraction efficiencies of volume holographic gratings with 99% accuracy. However, this method does not include the effect of absorption from the cover glasses used to protect the volume hologram's active region from physical damages and humidity. The amplitude of the absorption from the BK7 cover glasses is dependent on wavelength;

since the refractive index of BK7 changes with wavelength in the visible spectrum. Figure 2.1 shows the change of the refractive index of BK7 with wavelength of light in the visible. Another drawback in terms of limitation with this method is the assumption that only two waves propagate, the reference and signal waves.

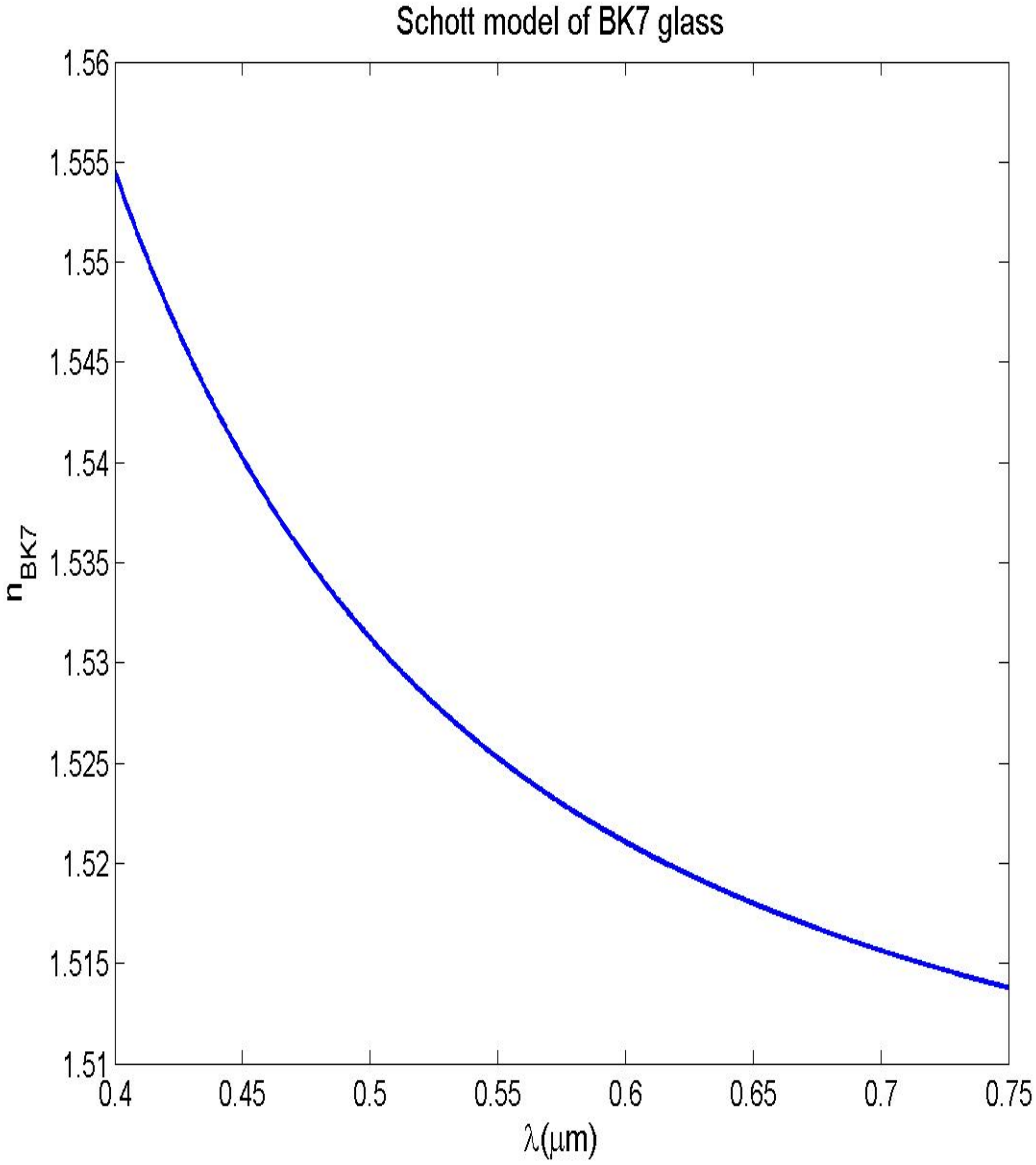

Figure 2.1: The Schott model of refractive index of BK7 glass as a function of wavelength. These values of the refractive index of the BK7 cover glasses were used throughout the entire simulations of the performance of volume hologram.

The most accurate way to predict the electromagnetic properties of light diffracting through a volume hologram is to use the rigorous coupled-wave analysis. The RCWA was introduced by Moharam et al, and since then has been one of the most widely used methods for simulating and predicting the diffraction properties of periodic gratings. This method uses a rigorous formulation which does not make any assumptions to solve Maxwell's electromagnetic equations. The stability and convergence of the RCWA computations to the right diffraction efficiency depend on two factors: the number of harmonic orders in the Fourier series expansion of the field within the active region of the material and the number of propagating diffraction orders.

In this chapter, implementations of the coupled-wave analyses will be derived for the case of planar diffraction. Analyses based on the TE and the TM modes can be derived following the same procedure. The type of volume holographic grating studied and designed in this dissertation is the un-slanted and lossless transmission hologram. This type of holographic grating diffracts light through a spatial modulation of refractive index created via interference of two coherent waves, the reference and signal waves, within an optical material. Typical optical material used for making lossless volume holograms is the dichromated gelatin (DCG).

Section 2 will review Maxwell's equations and the derivation of the wave equation. In section 3, Kogelnik's coupled-wave theory for the case of a transmission un-slanted volume hologram will be reviewed. In section 4, the rigorous coupled wave analysis will be reviewed, following the method of Moharam et al. In section 5, review of the generalized ellipsometry following the method of Azzam and Bashara (*AzzamandBashara*, 1974, 1975; *deSmet*, 1975) will be presented. In the final

section, a conclusion will be derived about the coupled-wave theory.

2.2 Maxwell's Equations and The Wave Equation

Most physical phenomenons inside optical materials can be explained using electromagnetic theory, which begins with Maxwell's equations. These equations are fundamental to all electromagnetic theory and can be used to solve problems in many fields of science and engineering. The equations below are collectively know as Maxwell's equations,

$$\vec{\boldsymbol{\nabla}} \cdot \vec{\boldsymbol{D}} = \rho, \tag{2.1a}$$

$$\vec{\boldsymbol{\nabla}} \times \vec{\boldsymbol{H}} = \vec{\boldsymbol{J}}_{\boldsymbol{free}} + \frac{\partial \vec{\boldsymbol{D}}}{\partial t}, \tag{2.1b}$$

$$\vec{\boldsymbol{\nabla}} \times \vec{\boldsymbol{E}} = -\frac{\partial \vec{\boldsymbol{B}}}{\partial t}, \tag{2.1c}$$

$$\vec{\boldsymbol{\nabla}} \cdot \vec{\boldsymbol{B}} = 0, \tag{2.1d}$$

where:

$\vec{\boldsymbol{H}}$ is the magnetic field $[A/m]$

$\vec{\boldsymbol{E}}$ is the electric field $[V/m]$

$\vec{\boldsymbol{D}} = \epsilon_0 \vec{\boldsymbol{E}} + \vec{\boldsymbol{P}} = \epsilon_r \epsilon_0 \vec{\boldsymbol{E}}$ is the electric displacement $[C/m^2]$

$\vec{\boldsymbol{B}} = \mu_0 \vec{\boldsymbol{H}} + \vec{\boldsymbol{M}}$ is the magnetic induction $[W/m^2 or H.A/m^2]$

$\vec{\boldsymbol{J}} = \sigma \vec{\boldsymbol{E}}$ is the density of free current $[A/m^2]$

σ is the electric conductivity $[\Omega^{-1} m^{-1}]$,

and $\epsilon_0 = 8.8542 \times 10^{-12} F/m$ is the permittivity of free space, ϵ_r is the relative permittivity of the material, $\mu_0 = 4\pi \times 10^{-7} H/m$ is the permeability of free space and μ_r is the relative permeability of the material.

In Maxwell's first equation also known as Gauss' law for the electric field, Equation 2.1a, the density of free charges is denoted by ρ, and $\vec{\boldsymbol{P}}$ is the polarization density in the material media. In free space, $\vec{\boldsymbol{P}} = 0$, therefore $\vec{\boldsymbol{D}} = \epsilon_0 \vec{\boldsymbol{E}}$. In general $\epsilon_0 \vec{\boldsymbol{\nabla}}.\vec{\boldsymbol{E}} = \rho_{total}$ inside a material, where $\rho_{total} = \rho_{free} + \rho_{bound}$. The density of bound charges is given by $\vec{\boldsymbol{\nabla}}.\vec{\boldsymbol{P}} = -\rho_{bound}$.

The second equation, Equation 2.1b, also called Ampere's law, states that any net flow of current into a small volume element is not lost, but results in a change of the local charge density. This statement can be proved by taking the divergence of Maxwell's second equation and rearranging to get the charge continuity.

$$\vec{\boldsymbol{\nabla}}.\vec{\boldsymbol{J}} + \frac{\partial}{\partial t}\left[\vec{\boldsymbol{\nabla}}.\vec{\boldsymbol{D}}\right] = 0. \tag{2.2}$$

Maxwell's third equation, Equation 2.1c, also called Faraday's equation, states that the curl of the $\vec{\boldsymbol{E}}$-field at any location in space and time is exactly equal but opposite in direction to the time derivative of the local $\vec{B}$-field. In this equation $\vec{\boldsymbol{M}}$ is the magnetization density of the material medium. The magnetization is almost always equal to zero, $\vec{\boldsymbol{M}} = 0$, except in ferromagnetic material; therefore, the magnetic density reduces to

$$\vec{\boldsymbol{B}} = \mu_o \vec{\boldsymbol{H}}. \tag{2.3}$$

Maxwell's fourth equation also known as Gauss' law for the magnetism, Equation 2.1d, tells us that whatever $\vec{\boldsymbol{B}}$-field flows into a closed surface, the same amount will

flow out of that surface, so that there is no net flux of $\vec{\boldsymbol{B}}$-field into or out of any closed surface. The lines of the $\vec{\boldsymbol{B}}$-field, therefore, cannot terminate, nor can they originate, at any point in space. This means that there are no sources or sinks for the $\vec{\boldsymbol{B}}$-fields, in other words, there are no magnetic monopoles.

Substituting the expressions for $\vec{\boldsymbol{B}}$,$\vec{\boldsymbol{D}}$, and $\vec{\boldsymbol{J}}$ into Maxwell's third equation, and taking the curl of both sides of the equation, one gets

$$\vec{\boldsymbol{\nabla}} \times \vec{\boldsymbol{\nabla}} \times \vec{\boldsymbol{E}} = -\mu \frac{\partial}{\partial t} \vec{\boldsymbol{\nabla}} \times \vec{\boldsymbol{H}}. \tag{2.4}$$

Now substituting Maxwell's second equation into the right hand side of Equation 2.4 gives

$$\vec{\boldsymbol{\nabla}} \times \vec{\boldsymbol{\nabla}} \times \vec{\boldsymbol{E}} = -\mu\sigma \frac{\partial}{\partial t} \vec{\boldsymbol{E}} - \mu\epsilon \frac{\partial^2 \vec{\boldsymbol{E}}}{\partial t^2}. \tag{2.5}$$

Next we assume that the propagating waves are time dependent and separable. This allows us to write the expression for the first and second time derivatives of the fields as functions of the angular frequency ω and the fields,

$$E(r,t) = Ae^{-j\vec{\boldsymbol{k}}.\vec{\boldsymbol{r}}} e^{j\omega t}, \tag{2.6}$$

where A is a complex amplitude, and $\vec{\boldsymbol{k}}$ is the propagation vector of the plane wave. Replacing the time derivatives of the E-fields with their expressions in Equation 2.5 and re-arranging the right hand side of the expression leads to the wave equation,

$$\vec{\boldsymbol{\nabla}} \times \vec{\boldsymbol{\nabla}} \times \vec{\boldsymbol{E}} - \Upsilon^2 \vec{\boldsymbol{E}} = 0 \tag{2.7}$$

where

$$\Upsilon^2 = -\omega^2\mu\epsilon - j\omega\mu\sigma. \tag{2.8}$$

Throughout this thesis we focus mainly on dichromated gelatin, which can be assumed to be a lossless optical material. Therefore one can say that it has a negligible electric conductivity, i.e. $\sigma \cong 0$. Furthermore, in the case TE polarization, the reference and signal waves are polarized perpendicular to the plane of the grating vector,

$$\epsilon\vec{\boldsymbol{\nabla}}.\vec{\boldsymbol{E}} = 0. \tag{2.9}$$

Expanding the $\vec{\boldsymbol{\nabla}} \times \vec{\boldsymbol{\nabla}} \times \vec{\boldsymbol{E}}$ using properties of curl,

$$\vec{\boldsymbol{\nabla}} \times \vec{\boldsymbol{\nabla}} \times \vec{\boldsymbol{E}} = \vec{\boldsymbol{\nabla}}^2\vec{\boldsymbol{E}} - \vec{\boldsymbol{\nabla}}\left(\vec{\boldsymbol{\nabla}}.\vec{\boldsymbol{E}}\right) \tag{2.10}$$

and substituting Equations 2.8, 2.9, and 2.10 into Equation 2.7, we get the Helmholtz equation,

$$\vec{\boldsymbol{\nabla}}^2\vec{\boldsymbol{E}} - \Upsilon^2\vec{\boldsymbol{E}} = 0. \tag{2.11}$$

Note that in the case of the TM polarization, when the E-field is in the plane of incidence, the gradient of the divergence of the E-field is not always equal to zero. Thus one must use Equation 2.7 rather than Equation 2.11, as the general form of the wave equation.

2.3 Kogelnik's Coupled-Wave Analysis

The type of volume holographic grating investigated in this dissertation is depicted in Figure 2.2. A reference wave with wave vector $\vec{\boldsymbol{k_r}}$ incident at an angle θ_r and

a signal wave with wave vector $\vec{\boldsymbol{k_s}}$ incident at an angle θ_s equal in magnitude and opposite in sign to θ_r, interfere inside the dichromated gelatin dielectric material to generate straight line fringes aligned perpendicular to the direction of the x-axis. As a consequence of the interference between the two coherent waves, a refractive index modulation is created and serves as the periodic structure used to diffract light into different orders. The order at which light is diffracted is related to the wavelength of the two incident waves, the incidence angle of the incoming beam, the average refractive index of the dielectric material and the thickness of the material through the general grating equation. For diffraction to occur light must be incident according to Bragg's condition. The Bragg condition is met when the incidence and diffraction angles are equal but opposite.

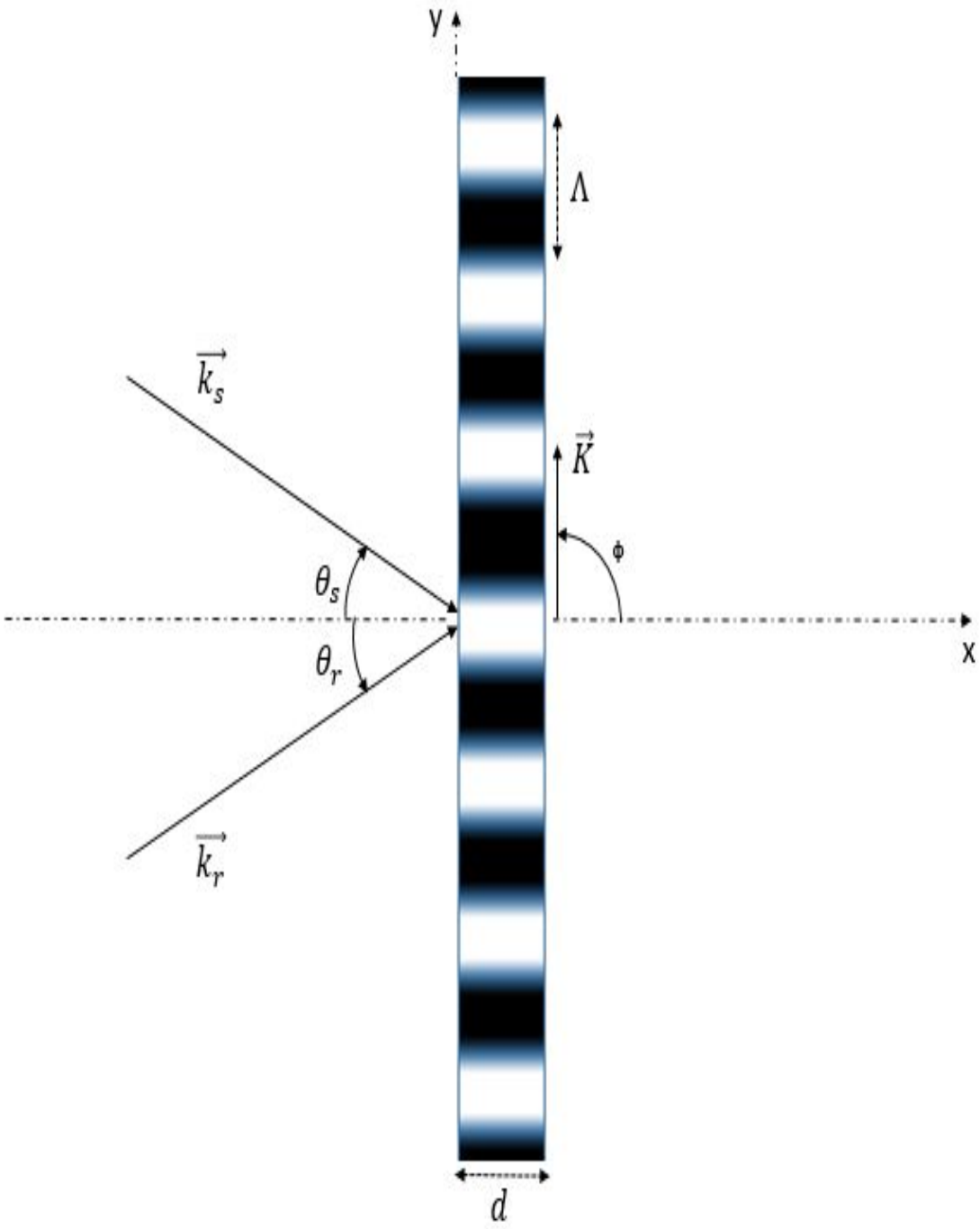

Figure 2.2: Un-slanted Transmission Volume Phase Hologram.

The spatial modulation of permittivity within the active region of the volume hologram is assumed to have a cosinusoidal form, which be can written as

$$\epsilon = \epsilon_{av} + \epsilon_{mod} \cos\left(\vec{\boldsymbol{K}}.\vec{\boldsymbol{r}}\right), \tag{2.12}$$

where ϵ is the permittivity inside the thin film medium, $\epsilon_{av} = \epsilon_0 \epsilon_{r_{av}}$ is the average permittivity, $\epsilon_{mod} = \epsilon_0 \epsilon_{r_{mod}}$ is the modulation permittivity, $\epsilon_{r_{av}}$ and $\epsilon_{r_{mod}}$ are the mean and the amplitude of the modulation of the relative permittivities within the active region of the grating, ϵ_0 is the permittivity of free space, $\vec{\boldsymbol{K}}$ is the grating vector, and $\vec{\boldsymbol{r}}$ is the space vector. The expressions for the grating vector, and the space vector are defined as,

$$\vec{\boldsymbol{K}} = \frac{2\pi}{\Lambda} \left[\hat{x} \cos\left(\phi\right) + \hat{y} \sin\left(\phi\right)\right], \tag{2.13}$$

$$\vec{\boldsymbol{r}} = \hat{x}x + \hat{y}y, \tag{2.14}$$

where Λ is the the period of the grating modulation, and ϕ is the slant angle of the fringe pattern.

Knowing that the fringe patterns within the active region of the grating are aligned along the y-axis, $\phi = \frac{\pi}{2}$, and the fact that the dichromated gelatin has a negligible conductivity, $\sigma = 0$, the expression of Υ of Equation 2.8 becomes,

$$\begin{aligned} \Upsilon^2 &= -\omega^2 \mu \epsilon \\ \Upsilon^2 &= -\omega^2 \mu \epsilon_0 \epsilon_{r_{av}} - \omega^2 \mu \epsilon_0 \epsilon_{r_{mod}} \cos\left(\vec{\boldsymbol{K}}.\vec{\boldsymbol{r}}\right). \end{aligned} \tag{2.15}$$

From the beginning of this chapter up to here, Maxwell's equations, the wave equation, and the profile of the refractive index modulation within the active region of

the volume hologram have been discussed and explained in detail. In the following section, the derivation of the fields in the superstrate, substrate, and grating material, as well as the calculation of the diffraction efficiency for the first order forward diffracted efficiency will be presented.

2.3.1 Diffraction Efficiency: TE Mode

The configuration for this mode is shown in Figure 2.3 below; where the $\vec{\boldsymbol{E}}$-field component of the incident light is perpendicular to the plane of incidence, and $\vec{\boldsymbol{H}}$ field is parallel to the plane of incidence.

Now let us define two parameters, the average propagation vector β, and a coupling constant κ, describing the coupling between the reference and signal waves as,

$$\beta = \omega\sqrt{\mu\epsilon_0\epsilon_{r_{av}}} \tag{2.16}$$

$$\kappa = \frac{1}{4}\frac{\epsilon_{r_{mod}}}{\epsilon_{r_{av}}}\beta. \tag{2.17}$$

Rearranging the right hand side of equation 2.15, yields the expression of Υ^2 as,

$$\Upsilon^2 = -\beta^2 - 4\kappa\beta\cos\left(\vec{\boldsymbol{K}}.\vec{\boldsymbol{r}}\right). \tag{2.18}$$

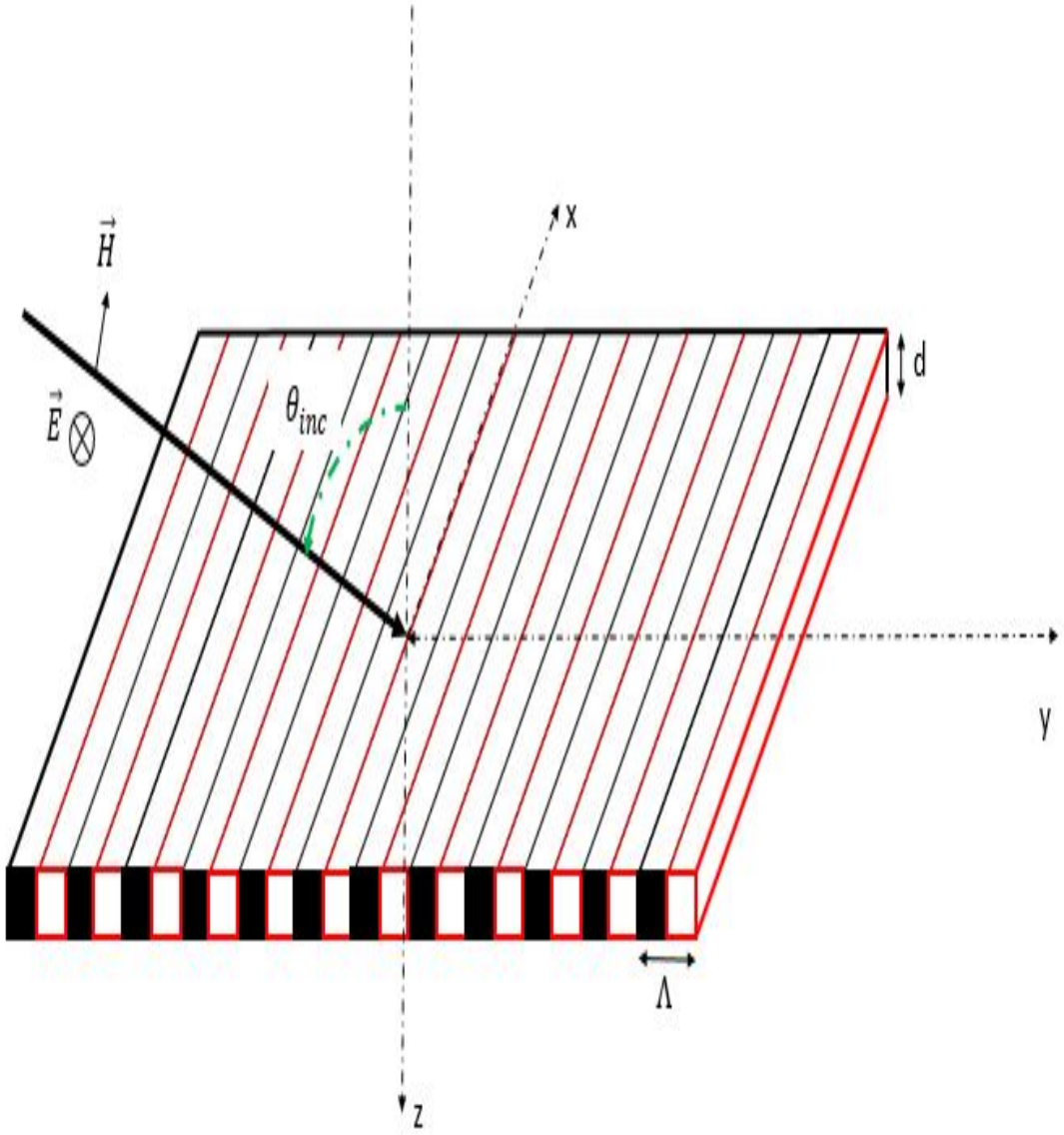

Figure 2.3: Geometry for the volume holographic grating for the case of TE polarization.

When $\kappa = 0$, there is no coupling between the two beams, hence light won't diffract into separate orders. This coupling factor is the main reason for the energy exchange between the reference and signal wave, and leads to the creation of the periodic structure within the active region of the volume hologram. The field generated inside the grating material by this coupling is the superposition of the two waves and is defined as,

$$E_z = R(x)e^{-j\vec{k}_r.\vec{r}} + S(x)e^{-j\vec{k}_s.\vec{r}} \tag{2.19}$$

where R(x) and S(x) are the complex amplitudes of the reference and signal waves. They vary along the x-direction as a result of the exchange of energy between the reference and signal waves. $\vec{k}_r$ and $\vec{k}_s$ are the propagation vectors of the reference and signal waves respectively. When the Bragg condition is met, the propagation vectors are related to the grating vector by

$$\vec{K} = \vec{k}_r - \vec{k}_s, \tag{2.20}$$

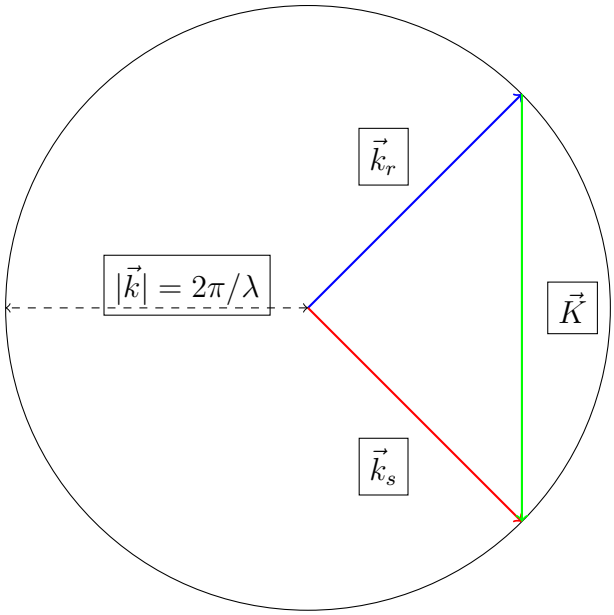

Figure 2.4: Vector relationship between the propagation vectors and the grating vector.

Figure 2.4 depicts the vector relationship between the propagation vectors of the reference and signal waves to the grating vector, at Bragg's incidence. One can also notice that $|\vec{\boldsymbol{k}}| = |\vec{\boldsymbol{k}}_{\boldsymbol{r}}| = |\vec{\boldsymbol{k}}_{\boldsymbol{s}}| = \frac{2\pi}{\lambda}$ when Bragg's condition is met.

Recally Equations 2.11,

$$\frac{\partial^2}{\partial x^2} E_z + \frac{\partial^2}{\partial y^2} E_z - \Upsilon^2 \vec{\boldsymbol{E}} = 0, \tag{2.21}$$

and noting that $\vec{\boldsymbol{k}}_{\boldsymbol{r}} = \hat{x} k_{rx} + \hat{y} k_{ry} + \hat{z} k_{rz}$ and similarly for $\vec{\boldsymbol{k}}_{\boldsymbol{r}}$. Using Equations 2.18, 2.19, and 2.20 and further noting that $k_{rz} = k_{sz} = 0$, one can substitute the equation for the $\vec{\boldsymbol{E}}$-field into Equations 2.11 and rearranged to determine the set of differential equations for solving Kogelnik's two wave coupled wave equations.

$$\left[\frac{\partial^2}{\partial x^2}R - 2jk_{rx}\frac{\partial}{\partial x}R - \left({k_{rx}}^2 + {k_{ry}}^2\right)R\right]e^{-j\vec{k}_r.\vec{r}} + \left[\frac{\partial^2}{\partial x^2}S - 2jk_{sx}\frac{\partial}{\partial x}S - \left({k_{sx}}^2 + {k_{sy}}^2\right)S\right]e^{-j\vec{k}_s.\vec{r}} +$$
$$\beta^2 R.e^{-j\vec{k}_r.\vec{r}} + \beta^2 S.e^{-j\vec{k}_s.\vec{r}} + 4\kappa\beta\cos\left[\left(\vec{k}_r - \vec{k}_s\right).\vec{r}\right]R.e^{-j\vec{k}_r.\vec{r}} +$$
$$4\kappa\beta\cos\left[\left(\vec{k}_r - \vec{k}_s\right).\vec{r}\right]S.e^{-j\vec{k}_s.\vec{r}} = 0$$

$$\left[\frac{\partial^2}{\partial x^2}R - 2jk_{rx}\frac{\partial}{\partial x}R - {k_r}^2 R\right]e^{-j\vec{k}_r.\vec{r}} + \left[\frac{\partial^2}{\partial x^2}S - 2jk_{sx}\frac{\partial}{\partial x}S - {k_s}^2 S\right]e^{-j\vec{k}_s.\vec{r}} +$$
$$\beta^2 R.e^{-j\vec{k}_r.\vec{r}} + \beta^2 S.e^{-j\vec{k}_s.\vec{r}} + 2\kappa\beta\left[e^{-j\left(\vec{k}_r - \vec{k}_s\right).\vec{r}} + e^{j\left(\vec{k}_r - \vec{k}_s\right).\vec{r}}\right]R.e^{-j\vec{k}_r.\vec{r}} +$$
$$2\kappa\beta\left[e^{-j\left(\vec{k}_r - \vec{k}_s\right).\vec{r}} + e^{j\left(\vec{k}_r - \vec{k}_s\right).\vec{r}}\right]S.e^{-j\vec{k}_s.\vec{r}} = 0$$

By grouping equal Fourier components, one can reduce the expression above to

$$e^{-\vec{k}_r.\vec{r}}\left[\frac{d^2R}{dx^2} - 2jk_{rx}\frac{dR}{dx} + 2\beta\kappa S\right] + e^{-j\vec{k}_s.\vec{r}}\left[\frac{d^2S}{dx^2} - 2jk_{sx}\frac{dS}{dx} + 2\beta\kappa R\right]$$
$$+2\beta\kappa S e^{-j(2\vec{k}_s - \vec{k}_r).\vec{r}} + 2\beta\kappa R e^{-j(2\vec{k}_r - \vec{k}_s).\vec{r}} = 0. \tag{2.22}$$

Considering the assumption that only two waves, the reference and the signal, propagate and assuming that $\frac{dS}{dx}$ and $\frac{dR}{dx}$ change much faster than $\frac{d^2S}{dx^2}$ and $\frac{d^2R}{dx^2}$, we can neglect terms, and set the second derivatives to zero,

$$\begin{matrix}\frac{d^2}{dx^2}R = 0 \\ \frac{d^2}{dx^2}S = 0\end{matrix}.$$

Moreover since only two waves propagate, one can assume that the terms in $e^{-j(2\vec{k_r} - \vec{k_s})\cdot\vec{r}}$ and $e^{-j(2\vec{k_s} - \vec{k_r})\cdot\vec{r}}$ can be set to zero as they contribute negligible energies.

By comparison of the terms in $e^{-j\vec{k_r}.\vec{r}}$ and $e^{-j\vec{k_s}.\vec{r}}$, we reduce Equation 2.22 to a system of two linear coupled differential equations in S and R as,

$$\begin{aligned} \frac{k_{rx}}{\beta}\frac{dR}{dx} + j\kappa S = 0 \\ \frac{k_{sx}}{\beta}\frac{dS}{dx} + j\kappa R = 0. \end{aligned} \tag{2.23}$$

From Equation 2.23, one can solve for the expression of first derivatives of the reference and signal waves as functions of the signal and reference waves respectively,

$$\begin{aligned} \frac{dR}{dx} = -j\kappa\frac{S}{\cos(\theta_r)}\frac{\beta}{k_r} \\ \frac{dS}{dx} = -j\kappa\frac{R}{\cos(\theta_s)}\frac{\beta}{k_s}. \end{aligned} \tag{2.24}$$

Taking the derivative of the two differential equations from Equation 2.23, and substitute the expressions from Equation 2.24 into the second order differential equation and noting that $\beta = k_r = k_s$ at Bragg's condition, one gets two uncoupled homogeneous second order differential equations,

$$\begin{aligned} \frac{d^2R}{dx^2} + \frac{\kappa^2}{\cos(\theta_r)\cos(\theta_s)}R = 0 \\ \frac{d^2S}{dx^2} + \frac{\kappa^2}{\cos(\theta_r)\cos(\theta_s)}S = 0. \end{aligned} \tag{2.25}$$

Letting,

$$R(x) = a_1 e^{\psi x} + b_1 e^{-\psi x} \tag{2.26}$$

The expressions in equation 2.25 can be solve using the fact that if $y_1(x)$ and $y_2(x)$ are both solutions to the homogeneous linear equations and a and b are any constants, the linear combination of the individual solutions is also a solution to the homogeneous differential equation. Looking at the homogeneous differential equations, we know

that the exponential function $y = e^{-\psi x}$, where ψ is a constant, has the property that its derivative is proportional to a constant times itself, and its second derivative is proportional to the squared of the constant times the itself.

Applying these theorems to the differential equations from Equation 2.25, we get the characteristic equation for the homogeneous second order differential equation as,

$$\begin{aligned} a_1 r^2 + b_1 r + c_1 = 0 \\ a_2 r^2 + b_2 r + c_2 = 0. \end{aligned} \tag{2.27}$$

For this case the solutions of the characteristic equations are complex, and given as

$$r = \pm j \frac{\kappa}{\sqrt{\cos(\theta_r)\cos(\theta_s)}}. \tag{2.28}$$

So one can write the general solution for the reference and signal waves as,

$$\begin{aligned} R(x) &= c_1 \cos\left[\kappa x \sqrt{\frac{1}{\cos(\theta_r)\cos(\theta_s)}}\right] + c_2 \sin\left[\kappa x \sqrt{\frac{1}{\cos(\theta_r)\cos(\theta_s)}}\right] \\ S(x) &= d_1 \cos\left[\kappa x \sqrt{\frac{1}{\cos(\theta_r)\cos(\theta_s)}}\right] + d_2 \sin\left[\kappa x \sqrt{\frac{1}{\cos(\theta_r)\cos(\theta_s)}}\right] \end{aligned} \tag{2.29}$$

To get the particular solution for the reference and signal waves, we need to introduce the boundary conditions at the interfaces between the superstrate and active region of the hologram.

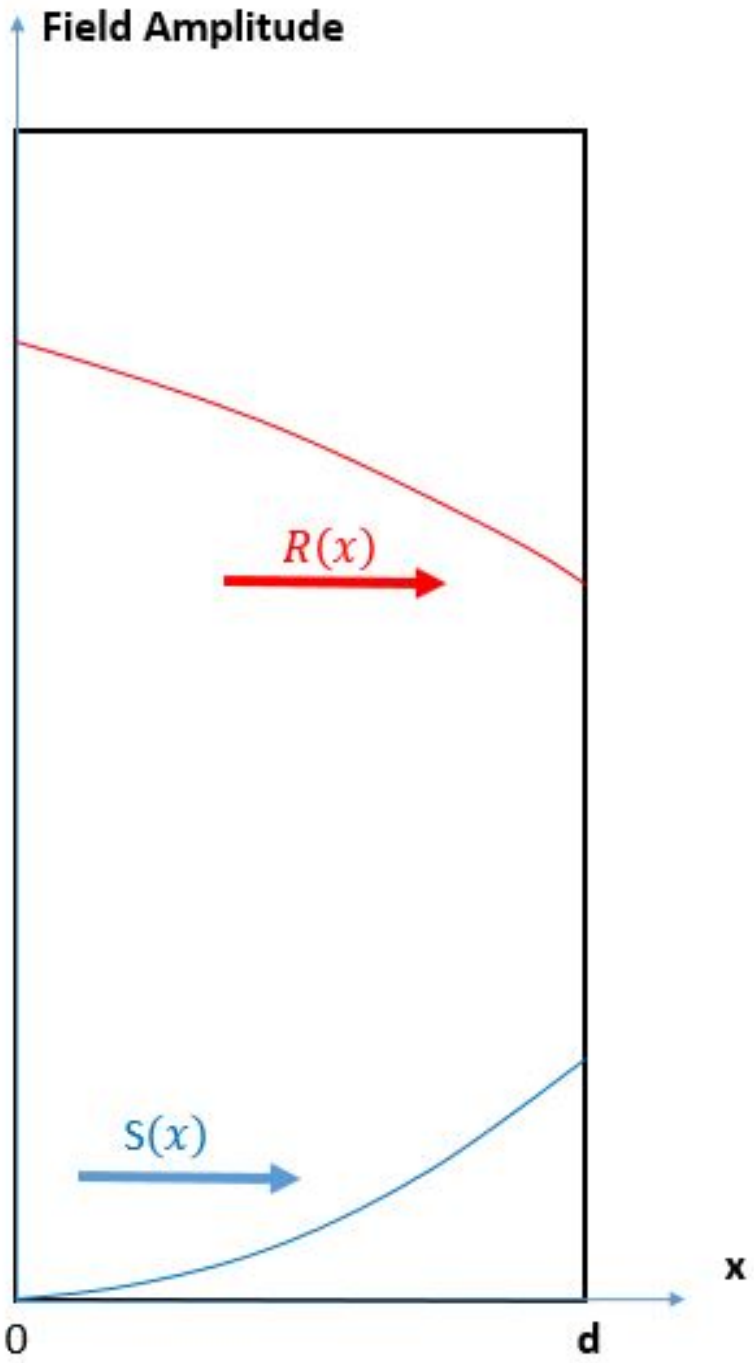

Figure 2.5: Coupling between the reference and signal waves as they propagate through the holographic window.

Figure 2.5 shows that the reference wave starts with maximum amplitude and the signal with minimum amplitude at the interface between the superstrate and the grating material. The reference wave decays as it propagates along the positive direction of the x-axis, and the signal wave gains as it propagates in the same direction (Kogelnik, 1969).

$$\begin{aligned} R(0) &= 1 \\ S(0) &= 0. \end{aligned} \tag{2.30}$$

For simplicity we apply the boundary condition on the general solution of the reference wave to get the particular solution. Then substitute this solution back into the second differential equation from Equation 2.24, to solve for the particular solution for the signal wave. Thus we determine a final solutions as,

$$R = \cos\left[\kappa d\sqrt{\frac{1}{\cos(\theta_r)\cos(\theta_s)}}\right] \tag{2.31}$$

$$S = -j\sqrt{\frac{\cos(\theta_r)}{\cos(\theta_s)}}\sin\left[\kappa d\sqrt{\frac{1}{\cos(\theta_r)\cos(\theta_s)}}\right] \tag{2.32}$$

The main purpose of solving the coupled wave equations is to get to understand the diffraction properties of the un-slanted transmission volume holographic grating. The diffraction efficiency η is the ratio between the incident and diffracted power and is defined as,

$$\eta = \frac{|\cos(\theta_s)|}{\cos(\theta_r)}\left[S(d)\right]\left[S(d)\right]^*, \tag{2.33}$$

where S and R are the amplitudes of the reference and signal waves.

$$\vec{\boldsymbol{k}}_{\boldsymbol{r}} = \frac{2\pi}{\lambda}\left[\hat{x}\cos(\theta_r) + \hat{y}\sin(\theta_r)\right] \tag{2.34}$$

$$\vec{\boldsymbol{k}}_{\boldsymbol{s}} = \frac{2\pi}{\lambda}\left[\hat{x}\left[\cos\left(\theta_r\right) - \frac{2\pi}{\Lambda}\cos\left(\phi\right)\right] + \hat{y}\left[\sin\left(\theta_r\right) - \frac{2\pi}{\Lambda}\sin\left(\phi\right)\right]\right] \tag{2.35}$$

For an un-slanted volume hologram, one can set:

$$\begin{aligned} \phi &= \frac{\pi}{2} \\ \frac{|k_{sx}|}{k_{rx}} &= 1 \\ \cos\left(\theta_s\right) = \cos\left(\theta_r\right) &= \cos\left(\theta\right) \end{aligned}$$

Substituting the values defined for the ratio of the tangential components of the propagation vectors and the azimuth angle into the expression of the diffraction efficiency,

$$\eta_{TE} = \left[-j\sqrt{\frac{\cos\left(\theta_r\right)}{\cos\left(\theta_s\right)}}\sin\left[\kappa d\sqrt{\frac{1}{\cos\left(\theta_r\right)\cos\left(\theta_s\right)}}\right]\right] \cdot \left[-j\sqrt{\frac{\cos\left(\theta_r\right)}{\cos\left(\theta_s\right)}}\sin\left[\kappa d\sqrt{\frac{1}{\cos\left(\theta_r\right)\cos\left(\theta_s\right)}}\right]\right]^{*}, \tag{2.36}$$

and re-arranging and simplifying some terms, leads to the final expression for the diffraction efficiency as

$$\eta_{TE} = \sin^2\left[\kappa\frac{d}{\cos\left(\theta\right)}\right]. \tag{2.37}$$

Note this expression and its equivalent for the case of transverse magnetic at incidence are used to determine the approximate refractive index modulation needed for the design of the RGB volume phase holographic grating. However if an accurate index modulation is needed, one must calculate the refractive index modulation using the rigorous coupled wave analysis (RCWA) rather than Kogelnik's coupled-wave theory. In that case the calculations might get very complicated as the RCWA's solutions depend on the number of diffraction orders considered. The more number of propagating orders considered, the more accurate the solutions.

2.3.2 Diffraction Efficiency: TM Mode

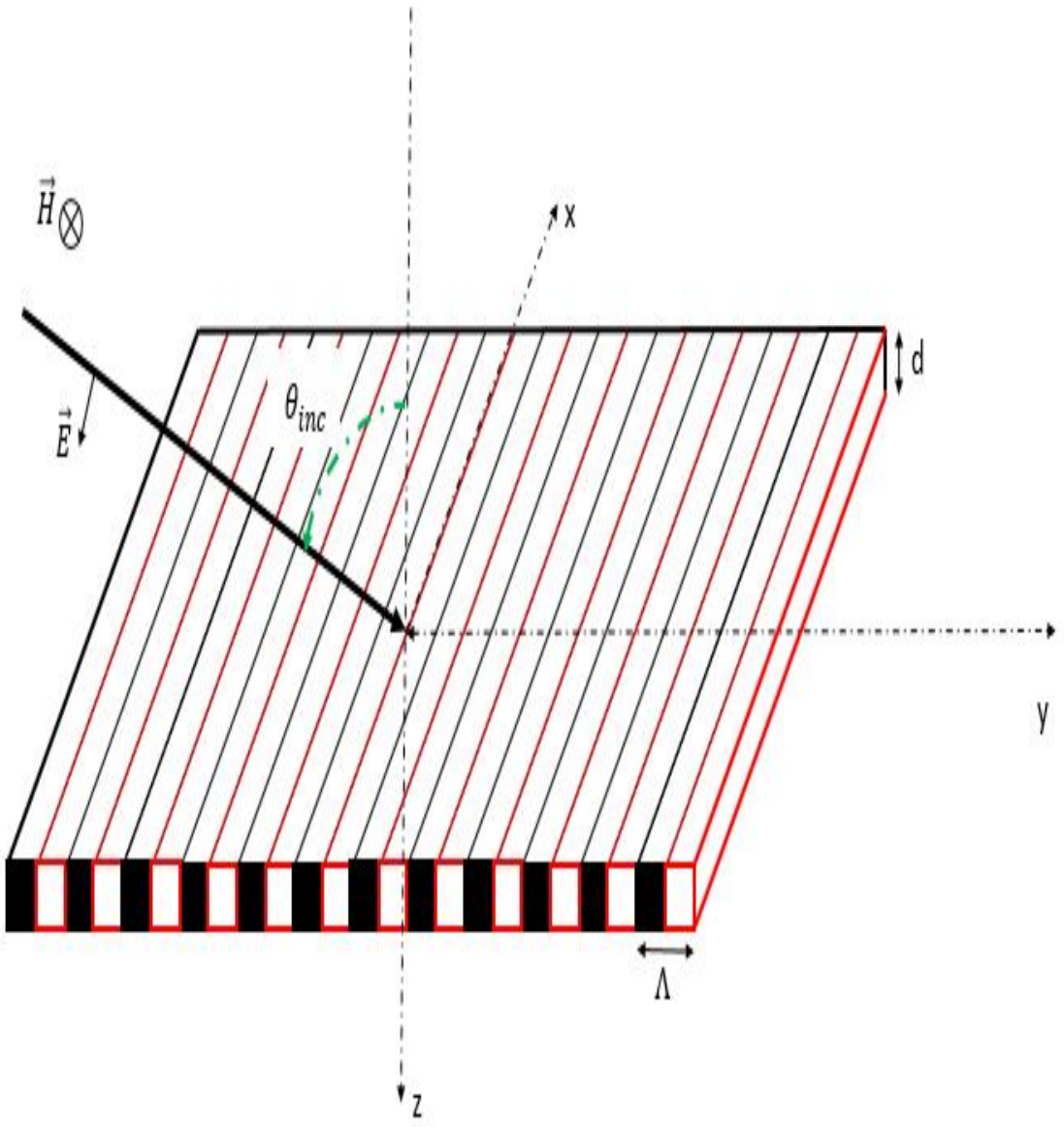

Figure 2.6: Geometry for the volume holographic grating in the case of TM polarization.

Figure 2.6 depicts the configuration for the case when the incident light is polarized in the TM mode. In the case of the transverse magnetic polarization, the electric field is parallel to the plane of incidence, and the magnetic field is perpendicular to the plane incidence. Kogelnik showed in the appendix of his work (Kogelnik, 1969), that using few change of variables one can use the results of the TE polarization to determine the expression of the diffraction efficiency for TM polarization. Most change of variables are related to the change of geometry and the fact that the magnetic field is transverse and both the E and H fields are perpendicular to the propagation vector. Using these assumptions and applying it to the magnetic field version of the wave equation, it can be shown that the new coupling constant has the form,

$$\kappa = -\frac{1}{4}\frac{\epsilon_{mod}}{\epsilon_{av}}\beta\cos(2\theta_r). \tag{2.38}$$

Combining Equations 2.17, 2.37, and 2.38 and rearranging terms,

$$\eta_{TM} = \left[-j\sqrt{\frac{\cos(\theta_r)}{\cos(\theta_s)}}\sin\left[\frac{1}{4}\frac{\epsilon_{mod}}{\epsilon_{av}}\beta\cos(2\theta_r)x\sqrt{\frac{1}{\cos(\theta_r)\cos(\theta_s)}}\right]\right] \cdot \left[-j\sqrt{\frac{\cos(\theta_r)}{\cos(\theta_s)}}\sin\left[\frac{1}{4}\frac{\epsilon_{mod}}{\epsilon_{av}}\beta\cos(2\theta_r)x\sqrt{\frac{1}{\cos(\theta_r)\cos(\theta_s)}}\right]\right]^*,$$

the expression for the diffraction efficiency for the case of TM polarization can be obtained as

$$\eta_{TM} = \sin^2\left[\beta d.\frac{\cos(2\theta_r)}{\cos(\theta_r)}\right]. \tag{2.39}$$

The results for the diffraction efficiencies for the TE and TM modes are used together to generate an approximate diffraction efficiency for the case when the incident

light is unpolarized,

$$\eta_{Unpol} = \frac{1}{2}[\sin^2[\frac{\pi\Delta n_g d}{\lambda\cos(\theta_g)}] + \sin^2[\frac{\pi\Delta n_g d\cos(2\theta_g)}{\lambda\cos(\theta_g)}]]. \tag{2.40}$$

This approximation states that if one averages the two expressions for the diffraction efficiencies from Equations 2.37 and 2.39, the resultant is the diffraction efficiencies for unpolarized light.

2.4 The Rigorous Coupled-Wave Analysis

The rigorous coupled-wave analysis (RCWA) is one of many methods used to solve the diffraction of electromagnetic waves propagating through periodic structures. This method is straightforward and non-iterative and can be used to analyze multilevel structures as well as volume holographic gratings. The RCWA solves for the electromagnetic components of the light diffracted off and through the grating using boundary conditions at the interfaces between the grating material and the superstrate and the substrate. This method solves the exact electromagnetic properties associated with the volume holographic grating by finding solutions that satisfy Maxwell's equations, Equation 2.1, in each of the three regions, the superstrate, the active region, and the substrate, and then match the tangential electric and magnetic field components at the two interfaces. The boundary between the superstrate and the active region forms one interface, and the boundary between the active region and the substrate forms the second interface. Figure 2.7 shows the type of volume holographic grating, an un-slanted transmission hologram, studied in this dissertation. The parameters Λ, and $\vec{\boldsymbol{K}}$ are the period of the refractive index modulation and the grating vector, d is

the thickness of the grating element, θ and θ_3 are the incidence and diffraction angles outside of the grating region.

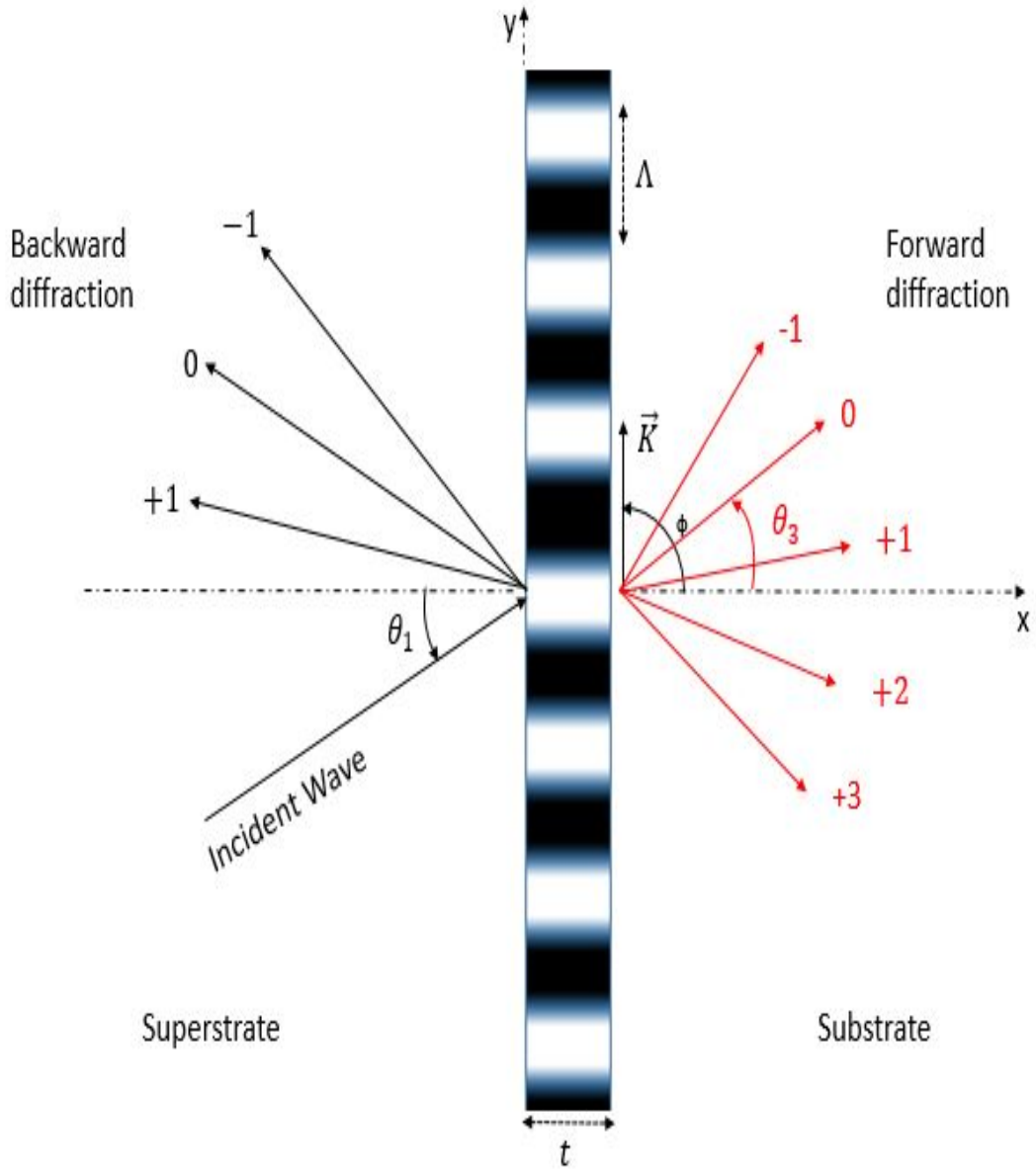

Figure 2.7: Geometry of an unslanted Transmission Volume Phase Hologram including the forward and backward diffracted orders.

The index modulation within the grating material is still considered to have the same cosinusoidal form as described by equation 2.43.

For the purpose of this dissertation, only planar diffraction for lossless material such as the dichromated gelatin is discussed.

2.4.1 RCWA for TE Polarization

This section goes in detail through the implementation of the RCWA model for the case when the incident light is TE polarized; that is when the electric field component of the propagating light is polarized normal to the plane of incidence and the magnetic field lies within the plane of incidence.

For simplicity, the incident light is assuming to be a harmonic plane wave that is separable in time and space. This incident plane wave can be expressed as,

$$\vec{\boldsymbol{E}}_{\boldsymbol{inc}} = \hat{z} e^{-jk_I[x\sin(\theta_I)+y\cos(\theta_I)]}, \tag{2.41}$$

where $k_I = \frac{2\pi}{\lambda_0} n_I$ is the magnitude of the propagation vector in the superstrate, and λ_0 is the wavelength of the incident light in air.

Knowing that the DCG is a dielectric and can be considered to be a lossless material, and assuming that the incident wave is harmonic and separable as in Equation 2.41, one can use the Helmholtz equation, Equation 2.11, to determine the coupled-wave differential equation necessary for solving the diffraction problem.

$$\vec{\boldsymbol{\nabla}}^2 \vec{\boldsymbol{E}} - k^2 \epsilon_r \vec{\boldsymbol{E}} = 0 \tag{2.42}$$

The form of the Helmholtz equation shown in Equation 2.42 is the same as the one

from Equation 2.11 except Υ^2 is reduced to $k^2\epsilon_r$, where ϵ_r is the relative permittivity of the refractive index modulation having the expression as,

$$\epsilon_r = \epsilon_{r_{av}} + \epsilon_{r_{mod}} \cos\left(\vec{\boldsymbol{K}}.\vec{\boldsymbol{r}}\right). \tag{2.43}$$

The transmission un-slanted volume holographic grating is a periodic system and can be described using the Floquet theorem (Collin and Chang, 1960). The Floquet theorem says that at steady state, for each propagating order, the fields at a certain space and time differ from the ones a period away by only a complex constant. The Floquet condition is described by Equation 2.44

$$\vec{\boldsymbol{\Gamma}}_{\boldsymbol{m}} = \vec{\boldsymbol{k}}_{\boldsymbol{g}} - m\vec{\boldsymbol{K}}, \tag{2.44}$$

and reduces to the Bragg's condition when $m = 1$. In Equation 2.44, the $\vec{\boldsymbol{\Gamma}}_{\boldsymbol{m}}$ is the wave vector of the m^{th} order inside the medium, $\vec{\boldsymbol{k}}_{\boldsymbol{g}}$ is wave vector of the 0^{th}, and m is an integer denoting the order number. A proof for the Floquet theorem can be noticed by the fact that if the volume hologram is periodic and infinitely long, one cannot distinguish it from itself by just moving it by a distance equal to its period along the direction of its grating vector (Collin and Chang, 1960).

Due to the periodic nature of the index modulation, the field inside the active region of the volume hologram can be written as a space harmonic using Fourier series as

$$E_g\left(x, y\right) = \sum_{m=-\infty}^{\infty} U_m\left(x\right) e^{-j\vec{\boldsymbol{\Gamma}}_{\boldsymbol{m}}.\vec{\boldsymbol{r}}}, \tag{2.45}$$

where U_m is the amplitude of the m^{th} diffracted wave, and Γ_m is its propagation

vector. Using the geometry shown in Figure 2.7 and simple geometrical projections, the expression for the electric field inside the active region can be re-written as,

$$E_g(x,y) = \sum_{m=-\infty}^{\infty} U_m(x)\, e^{-jk_g[y\sin(\theta_g)+x\cos(\theta_g)]} e^{-jm\vec{\boldsymbol{K}}\cdot\vec{\boldsymbol{r}}} \tag{2.46}$$

where θ_g is the diffraction angle inside the material and can be calculated using Snell's law of refraction,

$$n_I \sin(\theta_I) = n_g \sin(\theta_g). \tag{2.47}$$

The harmonic space coefficients are still unknown and can be calculated simultaneously for all propagating orders, using a second order differential equation deduced from the material properties of the grating, the field inside the active region, and the wave equation.

Substituting the expressions from Equations 2.43 and 2.46 into Equation 2.42 and re-arranging terms, we get

$$\begin{gathered}
\tfrac{\partial^2 E}{\partial x^2} + \tfrac{\partial^2 E}{\partial y^2} + \tfrac{\partial^2 E}{\partial z^2} + k^2\left[\epsilon_{r_{av}} + \epsilon_{r_{mod}}\cos\left(\vec{\boldsymbol{K}}.\vec{\boldsymbol{r}}\right)\right]\vec{\boldsymbol{E}} = 0 \\
\textstyle\sum_{m=-\infty}^{\infty}\{\tfrac{\partial^2 U_m(x)}{\partial x^2} - j2k_g\cos(\theta_g)\tfrac{\partial U_m(x)}{\partial x} - \{[k_g\sin(\theta_g) - mK]^2 - \\
[k_g\cos(\theta_g)]^2\}U_m(x)\}\}.e^{-j\{[k_g\sin(\theta_g)-mK]y+[k_g\cos(\theta_g)]x\}} + \\
k^2\{\epsilon_{r_{av}} + \tfrac{1}{2}\epsilon_{r_{mod}}.e^{j[Ky]} + \tfrac{1}{2}\epsilon_{r_{mod}}.e^{-j[Ky]}\}.\textstyle\sum_{m=-\infty}^{\infty} U_m(x)\, e^{-j\vec{\boldsymbol{\Gamma}}_{\boldsymbol{m}}\cdot\vec{\boldsymbol{r}}} = 0.
\end{gathered} \tag{2.48}$$

The differential equation in 2.48 can be further reduced to Equation 2.49 if one replaces the magnitude of the propagation vectors and the grating vector with their expression as $k = \frac{2\pi}{\lambda}$, $K = \frac{2\pi}{\Lambda}$, and $k_g = \frac{2\pi}{\lambda}\sqrt{\epsilon_{r_{av}}}$.

$$\begin{aligned}&\tfrac{\partial^2 U_m(x)}{\partial x^2} - j\tfrac{4\pi}{\lambda}\cos(\theta_g)\tfrac{dU_m(x)}{dx} - \{\left(\tfrac{2\pi}{\lambda}\right)^2 \epsilon_{r_{av}} \sin^2(\theta_g) + \left(m\tfrac{2\pi}{\Lambda}\right)^2 \\ &\qquad -\tfrac{8\pi^2}{\lambda\Lambda} m\sqrt{\epsilon_{r_{av}}}\sin(\theta_g) + \left(\tfrac{2\pi}{\lambda}\right)^2 \epsilon_{r_{av}} \cos^2(\theta_g)\} U_m(x) \\ &+ \left(\tfrac{2\pi}{\lambda}\right)^2 \epsilon_{r_{av}} U_m(x) + \tfrac{1}{2}\left(\tfrac{2\pi}{\lambda}\right)^2 \epsilon_{r_{mod}} U_{m+1}(x) + \tfrac{1}{2}\left(\tfrac{2\pi}{\lambda}\right)^2 \epsilon_{r_{mod}} U_{m-1}(x) = 0\end{aligned} \tag{2.49}$$

Dividing the entire expression from Equation 2.49 by $2\pi^2$ and re-arranging terms leads to

$$\tfrac{1}{2\pi^2}\tfrac{d^2U_m(x)}{dx^2} - j\tfrac{2}{\pi}\tfrac{\sqrt{\epsilon_{av}}\cos(\theta_g)}{\lambda}\tfrac{dU_m(x)}{dx} + \tfrac{2m(\chi-m)}{\Lambda^2}U_m(x) + \tfrac{\epsilon_{mod}}{\lambda^2}\left[U_{m+1}(x) + U_{m-1}(x)\right] = 0, \tag{2.50}$$

where

$$\chi = \frac{2\Lambda\sqrt{\epsilon_{av}}}{\lambda}\sin(\theta_g). \tag{2.51}$$

The expression for χ can be used to show that if χ is an integer, it reduces to the Bragg condition.

2.4.2 Boundary Conditions

The main purpose of the boundary conditions is to set up the conditions required to help determine the backward and forward diffracted fields for each propagating order. All backward and forward diffracted fields must be phase matched with the fields within the active region of volume hologram. This fact is presented in the form

of equation using Equation 2.52 below.

$$\begin{cases} k_I \sin(\theta_I) = k_g \sin(\theta_g) - mK \\ k_{II} \sin(\theta_{II}) = k_g \sin(\theta_g) - mK \\ k_I \cos(\theta_I) = \sqrt{k_I^2 - [k_g \sin(\theta_g) - mK]^2} \\ k_{II} \cos(\theta_{II}) = \sqrt{k_{II}^2 - [k_g \sin(\theta_g) - mK]^2} \end{cases} \tag{2.52}$$

Furthermore, the boundary conditions required to solve the diffraction problem, require that the tangential components of the fields within the active region of the volume hologram must match those in the substrate and the superstrate as specified by Equation 2.53,

$$\begin{cases} E_{I,z}(0) = E_{g,z}(0) \\ E_{II,z}(d) = E_{g,z}(d) \\ H_{I,y}(0) = H_{g,y}(0) \\ H_{II,y}(d) = H_{g,y}(d). \end{cases} \tag{2.53}$$

The normalized field in the superstrate region is the sum of the incident plane wave and the backward diffracted orders, and it is expressed as,

$$E_{I,z} = e^{-jk_I n_I [y \sin(\theta_I) + x \cos(\theta_I)]} + \sum_{m=-\infty}^{\infty} R_m e^{-j\{[k_g \sin(\theta_g) - mK]y + x\sqrt{k_I^2 - [k_g \sin(\theta_g) - mK]^2}\}}; \tag{2.54}$$

whereas, the normalized field in the substrate is a Fourier series sum of all the forward diffracted orders, and can be expressed as,

$$\vec{\boldsymbol{E}}_{\boldsymbol{II,z}} = \sum_{m=-\infty}^{\infty} T_m e^{-j\{[k_g \sin(\theta_g) - mK]y + (x-d)\sqrt{k_{II}^2 - [k_g \sin(\theta_g) - mK]^2}\}}. \tag{2.55}$$

In Equations 2.54 and 2.55, R_m is the amplitude of the m_{th} order backward diffracted wave, and T_m is the amplitude of the m_{th} order forward diffracted wave.

In this case, since the $\vec{\boldsymbol{E}}$-field is polarized normal to the incidence plane, it only has a component along the z-direction, $(0, 0, E_z)$. The $\vec{\boldsymbol{H}}$-field has two components, one in the tangential direction and another one along the normal. Using Equation 2.1c, one can determine the expression for the tangential component of the magnetic field as functions of the $\vec{\boldsymbol{E}}$-field.

$$\begin{vmatrix} \hat{x} & \hat{y} & \hat{z} \\ \frac{\partial}{\partial x} & \frac{\partial}{\partial y} & \frac{\partial}{\partial z} \\ 0 & 0 & E_z \end{vmatrix} = \hat{x}\frac{dE_z}{dy} - \hat{y}\frac{dE_z}{dx} \tag{2.56}$$

Knowing that the fields are harmonic and separable in time and space, and combining Equations 2.56 and 2.1c, and re-arranging, the expression for components of the magnetic field are obtained as,

$$\begin{cases} H_x = -j\frac{1}{\mu\omega}\frac{dE_z}{dy} \\ H_y = j\frac{1}{\mu\omega}\frac{dE_z}{dx} \end{cases} \tag{2.57}$$

where H_x and H_y are the components of the magnetic field along the normal and tangential to the surface of the volume hologram.

Considering the phase matching and the boundary condition, Equations 2.46, 2.53, 2.54, 2.55, and 2.57 can be combined together to determine a system of four equations,

$$\begin{cases} \delta_{m0} + R_m = U_m(0) \\ j\sqrt{k_I^2 - [k_g \sin(\theta_g) - mK]^2}\,[R_m - \delta_{m0}] = \frac{d}{dz}U_m(0) \\ T_m = U_m(d)e^{-jk_g d\cos(\theta_g)} \\ j\sqrt{k_{II}^2 - [k_g \sin(\theta_g) - mK]^2}T_m = \left[jk_g \cos(\theta_g)U_m(d) - \frac{d}{dz}U_m(d)\right].e^{-jk_g d\cos(\theta_g)} \end{cases} \tag{2.58}$$

that can be solved to calculate all the amplitudes of the backward and forward diffracted orders. In Equation 2.58, the symbol δ_{m0} is the Kronecker delta function, and takes a value of unity when $m = 0$ and zero otherwise.

So far in the formulation of the rigorous coupled-wave analysis, we set up the phase matching between the phases, the boundary condition, and we determined the expressions for the fields in the three regions. In the next section, the diffraction efficiency for the first order forward diffraction will be calculated.

2.4.3 Diffraction Efficiency

Although the entire derivations in the previous sections of this chapter were done to determine the fields in all three regions, the most important thing for us in the field of holographic element design is the diffraction efficiency, which is the ratio of the intensity of the diffracted order to the intensity of the incident field. Since the volume hologram studied in this dissertation is a transmission hologram, we are only

interested in the diffraction efficiency of the forward diffracted orders. Equation 2.59,

$$\eta_{T_{TE},m} = \begin{cases} \frac{\sqrt{\left[\frac{n_{II}}{n_I}\right]^2 - \left[\sin(\theta_I) - \frac{m\lambda_0}{n_I \Lambda}\right]^2}}{\cos(\theta_I)} R_m R_m^* \\ -j\frac{\sqrt{\left[\frac{n_{II}}{n_I}\right]^2 - \left[\sin(\theta_I) - \frac{m\lambda_0}{n_I \Lambda}\right]^2}}{\cos(\theta_I)} R_m R_m^* \end{cases} \tag{2.59}$$

is the general equation for the diffraction efficiency for the case when the incident light is TE polarized.

2.4.4 RCWA for TM Polarization

For TM polarized incident wave, the $\vec{\boldsymbol{H}}$-field is polarized perpendicular to plane of incidence. The same formulation as the case of TE polarization is used; however in this diffraction problem, the $\vec{\boldsymbol{H}}$-field is expressed as a Fourier sum, then the $\vec{\boldsymbol{E}}$-field components are determined from Maxwell's equations. Following the same steps and noting that the divergence of the electric field is no longer zero, one can successful derive the expression for the diffraction efficiency in this mode.

2.5 Review of Polarization

2.5.1 Introduction

The last few sections focused more on the determination of the expression for the electric and magnetic fields inside and outside of the grating material, as well as the diffraction efficiencies of the forward and backward diffracted lights; however in order to have a complete optical characterization of the volume hologram, it very useful to have an understanding of it polarization signature. This is the volume hologram's property that changes the orientation of the electric field component of

incident light as it diffracts through the holographic optical element. The polarization of light specifies the direction of oscillation of its electric field component; however the polarization signature of a material is its ability to alter the polarization state of light. This property of the transmission volume hologram can be described by 2×2 Jones matrices, which are matrices that relate the polarization states of the incident and diffracted waves for individual wavelength. The Jones matrix can be used to describe coherent light. Another polarization metric that can be used to describe both coherent and incoherent light, is the Mueller matrix.

As defined earlier in sections 3 and 4, the transmission volume hologram's active region is made of periodic cosinusoidal modulation of refractive indices. The refractive index modulation can be viewed as a multiple layers composite of isotropic materials arranged in a lamellar structure. The periodic structure and the combination of multiple isotropic materials would constitute a new meta-material that behaves as an anisotropic material, which exhibits an artificial birefringence property called the form birefringence (Born and Wolf, 1970; Yeh et al., 1977; Yariv and Yeh, 1977; Rytov, 1956). A form birefringence rise from the anisotropy created by the arrangement of isotropic materials who's sizes are smaller than the wavelength of light and larger than molecules (Born and Wolf, 1970).

In the next two sections, a description of the coherent Mueller matrix characterization, as well as the depolarization properties of the holograms that can be incorporated in the coherent Mueller matrix to produce a quasi-incoherent Mueller matrix will introduced.

2.5.2 Coherent Mueller Matrix of the Volume Hologram

In section 2.4 of this chapter, we talked about the rigorous coupled wave analysis and its commercial model, GSolver, that was used throughout the design and simulations of the volume hologram. The RCWA determines the complex reflection and transmission coefficients for the forward and backward diffraction orders by solving an eigenvalue problem dependent on the several parameters including the propagating orders; however for the purpose of this dissertation, we are only interested in the first order of forward diffraction. Assuming that the incoming plane wave has a known polarization state, the phase and amplitude of the transmitted coefficients of the first order of diffraction can be used to calculated the Jones matrix,

$$\boldsymbol{J} = \begin{bmatrix} t_1 e^{j\Psi_1} & t_{ps} \\ t_{sp} & t_2 e^{j\Psi_2}, \end{bmatrix} = \begin{bmatrix} T_{pp} & T_{ps} \\ T_{sp} & T_{ss} \end{bmatrix}, \tag{2.60}$$

which relates the incoming Jones vector to the diffracted Jones vector. In Equation 2.60, t_1 and t_2 are the amplitudes of the transmission coefficients for the TE and TM polarizations respectively, and Ψ_1 and Ψ_2 are their respective phases; whereas t_{sp} and t_{ps} are the transmission coefficients that mark the anisotropic property of the volume hologram. The non-diagonal elements, t_{sp} and t_{ps}, of the Jones matrices can be calculated using general ellipsometry (Azzam and Bashara, 1974, 1975; de Smet, 1975). Equation 2.61 shows how the Jones matrix relates the incident and diffracted $\vec{\boldsymbol{E}}$-field; where the 2x2 matrix represents the Jones matrix of the Transmission Volume hologram, the column vector on the left hand side is the Jones vector representing the diffracted $\vec{\boldsymbol{E}}$-field, and the column vector on the right hand side is the Jones vector

representing the incident $\vec{\boldsymbol{E}}$-field.

$$\begin{bmatrix} E_{tp} \\ E_{ts} \end{bmatrix} = \begin{bmatrix} T_{pp} & T_{ps} \\ T_{sp} & T_{ss} \end{bmatrix} \cdot \begin{bmatrix} E_{ip} \\ E_{is} \end{bmatrix} \tag{2.61}$$

In order to use generalized ellipsometry to determine these elements, one needs to consider at least three different states of polarization for the incident waves,with ellipses of polarization $(\chi_{i1}, \chi_{i2}, \chi_{i3})$. After diffraction through the volume hologram, the diffracted waves will have their own states of polarization, with ellipses of polarization $(\chi_{r1}, \chi_{r2}, \chi_{r3})$, as well. One can calculate the polarization ellipses of the incident and reflected light using Equations 2.62 and 2.63 respectively,

$$\chi_i = \frac{E_{is}}{E_{ip}} \tag{2.62}$$

$$\chi_t = \frac{E_{ts}}{E_{tp}} \tag{2.63}$$

By expanding the expression of Equation 2.61 into a linear system of two equations and eliminating the ratios $\frac{E_{is}}{E_{ip}}$, and $\frac{E_{ts}}{E_{tp}}$, the system can be reduced to a single equation given by the expression of Equation 2.64,

$$\chi_t = \frac{T_{ss}\chi_i + T_{sp}}{T_{ps}\chi_i + T_{pp}} \tag{2.64}$$

Considering three sets of incident polarizations and their respective diffracted polarizations states into Equation 2.64, the ratios of the elements of the 2x2 matrix in

Equation 2.60 can be calculated using Equations 2.65 through 2.68

$$\frac{T_{pp}}{T_{ss}} = \frac{\chi_{12} - \chi_{i1}H}{\chi_{t2}H - \chi_{t1}} \tag{2.65}$$

$$\frac{T_{ps}}{T_{ss}} = \frac{H - 1}{\chi_{t2}H - \chi_{t1}} \tag{2.66}$$

$$\frac{T_{sp}}{T_{ss}} = \frac{\chi_{i2}\chi_{t1} - \chi_{t2}\chi_{i1}H}{\chi_{t2}H - \chi_{t1}} \tag{2.67}$$

$$H = \frac{(\chi_{t3} - \chi_{t1})(\chi_{i1} - \chi_{i2})}{(\chi_{t3} - \chi_{t2})(\chi_{i3} - \chi_{i1})} \tag{2.68}$$

The 2×2 matrix of Equation 2.60 describes the transformation of the the field vectors; however in order to describe the intensity of the light, which is what detectors measure, one needs to determine a Mueller matrix that relates the intensities. The input intensity polarization data is related to the output intensity polarization data through a 4×4 Mueller matrix that describes how the transmission volume hologram is changing the polarization state of incoming light, and is calculated using equation 2.69 (Azzam and Bashara, 1977; Azzam, 1986),

$$M_{VPH} = \begin{bmatrix} M_{00} & M_{01} & M_{02} & M_{03} \\ M_{10} & M_{11} & M_{12} & M_{13} \\ M_{20} & M_{21} & M_{22} & M_{23} \\ M_{30} & M_{31} & M_{23} & M_{33} \end{bmatrix} = A * \mathbf{KP}\{J_{VPH}, J^*_{VPH}\} * A^{-1}, \tag{2.69}$$

where **KP** represents the Kronecker product of the Jones matrix, and A is a 4x4

matrix given by

$$A = \begin{bmatrix} 1 & 0 & 0 & 1 \\ 1 & 0 & 0 & -1 \\ 0 & 1 & 1 & 0 \\ 0 & j & -j & 0 \end{bmatrix}. \tag{2.70}$$

2.5.3 Depolarization Properties of the Volume Hologram

Depolarization is a process that couples polarized light into unpolarized light and it is intrinsically related to scattering, diattenuation, and retardance that vary with time and wavelength. One way to investigate the depolarization property of the volume holographic gratings is to determine its band averaged Mueller matrix that will serve as an incoherent Mueller matrix that can be used to check for its depolarization level. This can be done by first calculating the coherent Mueller matrices for several wavelengths within the chosen waveband and then summing them to find the incoherent Mueller matrix. A necessary and sufficient condition for a physically realizable Mueller matrix to represent a non-depolarizing optical system was determined by (Gil and Bernabeu, 1985) and given as,

$$\sqrt{\mathbf{Tr}\left[M^T M\right]} = \sum_{a,b}^{3} M_{ab}^2 = 4M_{00}^2 \tag{2.71}$$

where **Tr** is the trace function, which is defined as the sum of the diagonal elements of the matrix M.

The depolarization associated with the transmission volume hologram can be calculated using the elements of a newly created, incoherent Mueller matrix. The quantity that determines the depolarization of the first order forward diffracted light is

called the depolarization index, and is it is expressed as,

$$P_D(M) = \sqrt{\frac{\sum_{a,b} M_{ab}^2 - M_{11}^2}{3M_{11}^2}}, \tag{2.72}$$

where $P_D(M)$ takes values ranging from 0 (perfect depolarizer) to 1 (non-depolarizing). The depolarization effects in the optical response of the volume holographic gratings can be classified into two groups, the intrinsic and extrinsic depolarization properties. The intrinsic depolarization properties come from surface non-uniformities of the active region of the gratings, and the transparencies of the BK7 cover glasses. On the other hand, the extrinsic depolarization properties come from imaging system used to collect data. The most common sources of extrinsic depolarization are imperfection of optical elements, and the finite numerical aperture of the focusing lens.

The depolarization effects that are introduced by surface non-uniformities, hence thickness variations, can be determined as the sum of the product between the non-depolarizing Mueller matrices $\boldsymbol{M}$ and the corresponding thickness distribution $\mathbf{T}$, and is given as

$$\boldsymbol{M_t} = \int \mathbf{T}(\mathbf{t_o} - \mathbf{t})\boldsymbol{M}(\boldsymbol{t})dt. \tag{2.73}$$

On the other hand, one can calculated the incoherent Mueller matrix containing the depolarization properties induced by finite numerical aperture of the imaging system as

$$\boldsymbol{M_{NA}} = \frac{1}{\pi r^2} \int\int \boldsymbol{M}(\boldsymbol{\theta}, \boldsymbol{\phi}) d\theta d\phi, \tag{2.74}$$

and the incoherent Mueller matrix containing the depolarization properties induced

by the finite bandwidth of the imaging system as

$$\boldsymbol{M_\lambda} = \int \mathbf{w}(\boldsymbol{\lambda_0} - \boldsymbol{\lambda})\boldsymbol{M}(\boldsymbol{\lambda})d\lambda, \tag{2.75}$$

where $\boldsymbol{M(\theta, \phi)}$ is the non-depolarizing Mueller matrix, θ is the angle of incidence, ϕ is the azimuthal angle, C is the exit pupil of the imaging system, and $\mathbf{w}(\boldsymbol{\lambda})$ is its spectral bandwidth function. This method of incorporating the depolarization properties into the coherent Mueller matrices results from the fact that polarimetric imaging systems tend to average over some bandwidths. Those imaging devices do not know how to separate individual wavelengths, angles, or thicknesses; they always average over a limited bandwidth.

2.6 Conclusion

In this chapter most of the theory behind the design, simulation, and characterization of a transmission volume hologram were presented. The formulations of the diffraction efficiencies using the two-wave coupled wave analysis(Kogelnik, 1969) and the rigorous coupled wave analysis (Moharam and Gaylord, 1981; Moharam et al., 1995b,a; Gaylord and Moharam, 1982; Moharam et al., 1981; Gaylord and Moharam, 1981) were presented, as well as the method of generalized ellipsometry (Azzam and Bashara, 1974, 1975; Azzam, 1986; Azzam and Bashara, 1977). We also talked about the two main factors of depolarization, the intrinsic and extrinsic factors. Thus chapter introduces all the tools needed to design and characterize a volume holographic phase grating.

Chapter 3

Design, Optimization, and Simulation

3.1 Introduction

In this chapter, a complete description of the design parameters as well as the simulation of the diffractive behavior of the volume hologram are presented. Using results of the derivations from Chapter 2, a commercial package of the RCWA model (G-Solver), one can determine the architectural design parameters for the transmission volume holographic grating, as well as its first order forward diffracted efficiencies. Most parameters are determined using the results of Kogelnik's coupled wave analysis and the Bragg condition; however the final diffraction efficiencies, and the spectral and angular bandwidths for the $460nm$, $532nm$, and $532nm$ design wavelengths are calculated from the RCWA for accuracy and consistency with experimental results. All results shown in this section are calculated for the case when the incident light is unpolarized. In this dissertation, the diffraction efficiency for the case when incident light is unpolarized, is approximated as the average between the diffraction efficiencies for transverse electric (TE), and transverse magnetic (TM) polarizations.

In recent years, interest in the use of volume phase holographic gratings have grown in several fields of optics, photonics, and astronomy (Wakayama et al., 2013; Barden et al., 1998; Bianco et al., 2012; Arns and Dekker, 2008). Although, volume holograms can be recorded on several materials, dichromated gelatin (DCG) is the preferred material due its high-efficiency for both 2-D and 3-D gratings with low noise

(Shankoff, 1968; Newell et al., 1985; Chang and Leonard, 1979; Baldry et al., 2004; Blanche et al., 2004). Baldry et al. (2004) derived a tuning parameter from Kogelnik's efficiency equations (Kogelnik, 1969) for determining the index modulation needed for obtaining high efficiency with unpolarized light; however they did not consider the simultaneous optimization for blue, red, and green wavelengths. This chapter discusses the design and optimization of a volume phase hologram for simultaneous use with red, green, and blue wavelength when unpolarized light is incident. The optimization of this volume hologram is done using Kogelnik's method (Kogelnik, 1969) and the rigorous-coupled wave analysis (Moharam and Gaylord, 1981; Moharam et al., 1995b,a).

Section 2 will discuss Bragg diffraction and volume hologram physics, section 3 defines the optimization process, section 4 will present the simulation of the volume phase hologram, section 5 will talk about the fabrication tolerances, and section 6 will give a closing conclusion about the design.

3.2 Bragg Diffraction and Volume Hologram Physics

Volume phase holograms are diffractive optical elements which diffract light using a modulation of refractive index within the active region of the grating. The average refractive index modulation n_g, within the active region of the grating is approximated to have a cosinusoidal structure and it is defined by,

$$n_g = n_o + \Delta n_g \cos(\frac{2\pi x}{\Lambda}) \tag{3.1}$$

where n_o is the average index of refraction of DCG, Δn_g is the index modulation, and Λ is the period of the index modulation. The index modulation is created by interfering two beams within the active region of the volume hologram. The orientation of the index modulation is determined by the direction of propagation of the two interfering beams. The main topic of this chapter is the design of a transmission volume phase hologram for simultaneous use with red, green, and blue light. The volume hologram is recorded on a $12\mu m$ thick DCG film. The refractive index modulation created within the DCG has an average refractive index $n_o = 1.5$ and an index modulation $\Delta n = 0.022$. The design is then optimized for unpolarized blue, green, and red light with wavelengths $460nm$, $532nm$, and $632nm$ respectively.

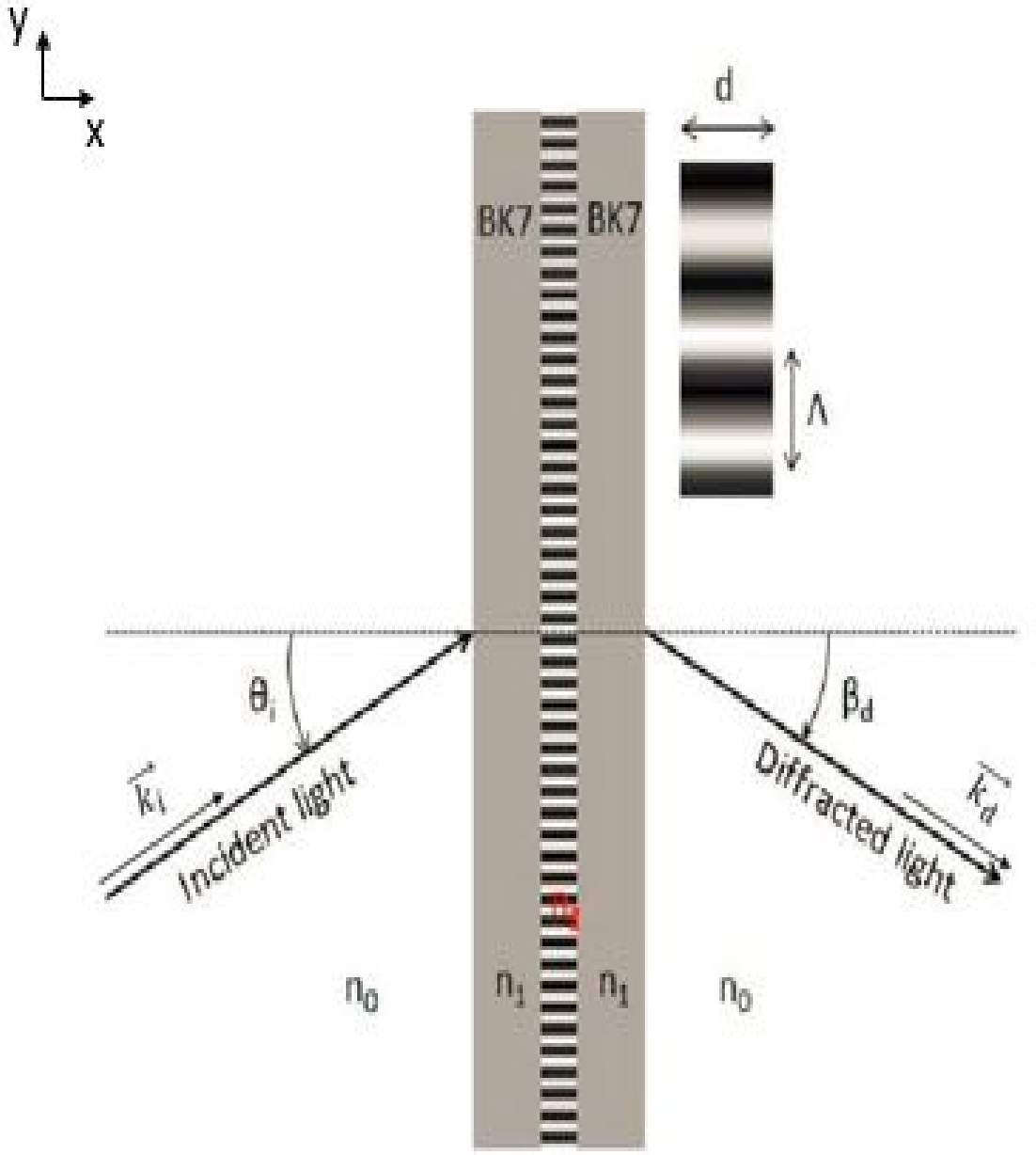

Figure 3.1: Un-slanted Transmission Volume Phase Hologram.

Figure 3.1 shows the type of volume holographic grating, an un-slanted transmission volume hologram, that is used throughout this chapter.

Bragg's condition in conjunction with the classical grating equation enable the calculation of the incidence angle desired to diffract light into any specific orders. Light incident at Bragg's angle gets diffracted, and all other incidence angles get transmitted through without being diffracted. The design and optimization in this chapter is done for the first order of diffraction.

The classical grating equation for transmission is given by:

$$k_i \sin(\theta_i) + k_d \sin(\beta_d) = \frac{2\pi m}{\Lambda} \tag{3.2}$$

where $\overrightarrow{k_i}$ and $\overrightarrow{k_d}$ are the propagation vectors for the incident and diffracted lights and where $k_i = |\vec{\boldsymbol{k_i}}|$ and $k_d = |\vec{\boldsymbol{k_d}}|$, θ_i is the incidence angle in air, β_d is the diffraction angle in air, and m is the order of diffraction.

The Bragg condition is met when the incidence and diffraction angles are equal but opposite. Using this condition, Equation 3.2 can be re-written as,

$$m\lambda = 2\Lambda \sin\theta_i. \tag{3.3}$$

In order to ensure the accuracy of the design, two methods, Kogelnik's couple-wave analysis (Kogelnik, 1969) and the rigorous-coupled wave analysis (RCWA) (Moharam and Gaylord, 1981; Moharam et al., 1995b,a), are used in parallel to calculate the theoretical diffraction efficiencies. Although Kogelnik's equations are the most often used equations to calculate the 1st order diffraction efficiencies of volume holograms,

they fail to include the effects of absorption from the BK7 cover glass. These effects are included in the RCWA model.

Kogelnik's coupled-wave analysis give fairly good approximations of the spectral and angular bandwith $\Delta\lambda$ and $\Delta\theta$ respectively as

$$\Delta\lambda_{FWHM} = \frac{\lambda\Lambda}{d\cot(\theta_g)} \tag{3.4}$$

$$\Delta\theta_{FWHM} = \frac{\Lambda}{d}, \tag{3.5}$$

where d is the thickness of the active region of the volume hologram as specified in Figure 3.1.

The diffraction efficiency (DE) as determined by Kogelnik for the case of TE polarized E-field is

$$\eta_{TE} = \sin^2[\frac{\pi\Delta n_g d}{\lambda\cos(\theta_g)}], \tag{3.6}$$

whereas the diffraction efficiency for TM polarized light η_{TM} is given by,

$$\eta_{TM} = \sin^2[\frac{\pi\Delta n_g d\cos(2\theta_g)}{\lambda\cos(\theta_g)}], \tag{3.7}$$

where θ_g is the angle inside the grating material, and can be determined using Snell's law.

For the case of unpolarized light, the diffraction efficiency is approximated by the average between the DE for TE and TM polarizations and is expressed as

$$\eta_{Unpol} = \frac{1}{2}[\sin^2[\frac{\pi\Delta n_g d}{\lambda\cos(\theta_g)}] + \sin^2[\frac{\pi\Delta n_g d\cos(2\theta_g)}{\lambda\cos(\theta_g)}]]. \tag{3.8}$$

3.3 Optimization for the RGB Wavelengths with Unpolarized Light

The grating is optimized to determine the refractive index modulation needed to get diffraction efficiencies higher than 98% at 532nm, and at least 70% for all wavelengths between 400-700nm for unpolarized incident light. The reason for these percentage choice is simplify driven by the desire to have a minimum diffraction efficiency that is usable for all wavelengths in the visible spectrum. Due to the fact Kogelnik's method does not include the effect of absorption from the BK7 cover glasses, which is also a function of the BK7's dispersion, the RCWA method is used in order to incorporate all losses due to wavelength dependent absorption.

The optimal solution is determined using Monte Carlo analysis for wavelength values between 400 and 700 nm to maximize the diffraction efficiencies of Equations 3.6-3.8 using a random generator containing 50 million index modulation values between 0 and 0.05. Theoretically, the index modulation can be as high as possible, even higher than 0.1; however, in order to avoid milking of the DCG, the index modulation must not be very high.

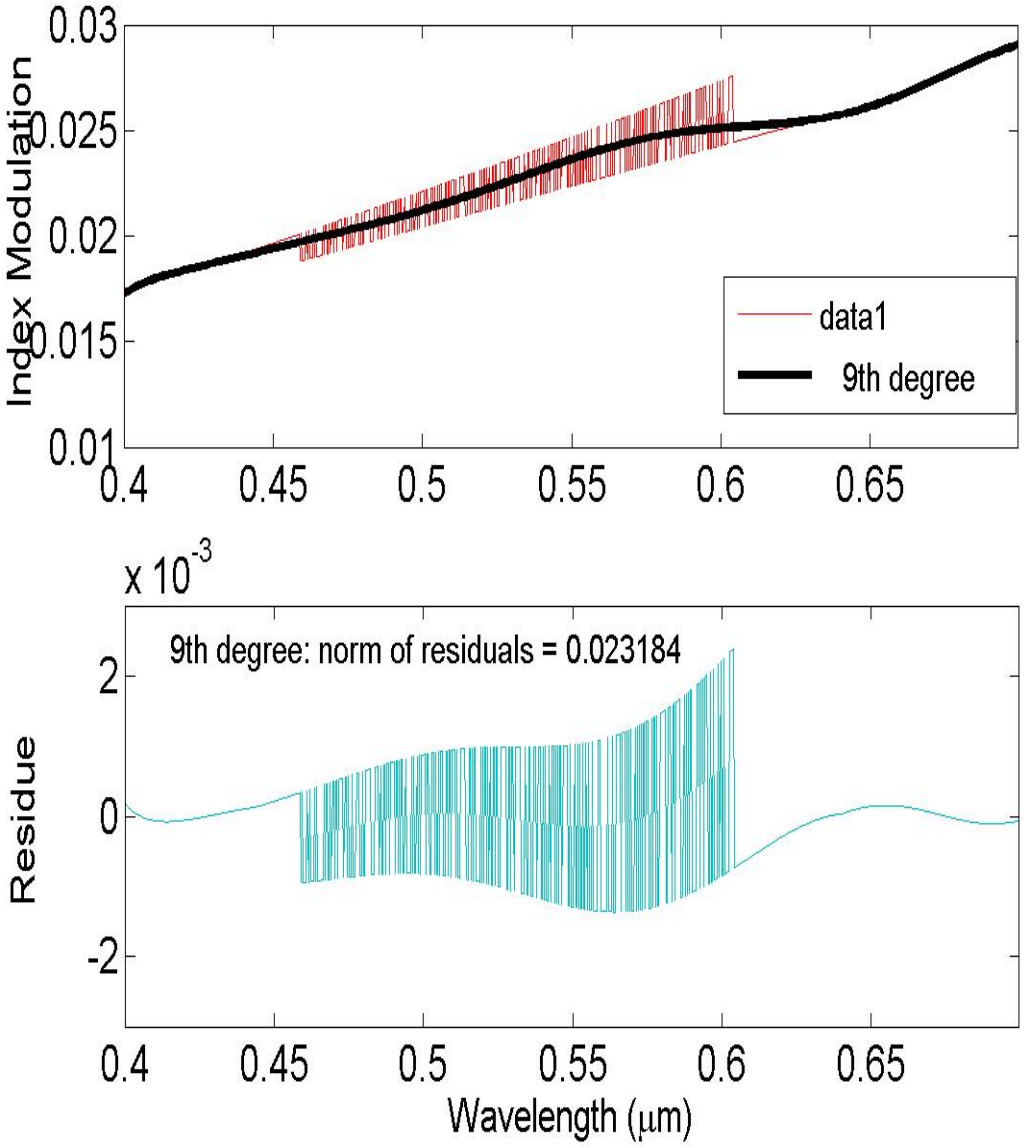

Figure 3.2: Index modulation versus wavelength as determined from the Monte Carlo analysis. The upper plot shows the result of the analysis and its 9^{th} order polynomial fit. The lower plot shows the residue, which is the difference between the simulated value of the modulations and the 9^{th} order polynomial fit.

Figure 3.2, shows the plot of the index modulation versus wavelength, its 9^{th} order polynomial fit, and the residue, calculated as the difference between the two. This result can be used as a rule of thumb to determine the approximate index modulation needed to design a volume phase hologram that gives diffraction efficiencies higher than 70% for all wavelengths of the visible spectrum. The refractive index modulation is determined by averaging all indices for diffraction efficiencies values between 75% and 98%. The result of the analysis yielded an average index modulation of $\Delta n = 0.022$, for highest theoretical diffraction efficiency of 98% at 532 nm. The average index modulation is calculated in the following steps:

a. Determine the refractive index modulations for each wavelength, red, green, and blue from the Monte Carlo Analysis.

b. Calculate the average and standard deviation of the index modulation.

c. Using the average and standard deviation one can tune the design to be red or blue shifted.

The index modulation can be calculated using,

$$\Delta n = \Delta n_{av} - \alpha \sigma_{\Delta n} \tag{3.9}$$

where α is a value between 0 and 1, Δn_{av} is the average value between the index modulation for red, green, and blue wavelengths, and $\sigma_{\Delta n}$ is their standard deviation.

Furthermore, this optimization is still preliminary until the design is re-run using an RCWA model. The result obtained from the RCWA yielded a maximum

theoretical diffraction efficiency of 94% shown in Figure 3.4.

3.4 Order Requirement for RCWA

The accuracy of the rigorous coupled-wave analysis to yield the right value is dependent on the number of propagating orders considered and the Fourier terms used to approximate the profile in the active region of grating. Previous work (Moharam et al., 1995b,a) have studied the numerical stability for a surface relief grating; however they have not addressed these criteria for the case volume holograms. In this section of the dissertation, an investigation of the order requirement needed for a stable solution is addressed.

Based on the results shown on Figure 3.3 it can be seen that the order requirement for the RCWA to yield a stable result is fairly simple. The results of the calculations yield a stable result as long as one considers at least three propagating orders. An investigation into the change of the magnitude of the diffraction efficiencies between two and three propagating orders showed percent differences of 0.4258%, 0.4479%, and 0.0393% for the cases of blue, green, and red Bragg wavelengths. These differences show that if it is not for the absorption of the BK7, Kogelnik's two wave coupled wave analysis already suffice to yield an acceptable result. However in order to have enough Fourier terms to construct a fairly good profile of the period structure within the active region of the grating material, we have used twenty-five propagating orders in the entire RCWA calculations within this dissertation.

Furthermore, one can conclude from the results of Figure 3.3 that the only factor that will induce variation in the spectral and angular response of the first order of

forward diffraction for this volume hologram is the wavelength dependent absorption from the BK7 cover glasses.

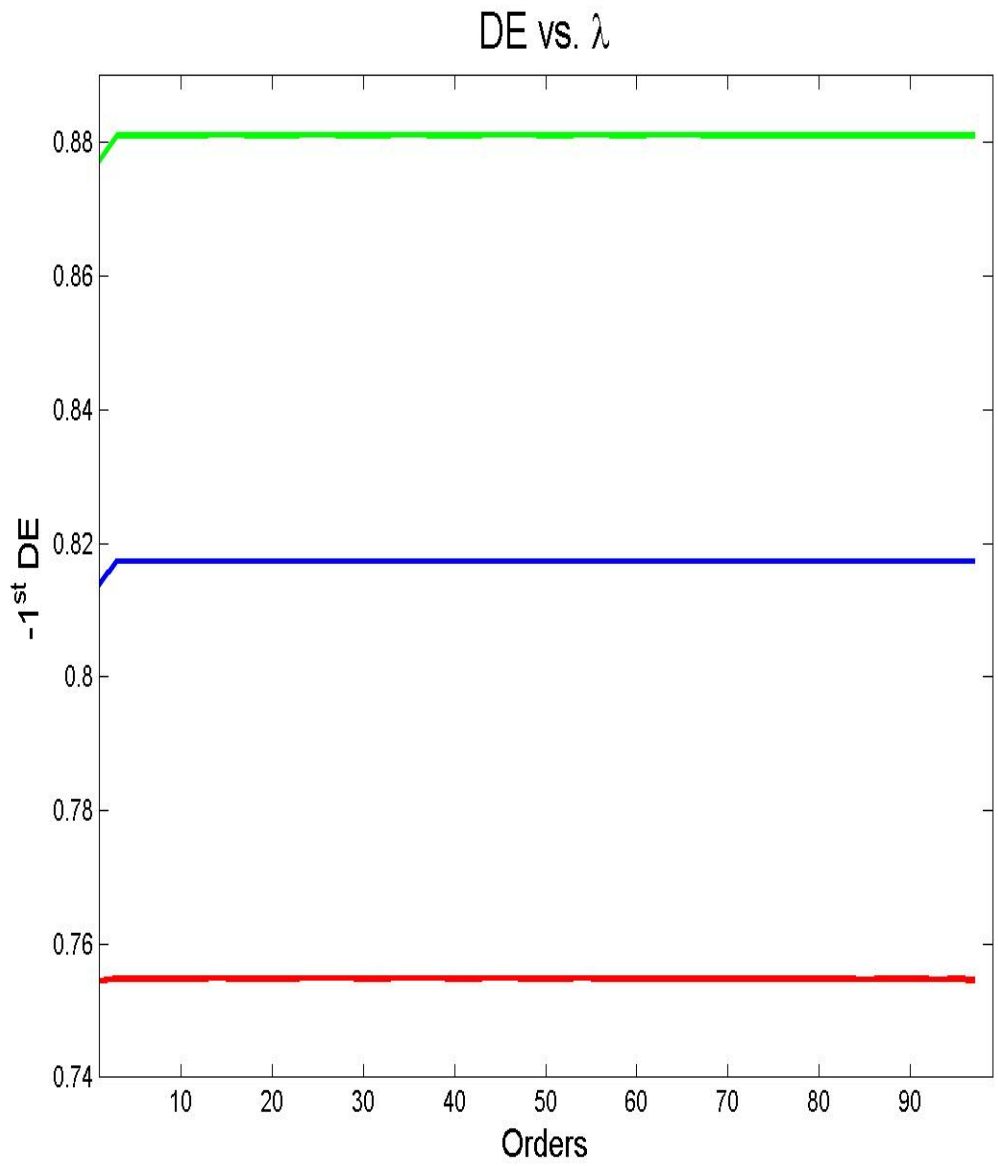

Figure 3.3: Diffraction efficiency versus number of propagating orders. The green, blue, and red lines represent the response of the hologram at Bragg wavelengths of 532nm, 460nm, and 632nm respectively.

3.5 Simulation of the RGB Volume Hologram

The RGB Volume Phase Hologram is a special grating designed for providing high diffraction efficiency for the wavelength regions between 400 to 700 nm. Due to the high demand for the use of volume holograms, the design of a volume hologram with superblaze envelope having high efficiency values over the entire visible spectrum is introduced. The superblaze is the envelope obtained from an ensemble of diffraction efficiency versus wavelength plots for different incidence angle; however maximum efficiencies are obtained at the Bragg angles. The design of this hologram can help scientists and engineers to utilize a single volume hologram for multiple tasks. This volume hologram provides more than 75% efficiency for the red, blue, and green light.

Figure 3.4 shows the plots of the efficiency versus wavelength for all three Bragg angles determine using wavelength values of $460nm$, $532nm$, and $632nm$. Efficiency plots determined ignoring wavelength dependent absorption from the cover glasses are shown in black, and the ones considering the effect of absorption are shown in colors representing their peak wavelength values. A comparison between the plots of the diffraction efficiencies in the presence of absorption to those without absorption, shows that absorption of the BK7 cover glasses reduce the efficiencies at the Bragg wavelengths for all three wavelengths; however effect of absorption is mainly seem in the red region of the visible spectrum. The inclusion of the absorption from the BK7 reduced the spectral bandwidth as well.

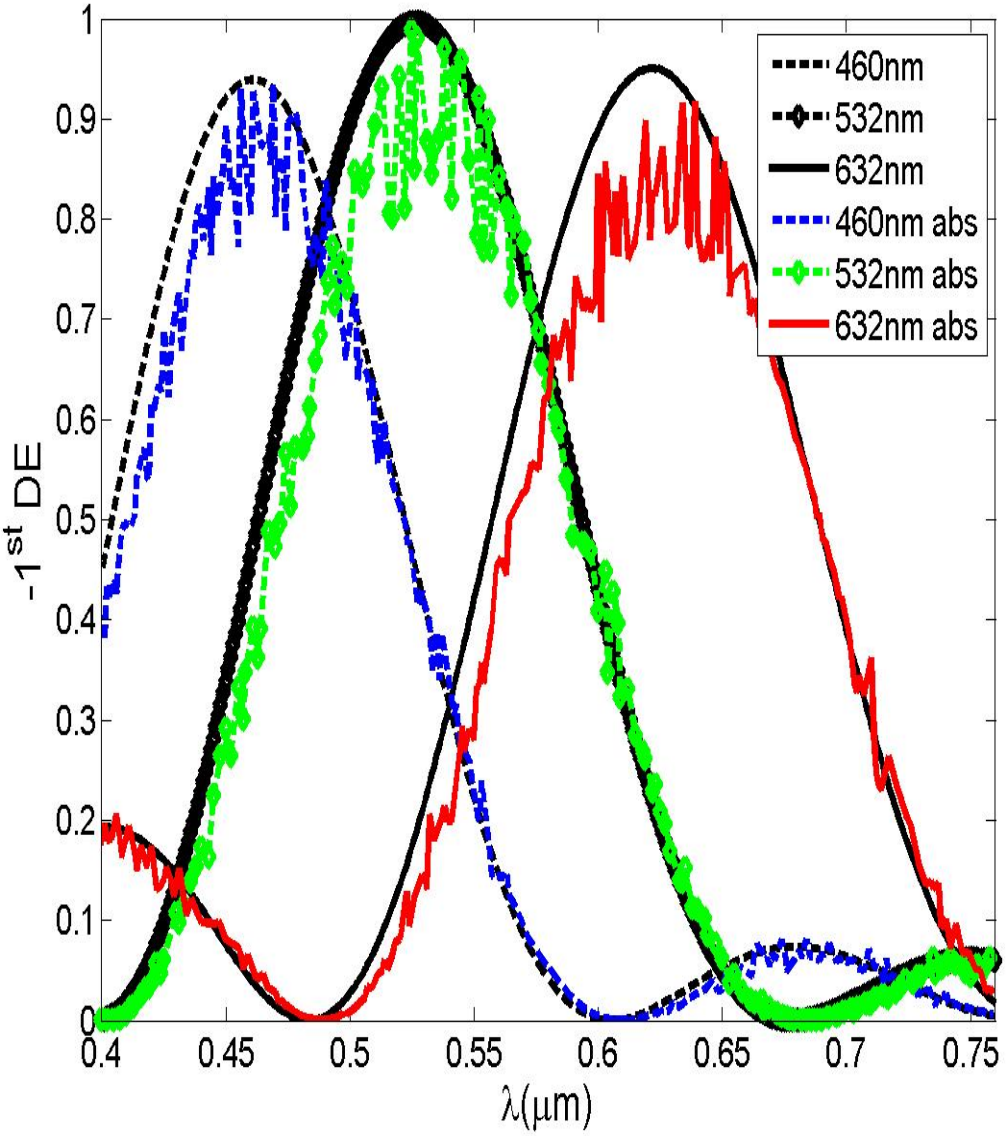

Figure 3.4: Diffraction efficiencies versus wavelength. The black dashed, black diamond, and black solid lines are the efficiency plots simulated at Bragg angles determined with for blue, green, and red wavelength when absorption due to BK7 cover glasses were not included. The blue dashed line, green line with diamond, and the red solid lines are the efficiencies for the cases that include effects of absoption.

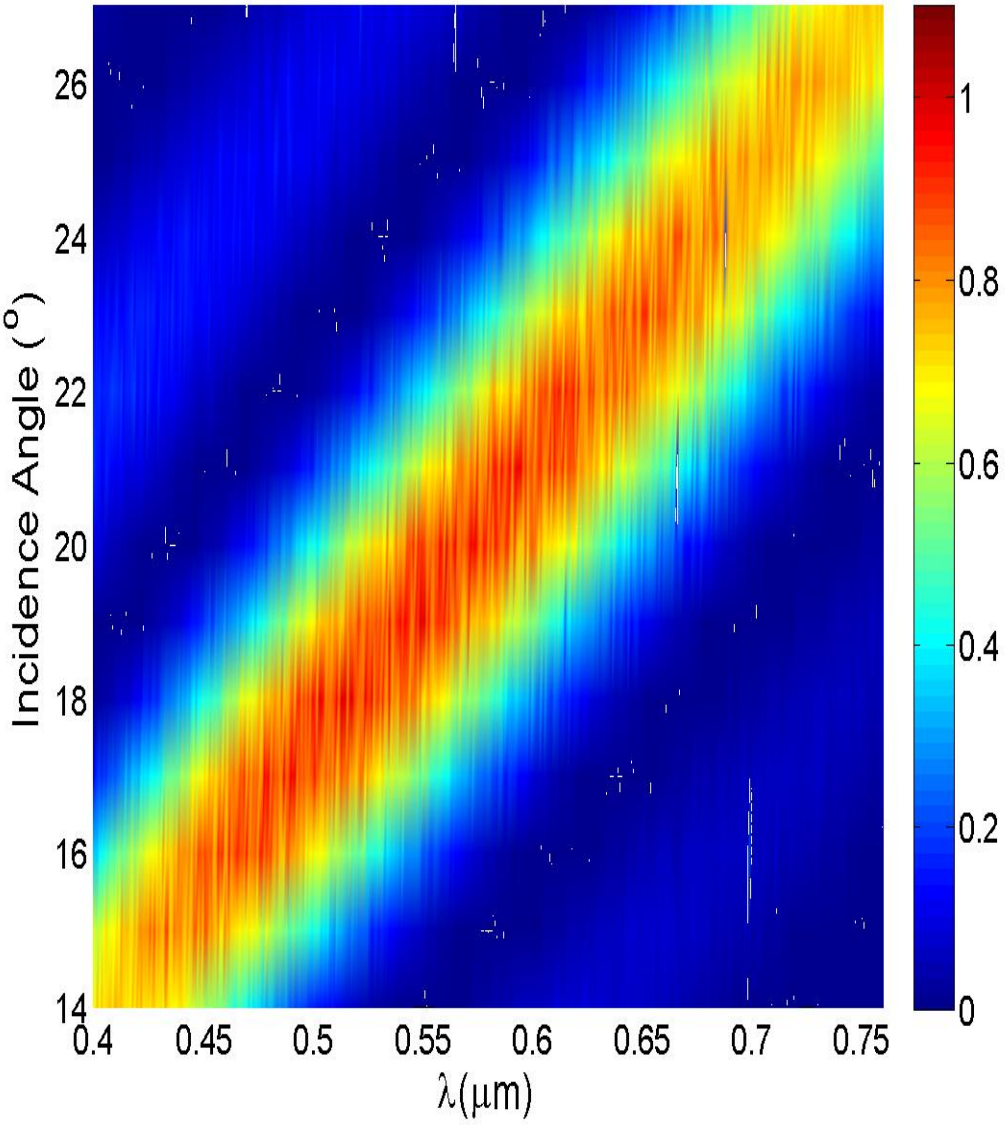

Figure 3.5: 2-D plot of the diffraction efficiencies as functions of wavelength and incidence angle. Data is acquired for the entire visible spectrum for incidence angles between 14^o and 27^o with an increment of 1^o.

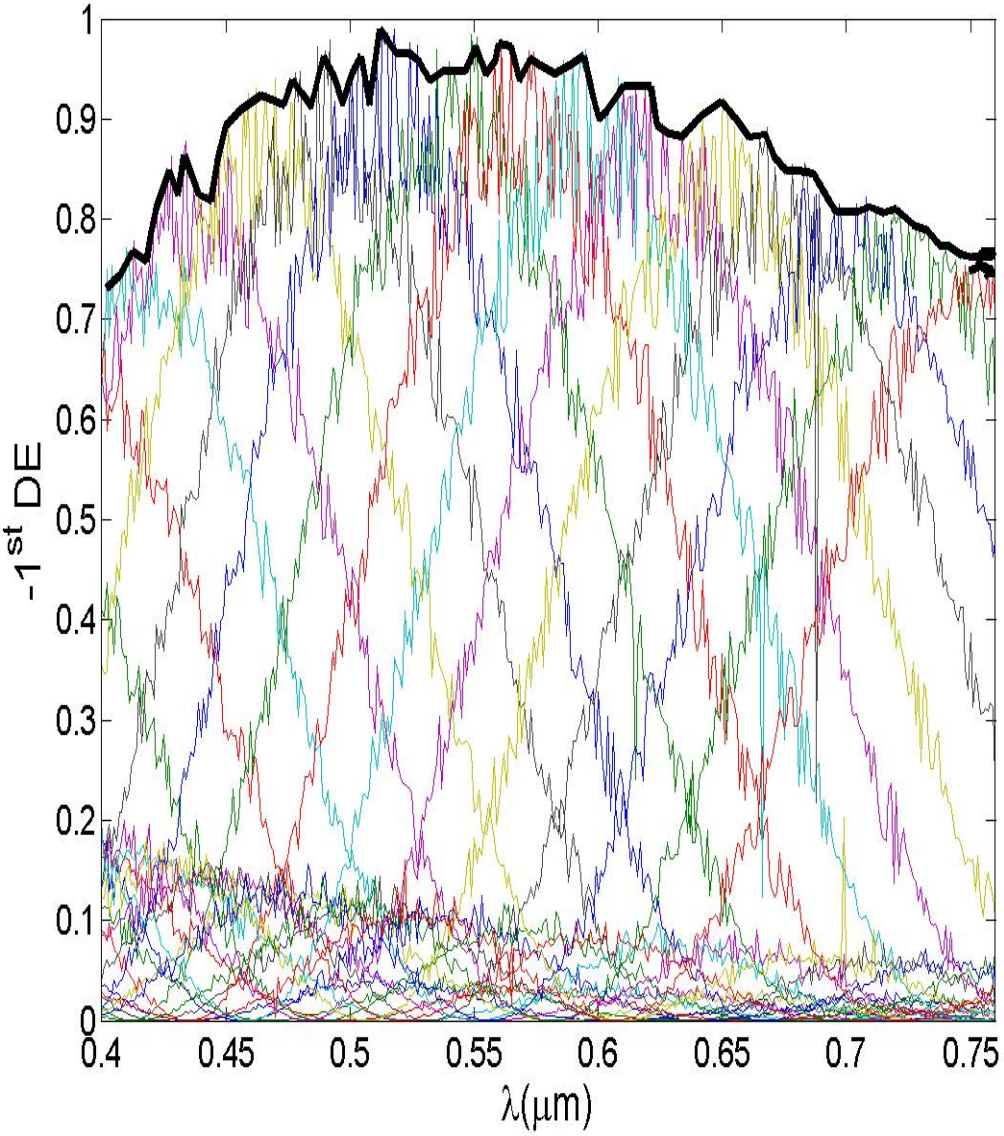

Figure 3.6: Blazed curves for the different incidence angles, and the superblaze envelop that covers the entire visible spectrum.

Figure 3.5 shows a full map of the simulated diffraction efficiencies for the visible spectrum versus incidence angles, from 14^o to 27^o. The results shown in this figure indicate that the volume hologram will exhibit at least 70% efficiency for all wavelengths of the visible spectrum with their corresponding angles as shown in Figure 3.5.

Figure 3.6 depicts the blazed curves for multiple incidence angles. The blazed curves are the diffraction efficiency plots at different incident grating angles and have their maximums at their respective wavelengths according to the Bragg condition. The envelope resulting from the blazed curves is the super blaze curve. The super-blaze curve is the envelope shown in Figure 3.6 by the solid black line. This envelope explains the fact that this volume hologram is designed for operation in the red, green, and blue wavelengths and can also give acceptable diffraction efficiencies for the entire visible spectrum.

Since the design is optimized to provide highest efficiency at 532 nm, it can be seen on Figures 3.4-3.6 that maximum efficiency is obtained around the green region of the spectrum.

3.6 Fabrication Tolerances

Due to many beneficial factors, the dichromated gelatin was the preferred material for the fabrication of the RGB volume phase hologram. However, during the recording process many factors can introduce defect and non-uniformity to the volume hologram's optical performance. For that reason, it is wise to develop a few fabrication tolerances to help reduce the intrinsic and extrinsic sources of errors that would affect the performance of the final product. Some of the main factors that needed to be

controlled with fabrication tolerances are:

a. The grating thickness, which can increase during the swelling phase of the DCG.

b. The index modulation which can be affected by the recording onto the DCG and processing of the final product.

c. The incidence angles of the two coherent beams used for creating the interference pattern within the active region of the hologram will need to be aligned properly, in order to avoid errors and introduction of slant angle.

In theory the thickness of the volume hologram is fixed at $12\mu m$, but in reality the thickness could change either because of fabrication errors or temperature change. Figure 3.7 shows the change of the diffraction efficiency as function of thickness variation.

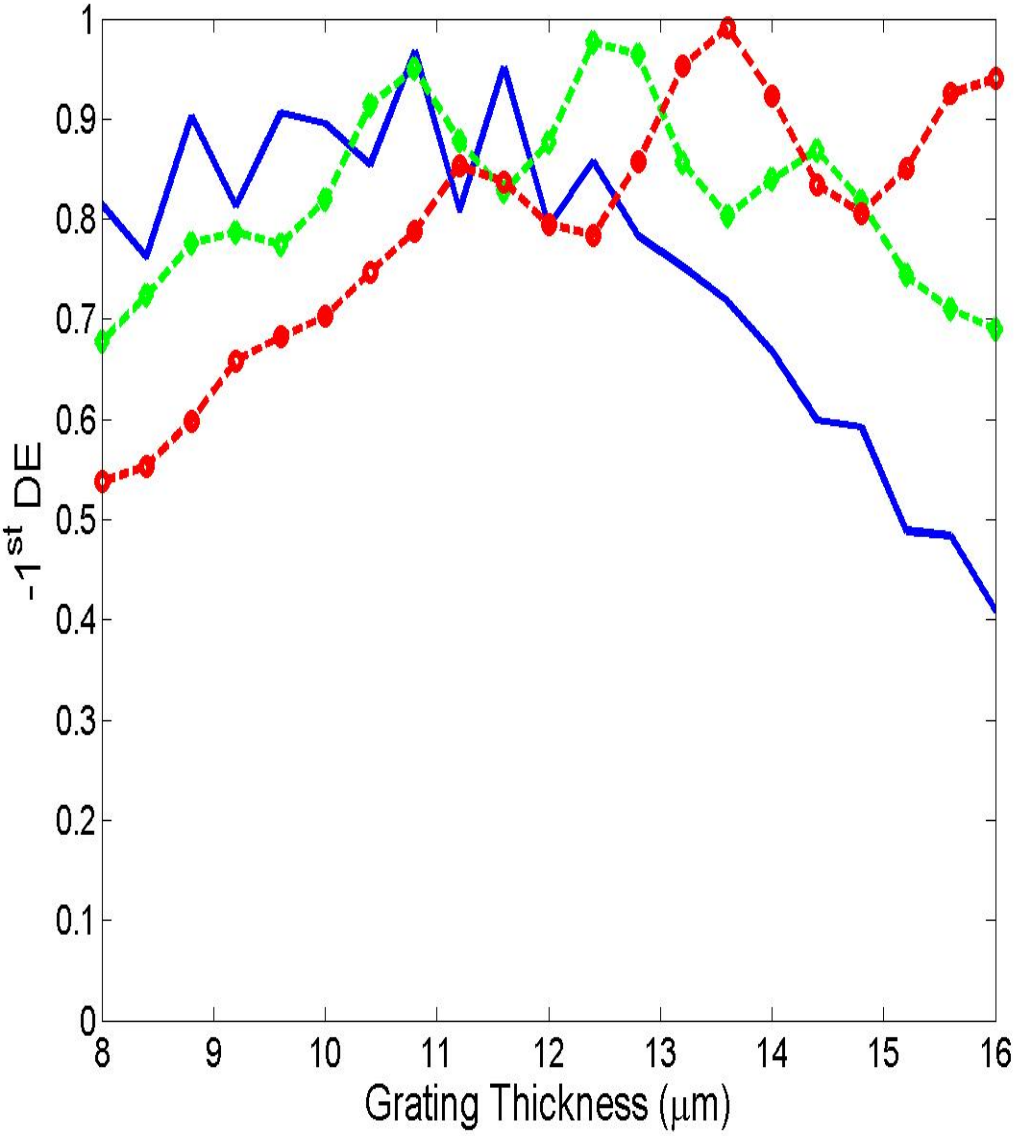

Figure 3.7: Diffraction efficiency versus thickness of the active region of the RGB volume phase holographic grating.

It is noticeable that as the thickness of the active region deviates away from the design thickness, the diffraction efficiency changes as well. However, since this grating is designed and optimized to have higher efficiency at $\lambda = 532nm$, diffraction efficiency change with grating thickness is more stable compared to the changes seen at design wavelengths of $\lambda = 460nm$ and $\lambda = 632nm$. Figures 3.8, 3.9, 3.10 depict the effect of DCG thickness change on the overall diffraction efficiency and the spectral bandwidth for blue, green, and red wavelengths respectively. For all three cases, the spectral bandwidth is increased as the thickness of the active region is decreased by 10%, and decreased as the thickness is increased by the 10%. Moreover, the change in the thickness of the active region changed the magnitude of the diffraction efficiency for the blue and red wavelengths. However, the diffraction efficiency at the optimization wavelength, the green $\lambda = 532\mu m$, did not change by a significant amount.

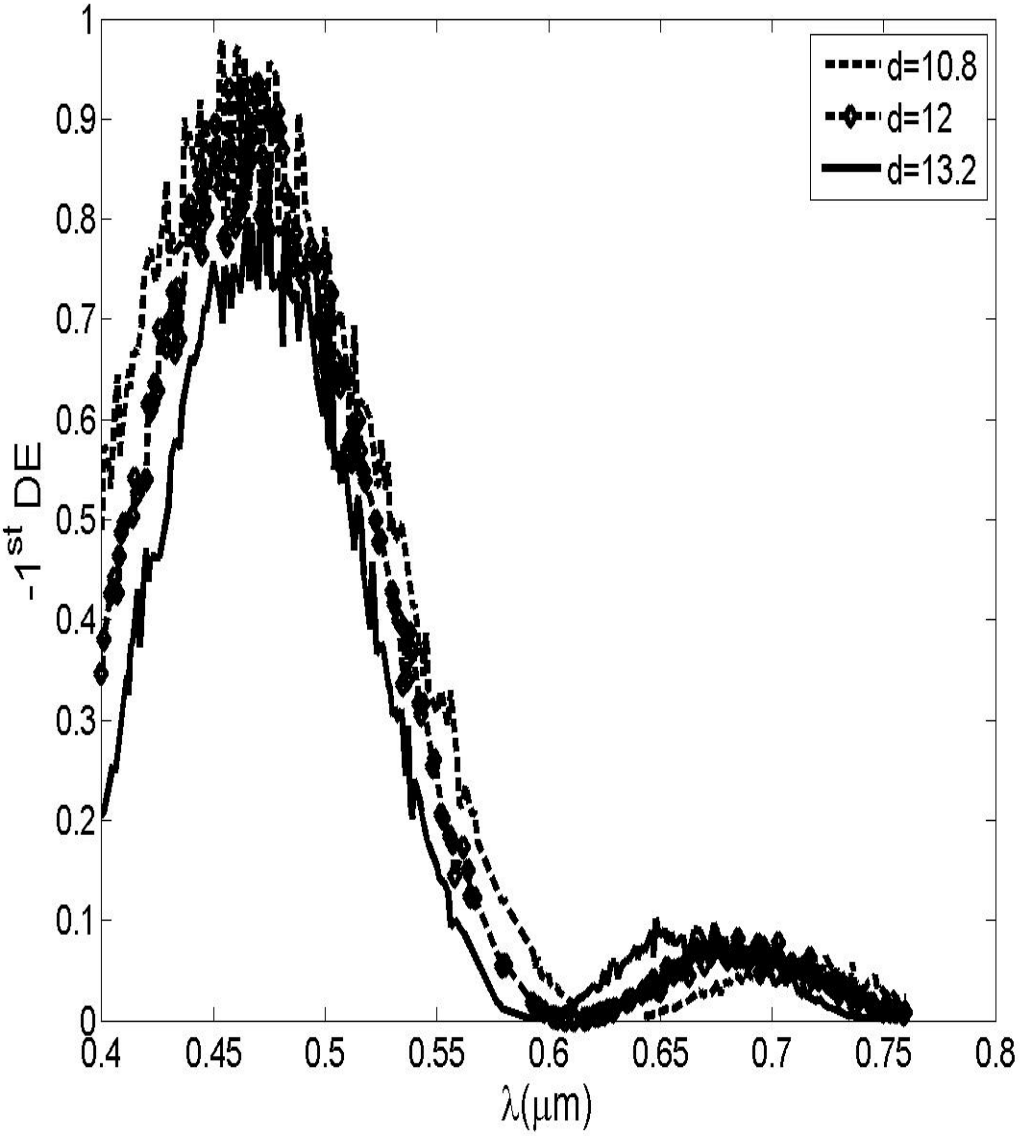

Figure 3.8: Diffraction efficiency versus wavelength plots for design wavelengths of 460 nm. The dashed lines are the plots for the case when d is reduced by 10%, the line with diamond points is when d is equal to the design thickness of $12\mu m$, and the solid line with circles for when d is increased by 10%.

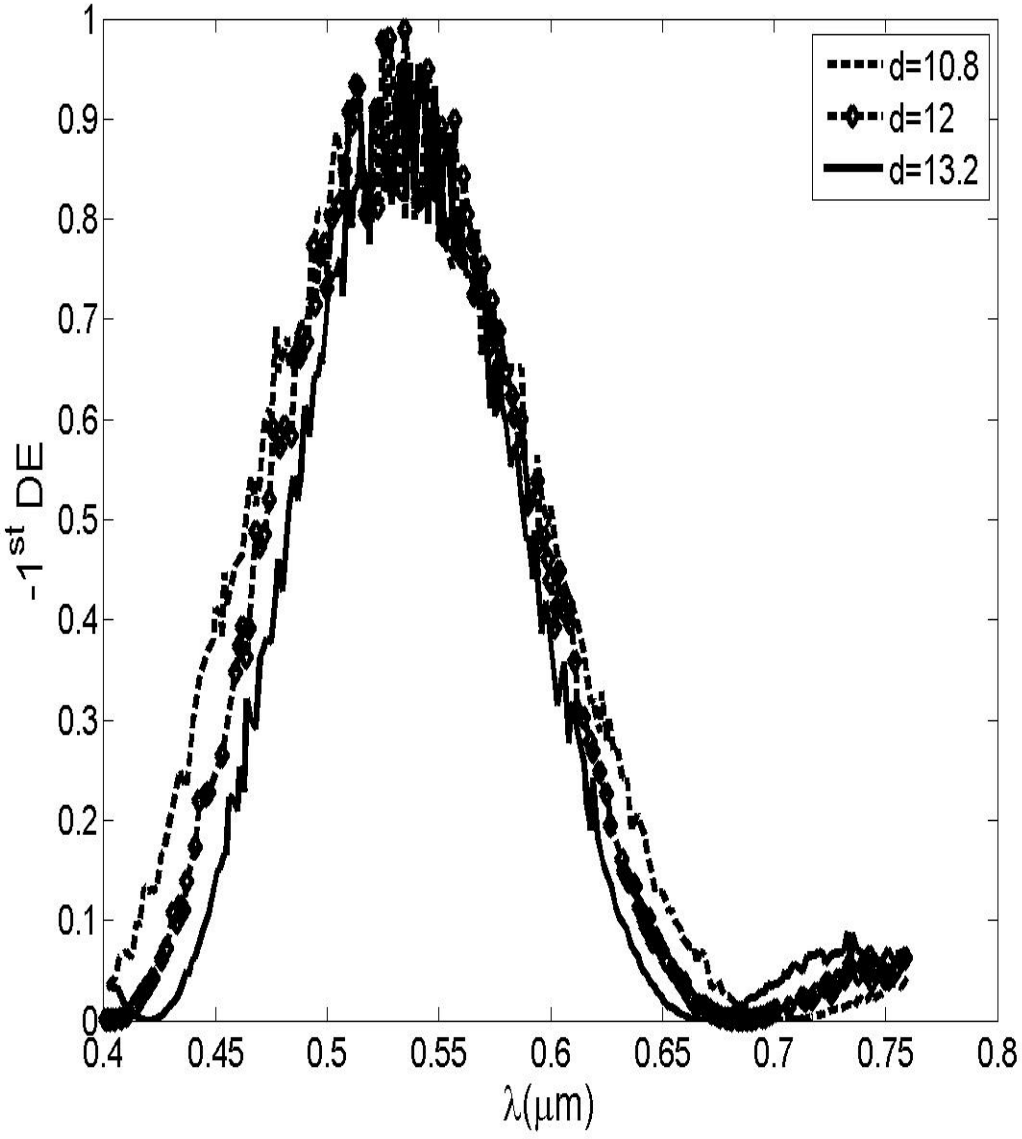

Figure 3.9: Diffraction efficiency versus wavelength plots for design wavelengths of 532 nm. The dashed lines are the plots for the case when d is reduced by 10%, the line with diamond points is when d is equal to the design thickness of $12\mu m$, and the solid line with circles for when d is increased by 10%.

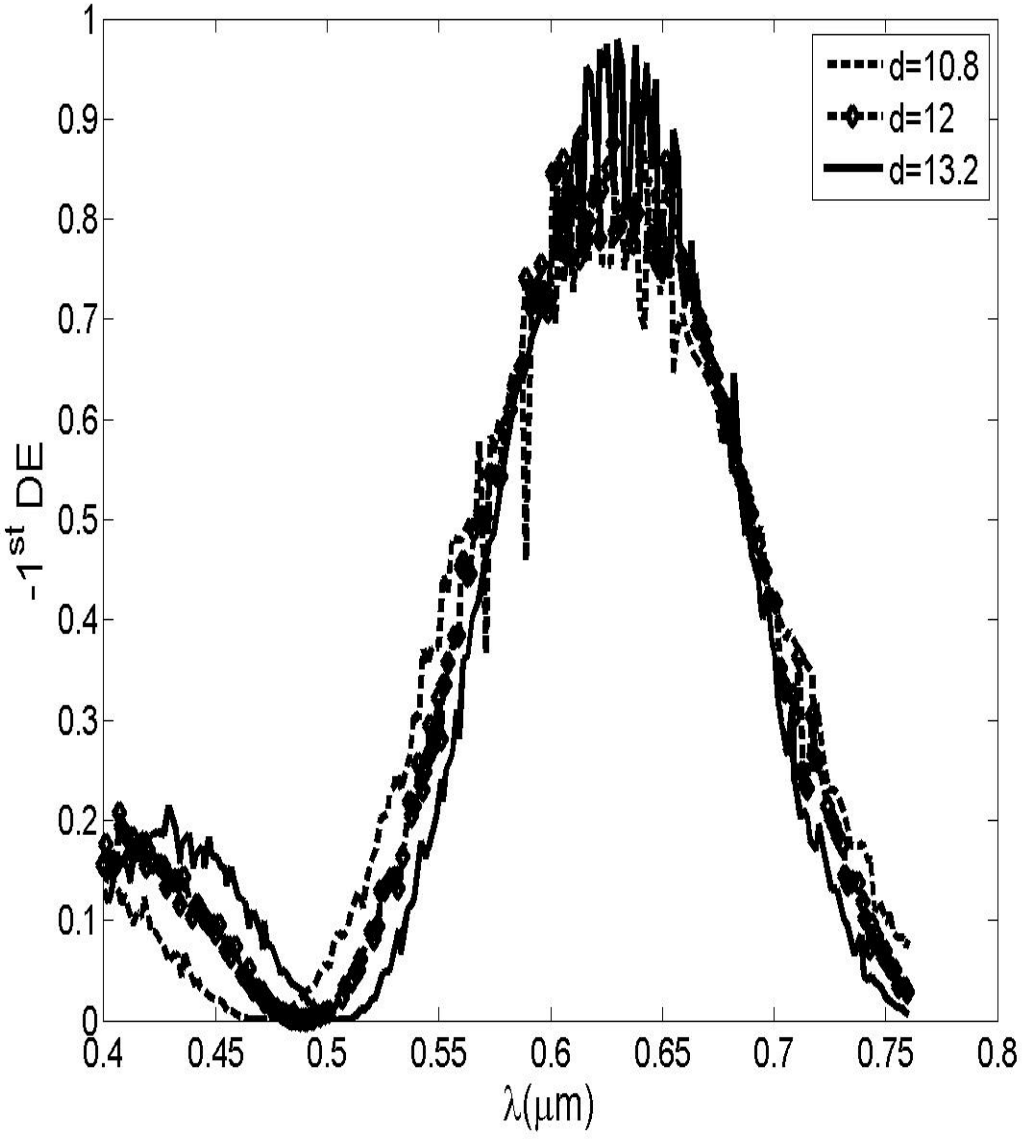

Figure 3.10: Diffraction efficiency versus wavelength plots for design wavelengths of 632 nm. The dashed lines are the plots for the case when d is reduced by 10%, the line with diamond points is when d is equal to the design thickness of $12\mu m$, and the solid line with circles for when d is increased by 10%.

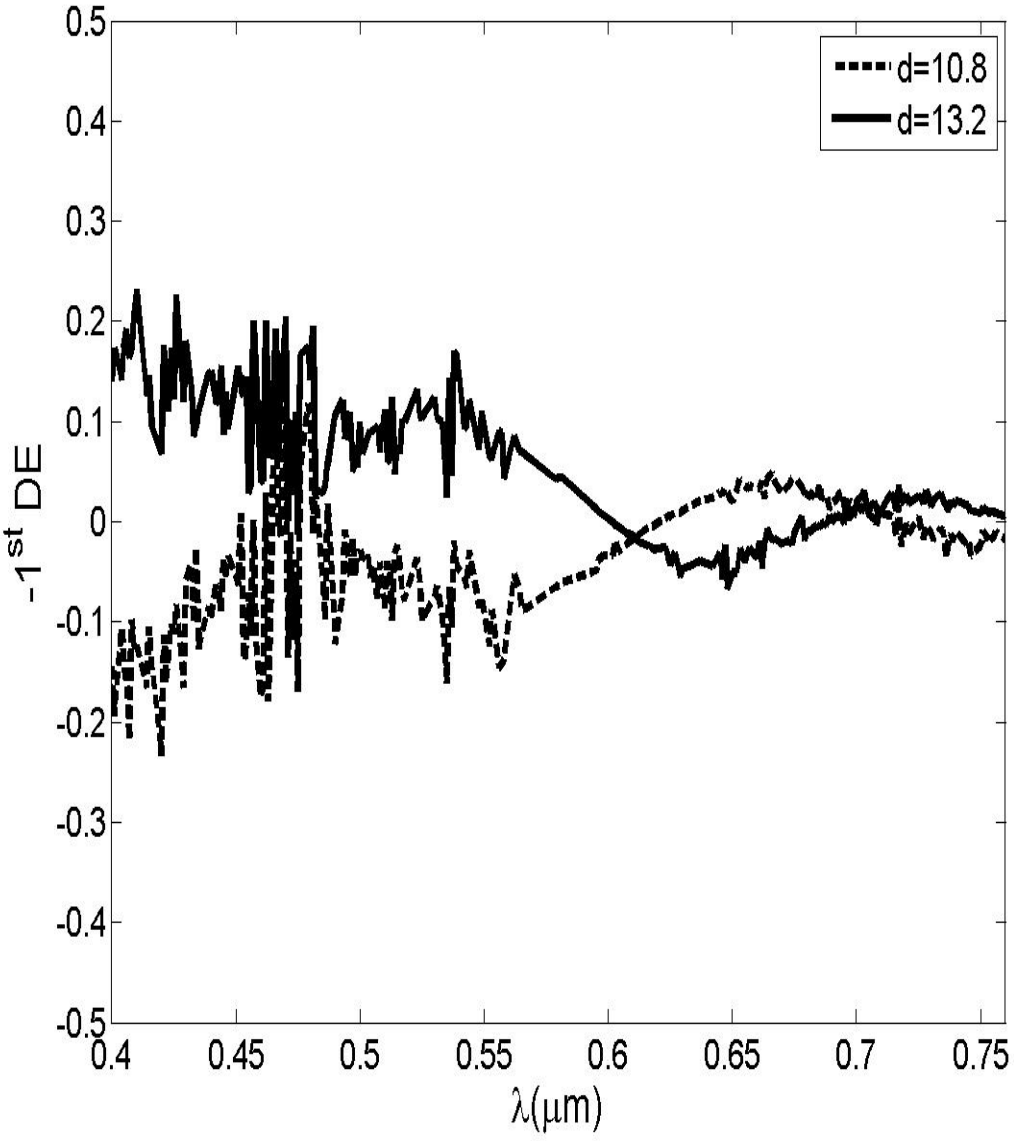

Figure 3.11: Diffraction efficiency change between the case of the nominal thickness and a change by 10% for blue light. The dashed line are the plots for when d is reduced by 10%, the solid line is when d is increased by 10%.

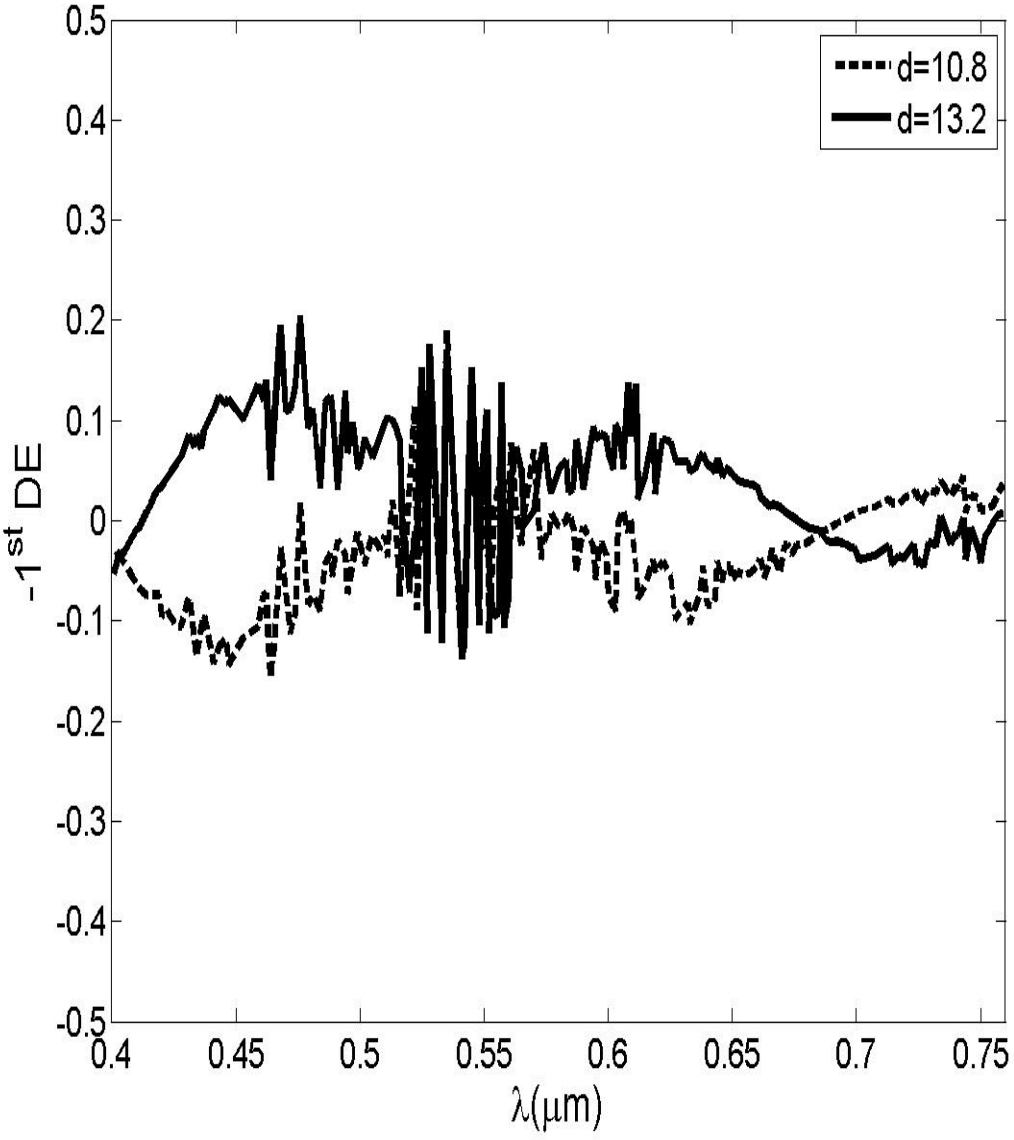

Figure 3.12: Diffraction efficiency change between the case of the nominal thickness and a change by 10% for green light. The dashed line are the plots for when d is reduced by 10%, the solid line is when d is increased by 10%.

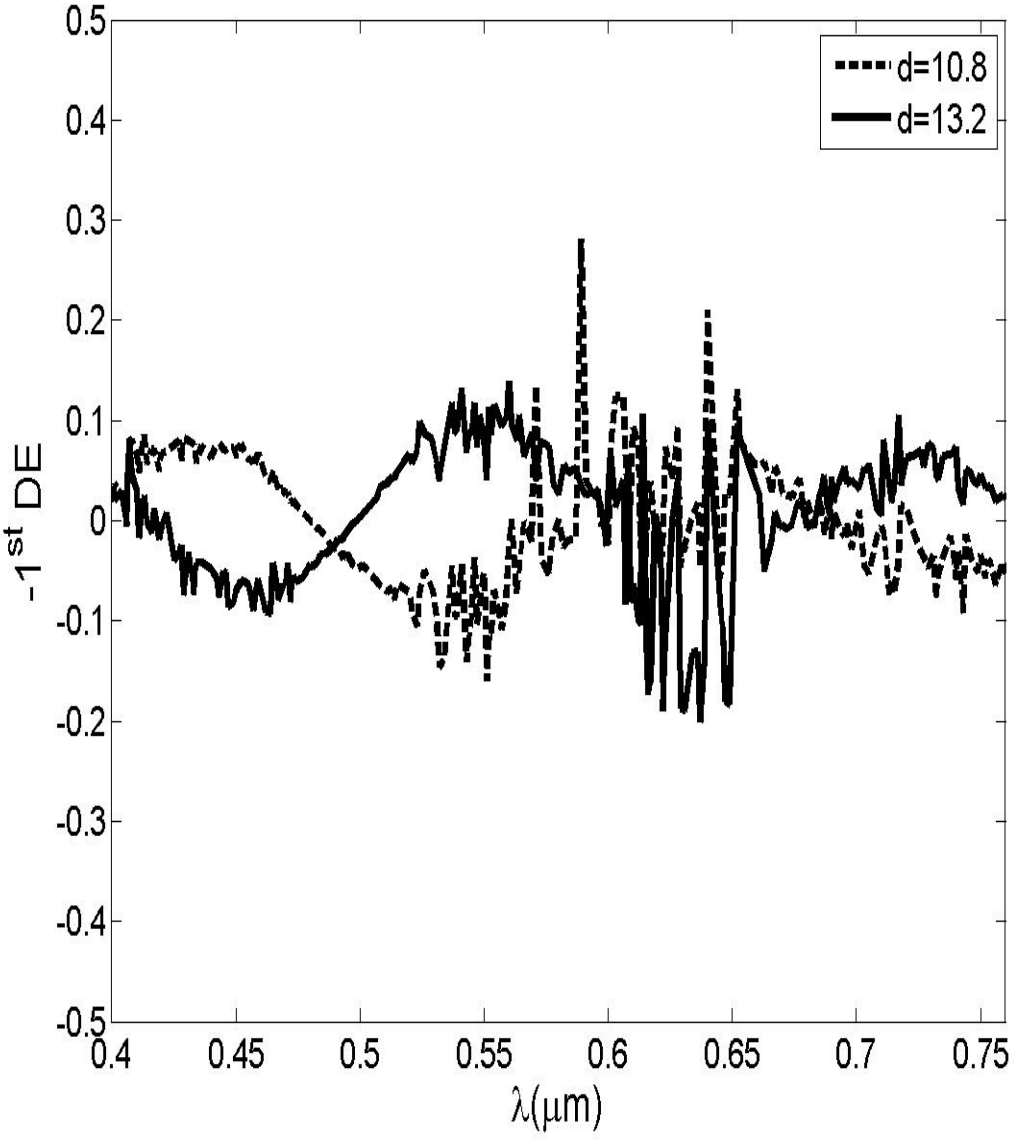

Figure 3.13: Diffraction efficiency change between the case of the nominal thickness and a change by 10% for red light. The dashed line are the plots for when d is reduced by 10%, the solid line is when d is increased by 10%.

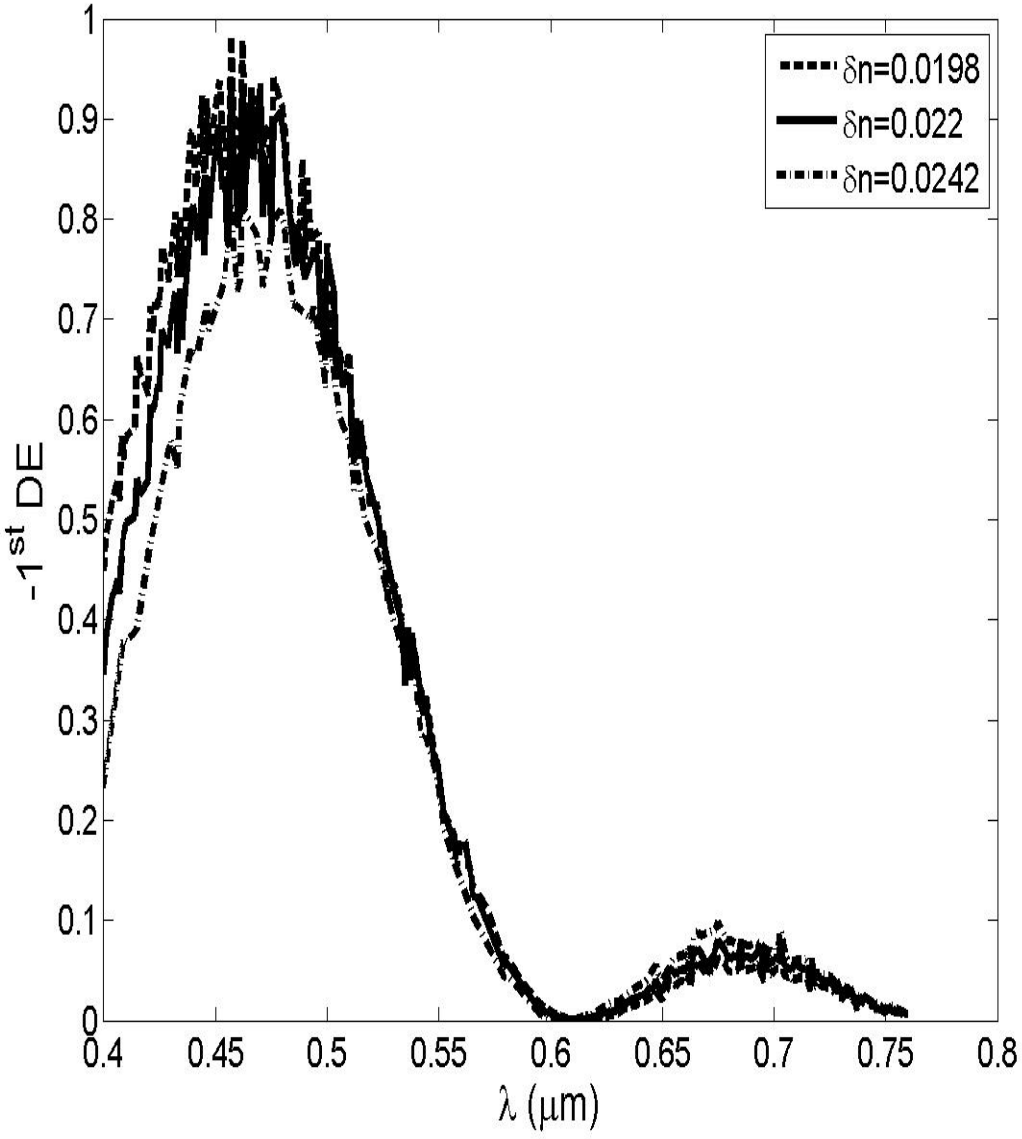

Figure 3.14: Diffraction efficiency versus wavelength plots for design wavelength of 460 nm. The dashed lines are the plots for the case when δn is reduced by 10%, the line with diamond points is when d is equal to the design index modulation of 0.022, and the solid line with circles for when δn is increased by 10%.

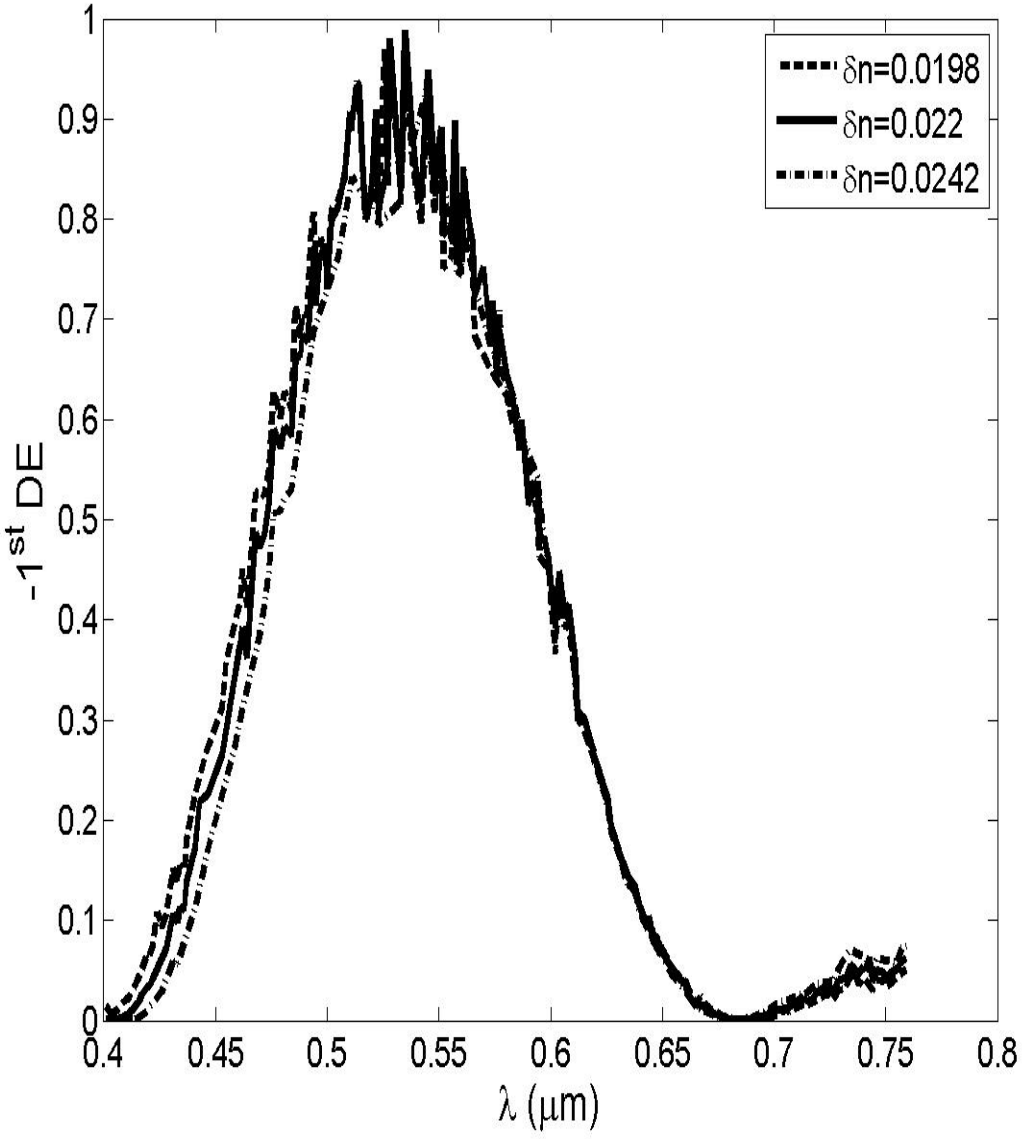

Figure 3.15: Diffraction efficiency versus wavelength plots for design wavelength of 532 nm. The dashed lines are the plots for the case when δn is reduced by 10%, the line with diamond points is when d is equal to the design index modulation of 0.022, and the solid line with circles for when δn is increased by 10%.

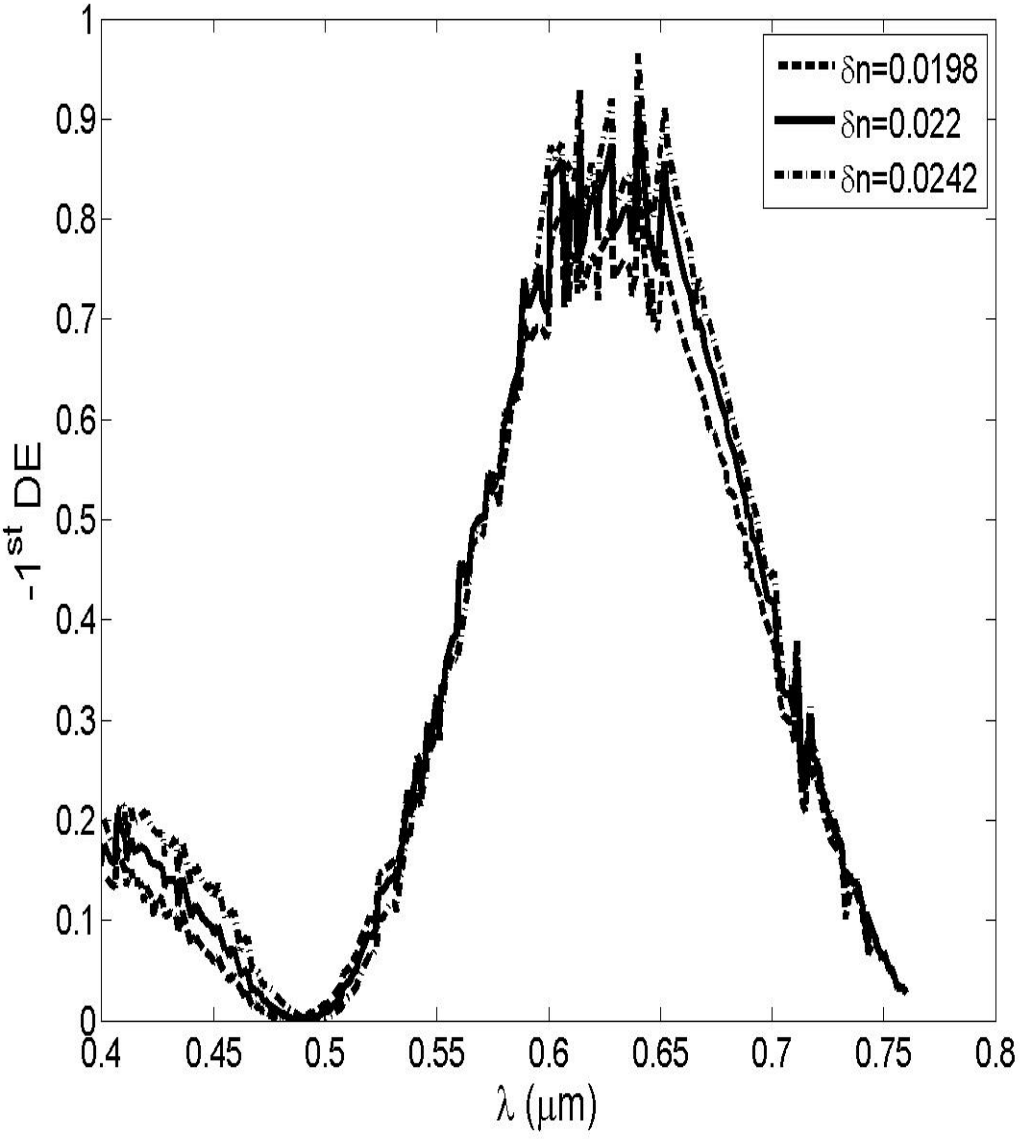

Figure 3.16: Diffraction efficiency versus wavelength plots for design wavelength of 632 nm. The dashed lines are the plots for the case when δn is reduced by 10%, the line with diamond points is when d is equal to the design index modulation of 0.022, and the solid line with circles for when δn is increased by 10%.

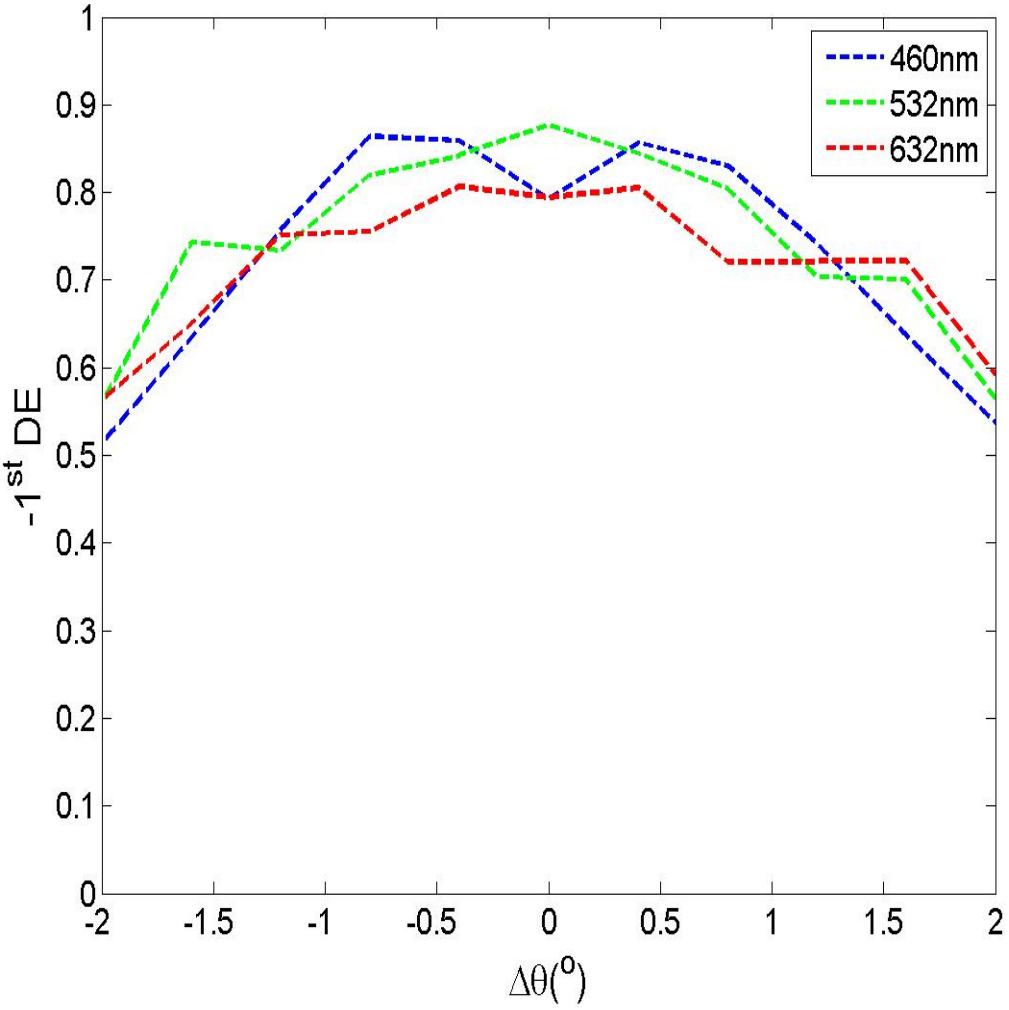

Figure 3.17: Diffraction efficiency versus change in the incident angles. The dashed line, the solid line, and the dashed line with dots show the efficiency plot for design wavelengths of 460 nm, 532 nm, and 632 nm respectively.

Figures 3.11, 3.12, and 3.13 show that a change in the thickness of the grating greatly affects the diffraction efficiencies for the design wavelengths of 460nm, and 632nm; however, this change is reduced significantly for 532nm. This reduction in the magnitude of the diffraction efficiency for 532 nm is a consequence of the optimization. The same effect can be seen if the plots shown in Figures 3.14, 3.15, and 3.16, where diffraction efficiency is plotted versus wavelength for all three design wavelengths as index modulation is changed by 10% from the optimal value of 0.022.

Figure 3.17 depicts the diffraction efficiency as a function incidence angle change away from the determined Bragg's angles for design wavelengths of 460 nm, 532 nm, and 632 nm respectively. The results shown in this figure show that the RGB volume hologram will yield diffraction efficiency of 70% even in the presence of 1^o alignment error. Furthermore, the plots show that the maximum efficiency is seen at exactly at Bragg's angle for 532 nm. This plot also illustrates the fact this volume hologram is optimized at $\lambda = 532nm$.

3.7 Conclusion

Overall, we showed that a volume phase hologram for simultaneous use with red, green, and blue wavelengths can be fabricated. We also showed in Figures 3.4 and 3.5 that as long as Bragg's condition is respected, the same volume phase hologram can be used for all wavelengths in the visible part of the spectrum. This volume hologram gives a theoretical diffraction efficiency of at least 70% for all wavelengths in the visible and highest efficiencies are obtained in the green region of the spectrum. Moreover, since human errors and other factors during fabrication can introduce various errors to the performance of the final product, we also determined a few tolerances that may

help in increasing the accuracy of the fabrication process. It was determined that the thickness of the thin film must be controlled with a tolerance of $\pm 1 \mu m$ and the angles during recording of the holographic optical elements must be kept in within a tolerance of $\pm 0.5^{\circ}$. As a final point, we believe that the design of a multi-task volume hologram can be beneficial by reducing the number of optical elements in a multi-wavelength system.

Chapter 4

Writing, Measurement, and Validation

4.1 Introduction

The last few chapters focused on the theoretical design and simulation of the diffraction efficiencies of the transmission volume holographic grating; however in order to have a complete design and system level characterization of the grating, experimental data are required to validate the accuracy and completeness of the design. For these reasons, one needs to develop a physical prototype of the transmission volume hologram. In this section of the dissertation, experimental set up for writing the hologram on a dichromated gelatin (DCG) is discussed. This chapter will also talk about the experimental set up and measurement of the diffraction efficiencies of light as it propagates and diffracts through the grating.

4.2 Writing of the Holographic Grating

Volume holograms are types of diffractive optical elements that diffract light via a refractive index modulation within the active region of the grating element. This index modulation is created by interfering two coherent beams within a dichromted gelatin thin film. Interference is the consequence of the superposition of two or more electromagnetic waves. It is the mechanism by which light interacts with light, and it is also the key factor on the establishment of the wave nature of light. For the purpose of this dissertation, the interference effect is restricted to two waves, denoted

by $\vec{\boldsymbol{E}}_1$ and $\vec{\boldsymbol{E}}_2$ respectively. The results of their interference effect simplifies to,

$$I(x,y,z,t) = \langle|\vec{\boldsymbol{E}}_1|^2\rangle + \langle|\vec{\boldsymbol{E}}_2|^2\rangle + \langle\vec{\boldsymbol{E}}_1 \cdot \vec{\boldsymbol{E}}^*{}_2\rangle + \langle\vec{\boldsymbol{E}}^*{}_1 \cdot \vec{\boldsymbol{E}}_2\rangle, \tag{4.1}$$

where in general $\vec{\boldsymbol{E}}_1 = \vec{\boldsymbol{E}}_1(\boldsymbol{x}, \boldsymbol{y}, \boldsymbol{z})$ and similarly for $\vec{\boldsymbol{E}}_2$. The first and second terms on the right hand side of Equation 4.1 represent the individual intensities for the first and second beams, respectively. These two terms do not contribute to the generation of the refractive index modulation within the active region of the hologram. The information about the interference of the two waves are contained in the third and fourth terms. Moreover, if the two waves are assumed to be monochromatic and linearly polarized they can be expressed as,

$$\vec{\boldsymbol{E}}_i(x,y,z,t) = \vec{\boldsymbol{A}}_i(x,y,z,t)e^{j[\omega_i t - \phi_i(x,y,z,t)]}, \tag{4.2}$$

where i is an integer taking values of $1, 2$ specifying the first or second waves, A_i and ϕ_i are the complex amplitude and phase of the i^{th} wave. Substituting the expression in Equation 4.2 into Equation 4.1 and re-arranging the terms gives a new equation that shows the interference term in the form of a cosine,

$$I(x,y,z,t) = \langle|\vec{\boldsymbol{E}}_1|^2\rangle + \langle|\vec{\boldsymbol{E}}_2|^2\rangle + 2\left(\vec{\boldsymbol{A}}_1 \cdot \vec{\boldsymbol{A}}^*{}_2\right)\cos\left[(\omega_1 - \omega_2)\,t - (\phi_1 - \phi_2)\right]. \tag{4.3}$$

From the term with the cosine, one can tell that if the polarization of the two waves are orthogonal, the dot product $\vec{\boldsymbol{A}}_1 \cdot \vec{\boldsymbol{A}}^*{}_2$ will be zero, which will result in no interference and there won't a refractive index modulation within the active region of the volume hologram. Another observation is that, if the two waves have different

frequencies then there will be modulation in the interference pattern. Thus one must make sure that the two interfering beams must have the same frequency and polarized in the same direction. This is why the division of amplitude done by element NPBS, shown in Figure 4.1 must be done using a 50/50 non polarizing beam splitter; the 50/50 is also used in order to maximize the contrast in term of visibility of the interference pattern.

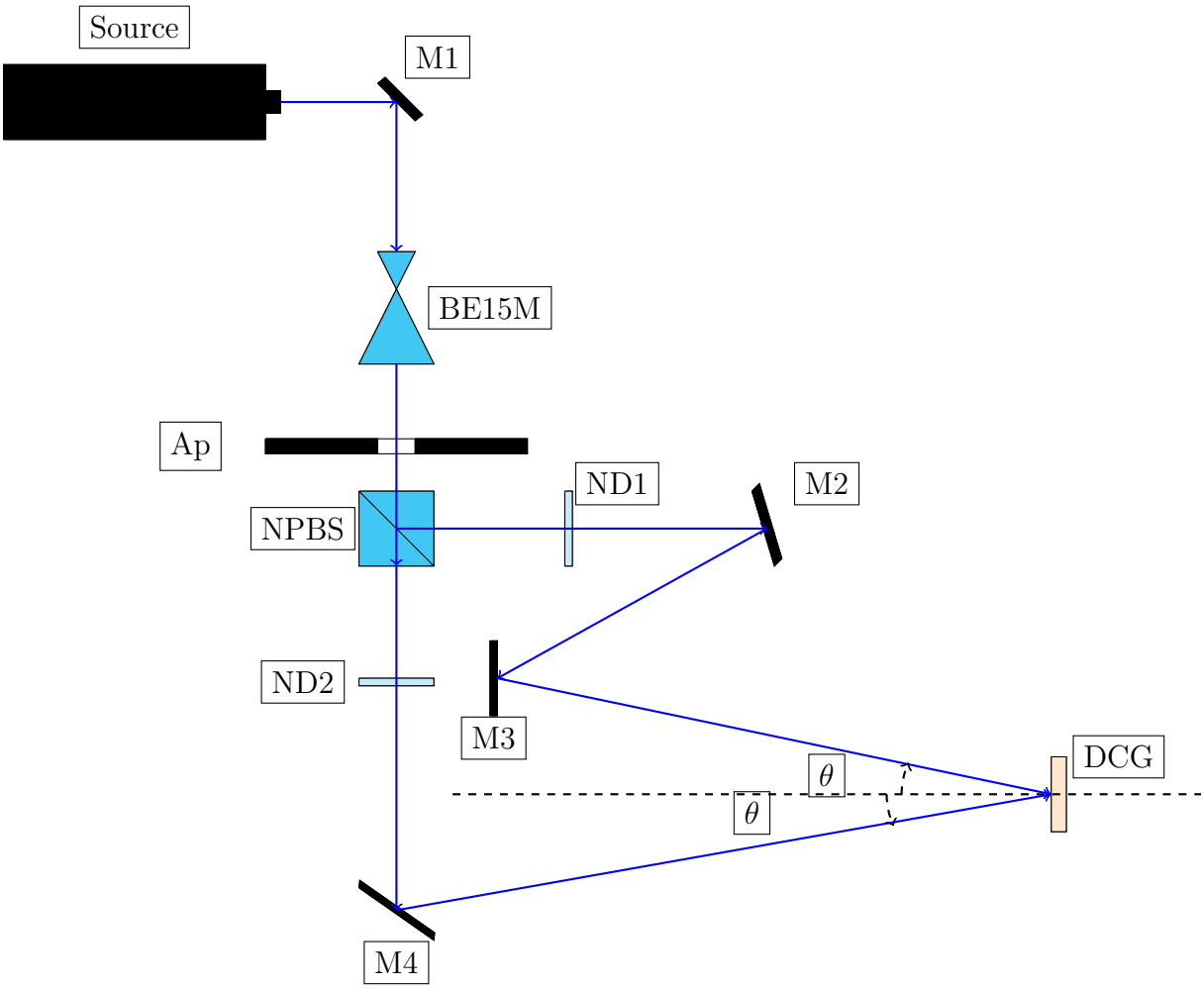

Figure 4.1: Set up for writing the first prototype of the RGB transmission volume hologram

Figure 4.1 depicts the set up used for writing the holographic optical element inside the dichromated gelatin (DCG) thin film. Due to the availability of only one light source, which is a blue laser-diode, the arrangement of all mirrors shown in Figure 4.1 is such that the two beams arrive at interference plane at angles of $\theta = 16^o$ with respect to the normal to the surface of the DCG thin film. The theory assumed plane waves, so the beam will need to be collimated as well. The illumination source is a Coherent Genesis blue laser-diode system operating at a wavelength of $\lambda = 460nm$ and having an output power of 1 Watt. The beam from the laser is incident on the surface of a mirror, M1, at an angle of 45^o with respect to the normal to the surface of M1. After reflection off the mirror, the beam is expanded using a Thor Labs 15X beam expander (BE15M) to produce a beam diameter of about half a centimeter. The iris (Ap) is placed right after the beam expander to stop down the size of the beam. The re-sized beam is split into two equal beams using a 50/50 non polarizing beam splitter (NPBS). Half of the light is transmitted through the beam splitter and the other half is reflected in a direction perpendicular to the transmitted one. The two beams are re-directed via the use of mirror M2, M3, and M4 and then recombined at the surface of the dichromated gelatin (DCG) thin film to interfere. The introduction of the neutral density filters, Thor Labs NE2 series, in the paths of the two beam is to balance the intensity of the beams before they interfere. The choice of the neutral density filters is made to compensate for the imperfection in the splitting ratio of the beam splitter NPBS.

For each of wavelengths of light, red or green, or blue, the incidence angle can be calculated using Equation 3.2. Table 4.1 shows the design parameters for the transmission volume hologram.

Table 4.1: Design parameters of the RGB transmission volume hologram

$\lambda(\mu m)$	$t(\mu m)$	$n_a v$	Δn	$\theta_{air}(^o)$
460	12	1.5	-	16
532	12	1.5	-	18.6
632	12	1.5	-	22.3
RGB	12	1.5	0.022	-

Since the two beams are assumed to be plane waves, it is expected that the interference pattern generated inside the active region of the hologram will produce straight line fringes in the refractive index. However, this assumption is not exactly true any movement or vibration can introduce a divergence in the beam. So it is expected that the diffraction efficiency produced by the written volume hologram is going to show a slight difference from the simulated diffraction efficiencies. Figure 4.2 shows pictures of a few prototypes of the volume hologram that were written at RL Associates in Pennsylvania. We attribute the difference in the appearance of the holograms to the limited knowledge of the chemical processing of the holograms after recording and the control of the exposure time of the thin film to the beams.

Figure 4.2: Picture of our first prototypes of the volume hologram, written at RL Associates.

4.3 Effect of the Laser Exposure Energy

The profile of the refractive index within the active region of the volume hologram is a function of several parameters, which include the exposure energy of the laser beam. The refractive index modulation is a function of this energy for low exposure energies; however at higher exposure energies, the index modulation is saturated to its maximum value. At the higher energies, the effect of the exposure energy mainly changes the magnitude of the diffraction efficiency at higher diffraction orders, but not the diffraction efficiency of the first order. However this same effect will affect the profile of the refractive index when the highest refractive index modulation is reached. When the modulation is saturated, increase in the energy of the laser beam will lead to broadening of the top part of the refractive index profile and narrowing of the bottom part. This behavior can be described using the empirical equation (Schutte and Stojanoff, 1997), Equation 4.4,

$$n = n_{av} + 2\Delta n_{max}\left[1 - e^{-\sqrt{\zeta^*\left(1+\cos\left(\vec{\boldsymbol{K}}.\vec{\boldsymbol{r}}\right)\right)}}\right]^2, \tag{4.4}$$

where n_{av} is the mean refractive index, Δn_{max} is maximum or saturation refractive index modulation, $\vec{\boldsymbol{K}}$ is the grating vector, and $\vec{\boldsymbol{r}}$ is the space vector. ζ^* is an experimental constant that relate the exposure energy E to an experimental material constant E_M and is defined using Equation 4.5, (Schutte and Stojanoff, 1997)

$$\zeta^* = \begin{cases} \left[\frac{E}{E_M}\right]^2 \cdot \zeta_M, if E < E_M \\ \sqrt{\frac{E}{E_M}} \cdot \zeta_M, if E > E_M. \end{cases} \tag{4.5}$$

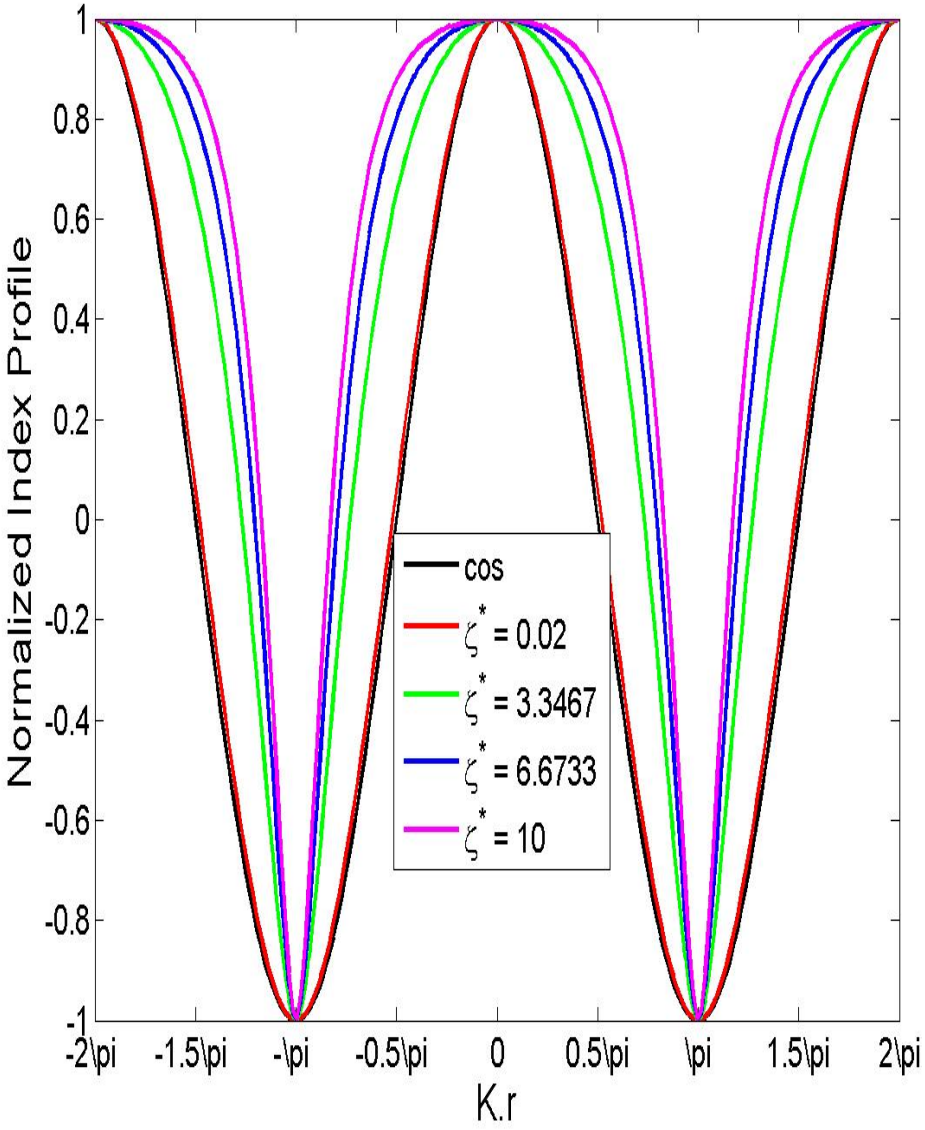

Figure 4.3: Simulated normalized refractive index profile as a function of $\vec{K}.\vec{r}$ for five different laser energies

Figure 4.3 shows the change in the profile of the refractive index within the active region of the volume hologram as a function of $\vec{K}.\vec{r}$ for five different laser energies (Schutte and Stojanoff, 1997). The results of this simulation show that when the energy is not too high and the index of refraction modulation did not reach its maximum, the profile of the refractive index within the active region is cosinusoidal. However, as the energy is increased then the profile tend to deviate away from its cosinusoidal shape. Furthermore, when the modulation maximum is reached, an increase in the energy of the laser will deform the shape of refractive index by enlarging the top and diminishing the bottom as shown in Figure 4.3.

4.4 Development and Curing of the Holographic Optical Element

Dichromated gelatin was determined by many studies (Stojanoff et al., 1994; Stojanoff, 1997; Sheel, 1990; Tropartz et al., 1991) to be one of the best light sensitive materials that could be used for the development of volume holographic grating via the interference of coherent light. Although the recording of the grating is done via interference of coherent beams, some chemical processing needs to be done on the written hologram before one can finalize its fabrication process to meet the design requirements. While the chemical process is important in the development of the holographic optical element (HOE), its precise control is most crucial as it affects the optical, physical properties, and the spectral characteristics of the HOE (Schutte and Stojanoff, 1997). The chemical phase in the fabrication of the volume hologram includes several processes: swelling of the DCG to create the refractive index modulation needed to form the periodic structure, hardening and fixing of the gelatin, and a dehydration after swelling to fix the modulation generated. A hardening process is

used to make sure that the DCG thin film does not deteriorate during the swelling process. Deterioration of the DCG will result from the fast expansion, or hot drying of the film. Table 4.2 shows the list of chemicals used to make the swelling, hardening and fixing baths used in the development of the first prototypes.

Table 4.2: Fixer and Hardener chemical components and their quantities (Billmers, 2015)

Chemical Supplies	**Quantity**
60% Ammonium Thiosulfate $(NH_4)S_2O_3)$ solution	$475ml$
Acetic Acid, Glacial $(C_2H_4O_2)$	$15ml$
Sodium Sulfate $(NaHSO_4$	$21g$
Boric Acid $(H3BO_2)$	$10.5g$
Distilled Water (H_2O)	as needed
Aluminum Sulfate $(Al_2(SO_4)_3)$	$28g$
Sodium Bisulfate $(NaHSO_4$	$2.6g$

The swelling of the DCG must be controlled in such a way that all parts of the film are swell at the same rate. Inhomogeneous swelling and shrinking of the DCG will cause the lamellar structure of refractive modulation to bend and affect the spectral response of the volume hologram.

4.4.1 Preparation of the Development Chemical Baths

The process of mixing the chemicals for the fixing and hardening of the holographic optical element can be done in two parts; preparations of the fixing and preparations of the hardening baths. This process is not light sensitive and can be performed prior to exposure of the DCG film. All baths were heated to a temperature of $50-55^oC$, except for the last 100% Isoproponal bath at 57^oC, prior to being used for the development of the HOE.

The fixer is prepared by mixing 475 ml of 60% Ammonium Thiosulfate solution with 21 g of Sodium Sulfate in a brown bottle and stirring the chemical composition until it is entirely mix and dissolved. Next, add 15 ml of Glacial Acetic Acid and 10.5 g of Boric Acid to the dissolved solution and stir the solution to mix all chemicals. The last components to be added are acids and may cause skin irritations; so one must be cautious when adding into and stirring the solutions. Add distilled water to the final solution to bring the water and chemical mix to a liquid volume of 1000 ml. Seal the brown bottle containing the prepared solution and store in a safe area.

Having the fixer bath done and set aside, the hardener bath needs to be prepared as well. The hardener is prepared by first mixing 28 g of Aluminum Sulfate with 60 ml of distilled water. Add 2.6 g of Sodium Bisulfate to the solution and stir well until all solids are completely dissolved. Again add distilled water to bring the final solution to a volume of 100 ml.

Although both fixer and hardener baths are prepared separately, the final solution used to accomplish these tasks, is a mixer of both solutions with water, into one chemical container. The water added to the solutions, serves as the swelling agent. The fixer hardener bath is made by mixing 100 ml of the fixer solution with 10 ml of

the hardener and 200 ml of deionized water.

The dehydration phase of the chemical development is composed of several baths with different composition of Isoproponal and water. For the development of the prototypes discussed in this dissertation, four different baths were used to complete the dehydration of the dichromated gelatin thin film. The baths were used, starting by the composition with lower percentage of Isopropanol to initiate the dehydration to a 100% Isopropanol to finish the dehydration. The purpose of the bath with low Isopropanol is to stop the swelling of the dichromated gelatin and initiate the dehydration process. The final step is to use a 100% isopropyl bath to completely dry the DCG. Table 4.3 shows the concentration of alcohol as well as the ratio of alcohol to water volume for all the dehydration baths that were used in the development process.

Table 4.3: Fixer and Hardener chemical components and their quantities (Billmers, 2015)

Concentration	**Volume (ml)**	**Volume of 70% Isopropyl (ml)/Volume H_2O**	**Volume of 100% Isopropyl (ml)**
25%	500	167/333	125
50%	500	333/167	250
75%	500	NA	375
100%	-	NA	500

Start by heating the solutions to their required temperatures as indicated in Table 4.4. Remove the HOE from the writing set up, and identify the film and the BK7 substrate sides. Insert the written hologram into the fixer/hardener bath and let it sit in the bath for one minute to one minute and a half. The chemical exposure process will create the refractive index modulation and fix it so that the interference

pattern stays permanently within the thin film. Next, remove the HOE from the fixer/hardener bath and place it into the distilled water, and let it sit for two minutes, to swell the film. The central wavelength can be shifted and adjusted by changing the exposure times in the hardener/fixer or the distilled water baths. However, if the time is reduced then, one might not remove all of the dichromated ions from the written part of the DCG, and will result with an unstable HOE. During the swelling process, the DCG thin film's thickness may go up to ten times its original thickness; so, a shrinking process is needed to bring the thickness back to its original value. The swollen HOE is then remove and placed in a 25% Isoproponal bath to initiate the dehydration/shrinking. The dehydration process is done in several steps using an increasing percentage of Isopropanol baths to dehydrate the DCG thin film slowly in order to avoid cracking on surface of the hologram. The last dehydration bath contain 100% Isopropanol to completely dry the HOE.

Now that all the chemical development is done, the dichromated gelatin is removed from the last Isopropanol bath and dried using a hair dryer. The HOE is supported at an angle of $45-60^o$, then blown with the dryer at low temperature until completely dry.

Table 4.4: Fixer and Hardener chemical components and their quantities (Billmers, 2015)

Bath	**Name**	**Time**	**Temperature**
1^{st}	Hardener/Fixer	1-1.5 min	$50^o - 55^oC$
2^{nd}	Distilled Water	2 min	$50^o - 55^oC$
3^{rd}	25% Isopropanol	0	$50^o - 55^oC$
4^{th}	50% Isopropanol	1 min	$50^o - 55^oC$
5^{th}	75% Isopropanol	1 min	$50^o - 55^oC$
6^{th}	100% Isopropanol	1 min	$50^o - 55^oC$
7^{th}	100% Isopropanol	1 min	57^oC

Table 4.4 shows the different baths used in the development process, their orders, exposure times , and temperatures.

4.5 Measurement of the Thickness of the DCG Film

The diffraction efficiency of the hologram is a function of several parameters, which include the refractive index modulation, the average refractive index, the incidence angle, and the physical thickness of the dichromated gelatin thin film. A change in any of these parameters will lead to a change in the efficiency of the diffracted light. In order to better understand the behavior of the written volume holograms, one should systematically investigate the deviation of some of the patterns from their nominal values; however after writing, the only parameter we were able to measure is the thickness of the film. Due to time and budget constraints we were not able to write multiple gratings with varying thicknesses. Also, the sample we obtained did not have strict control on the thickness.

The measurement of the thickness of the film was done using a commercial measurement device, the Filmetric F20 NIR thin film analyzer. This device can be used to measure thickness, some optical properties, such as refractive index and absorption constant, and reflectance and transmittance of most dielectric and semiconductors. Although, the Filmetric F20 NIR has all these capabilities, it was only used for measuring the thickness of the thin film.

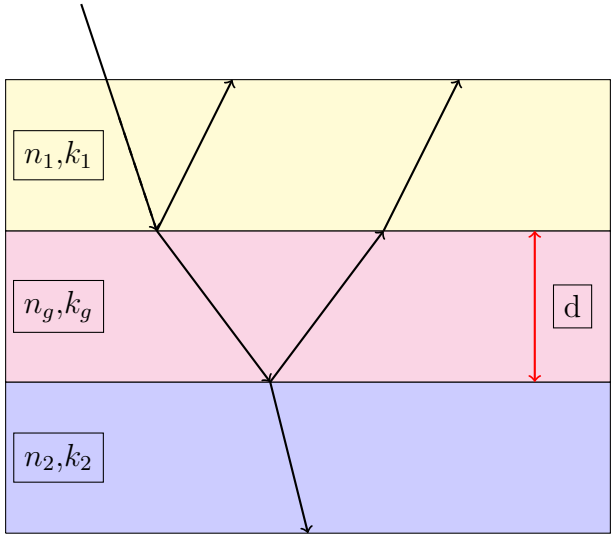

Figure 4.4: Reflection and refraction of the rays as they encounter interfaces between different materials.

Figure 4.4 depicts the technique used by the F20 NIR for measuring the thickness of thin films. This measurement technique determines the thickness of the film from the results of the interference between the lights that is partially reflected from the interfaces between the thin film, and its superstrate and substrate. The result of this interference (Tholl et al., 1995), when the reflected light waves are in-phase depend on the wavelength of light λ, and the thickness of the DCG thin film d, and the average refractive index n_{av},

$$\frac{4\pi}{\lambda} d n_{av} \sqrt{1 - \frac{n_{air}}{n_{av}} \sin\theta^2} = m\pi, \tag{4.6}$$

where θ is the angle of incidence, and n_{air} is the refractive index of air. In Equation 4.6, λ denotes the wavelength of light, n_{av} is the average refractive index of the DCG thin film, d is its thickness, and m is an integer. The filmetric F20 NIR uses an internal Halogen lamp, and a spectrometer with wavelength ranging between 950nm

and 1700nm; and can measure thicknesses between $100nm$ and $250\mu m$ with a precision of $0.1nm$ and a stability of $0.12nm$.

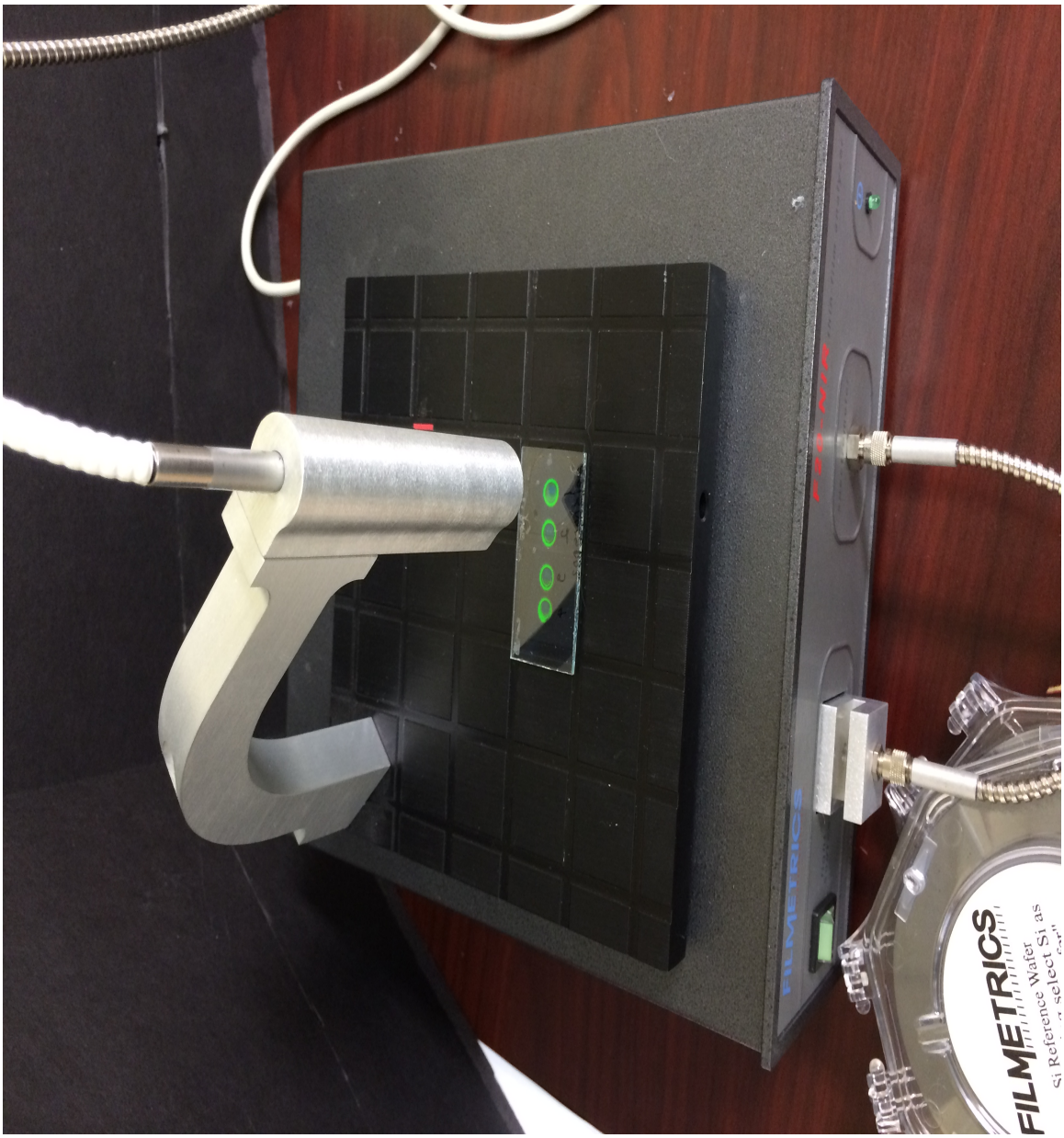

Figure 4.5: Measurement of the thickness of a DCG thin film at RL Associates using the F20NIR.

Figure 4.8 shows the set up for measuring the physical thickness of the DCG thin film used for the prototypes. In this figure, the light source used is coming from the overhead halogen lamp. The thin film is glued over a $3mm$ thick BK7 substrate and placed over a flat reference board.

After the writing and chemical development of the first prototypes, we proceeded to measure the thickness of each using the F20 NIR. Based on experience and common sense, it was assumed that the thickness of the film is never constant throughout the entire diameter of the recorded holographic optical element. To ensure high accuracy on the measurement of the thickness of the DCG thin film, ten different measurements were taken around the three holograms. Figure 4.9 shows the ten different locations on the thin film that were used to measure the thicknesses.

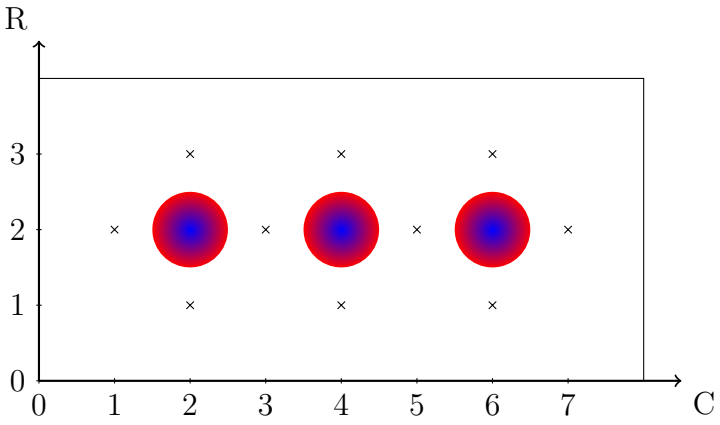

Figure 4.6: Layout of the locations used to determine the average thickness of each hologram.

For each written hologram, the average thickness of the dichromated gelatin is calculated as the average value of the four measurement data around it as,

$$d_{av} = \frac{\sum_{x=1}^{4} d_x}{4}, \tag{4.7}$$

where d_x are the individual thickness values, and x is an integer number between 1 and 4.

Although, it is obvious that only four values can't be assumed to provide an accurate thickness measurement, it is definitely more acurate than just taking a measurement of the central region on the hologram. For each of the ten measurements taken, the F20 NIR provided an average value, and a standard deviation of the thickness variations around each point. Tables 4.5 and 4.7 provide the average thickness values for all the ten locations; whereas Tables 4.6 and 4.8 give their standard deviations.

Table 4.5: Measured Thickness for 004 prototype.

	C1	C2	C3	C4	C5	C6	C7
R3	-	11.678μm	-	20.622μm	-	25.610μm	-
R2	9.54μm	-	18.724μm	-	26.143μm	-	27.503μm
R1	-	14.619μm	-	25.557μm	-	27.816μm	-

Table 4.6: Standard Deviation for 004 prototype.

	C1	C2	C3	C4	C5	C6	C7
R3	-	0.001μm	-	0.002μm	-	0.008μm	-
R2	0.003μm	-	0.001μm	-	0.003μm	-	0.003μm
R1	-	0.003μm	-	0.001μm	-	0.003μm	-

Table 4.7: Measured Thickness for 005 prototype.

	C1	C2	C3	C4	C5	C6	C7
R3	-	24.293μm	-	26.629μm	-	28.132μm	-
R2	22.975μm	-	25.646μm	-	27.193μm	-	-
R1	-	17.739μm	-	21.212μm	-	16.247μm	-

Table 4.8: Standard Deviation for 005 prototype.

	C1	C2	C3	C4	C5	C6	C7
R3	-	0.002μm	-	0.009μm	-	0.007μm	-
R2	0.01μm	-	0.001μm	-	0.005μm	-	-
R1	-	0.001μm	-	0.005μm	-	0.003μm	-

Based on the results shown on the last four tables, it is easily noticeable that the average thickness of the dichromated gelatin thin film used for the writing of the volume hologram are not constant across the entire film and suggest that the DCG thin has the form of an optical wedge. From an optical point of view, it is expected that some type of phase shift would be introduced to fields of light that pass through the DCG.

4.6 Measurement of the Diffraction Efficiency

4.6.1 Experimental Set-Up and Measurement

In this section, the measurement of the diffraction efficiencies in the forward first order diffraction will be done and discussed. Although two prototypes were written, measurement of the diffraction efficiency was done on only one of them. The set up used in this section, as shown in Figure 4.7 can be used to measure the change in the diffraction efficiency versus wavelength, as well as the change in the diffraction efficiency versus incidence angle.

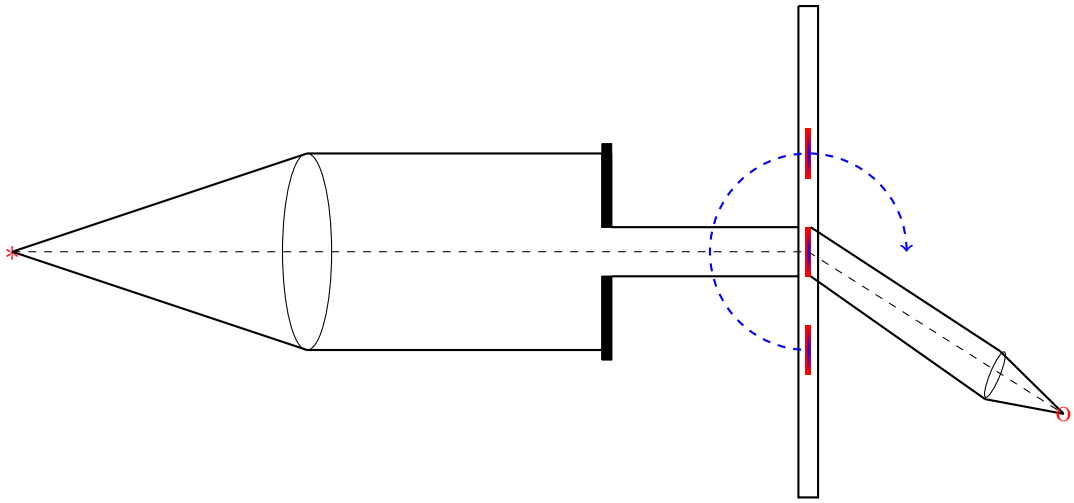

Figure 4.7: Set up for the measurement of the diffraction efficiency versus wavelength

In this case the illuminating source is a white light halogen lamp diverging out of an optical fiber. A collimating lens is placed approximately a focal length away from the source to focus the light infinitely far away. The iris placed in front of the collimating lens is used to stop down the beam, such that the light reaching the volume hologram fills the diameter of the written part of the film and no more. The holographic optical element is sandwiched between two $3mm$ BK7 cover glasses and placed on a rotation stage to allow rotation around the vertical axis. The reason for protecting the DCG thin film using the slabs of BK7 glasses is to protect it from dust as well as humidity. The rotation stage is used to change the angle of incidence of light, as the red, green, and blue lights are optimized at different angles of incidence. The assembly of the volume hologram and the rotation stage is then mounted on a translation stage to allow displacement in the direction perpendicular to the optical axis to make sure the beam of light is incident on the surface of the written hologram.

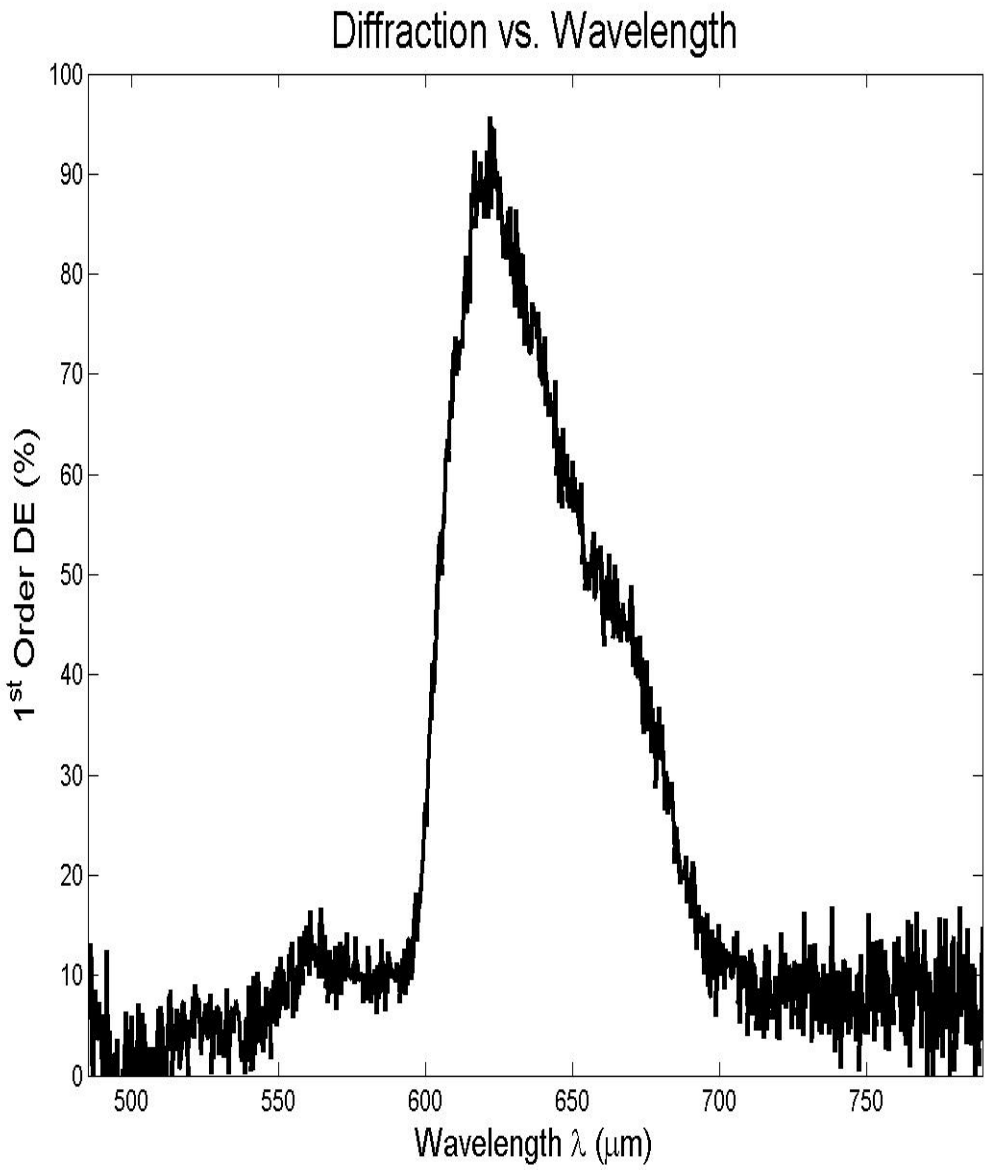

Figure 4.8: Measured diffraction efficiency versus wavelength for the first prototype.

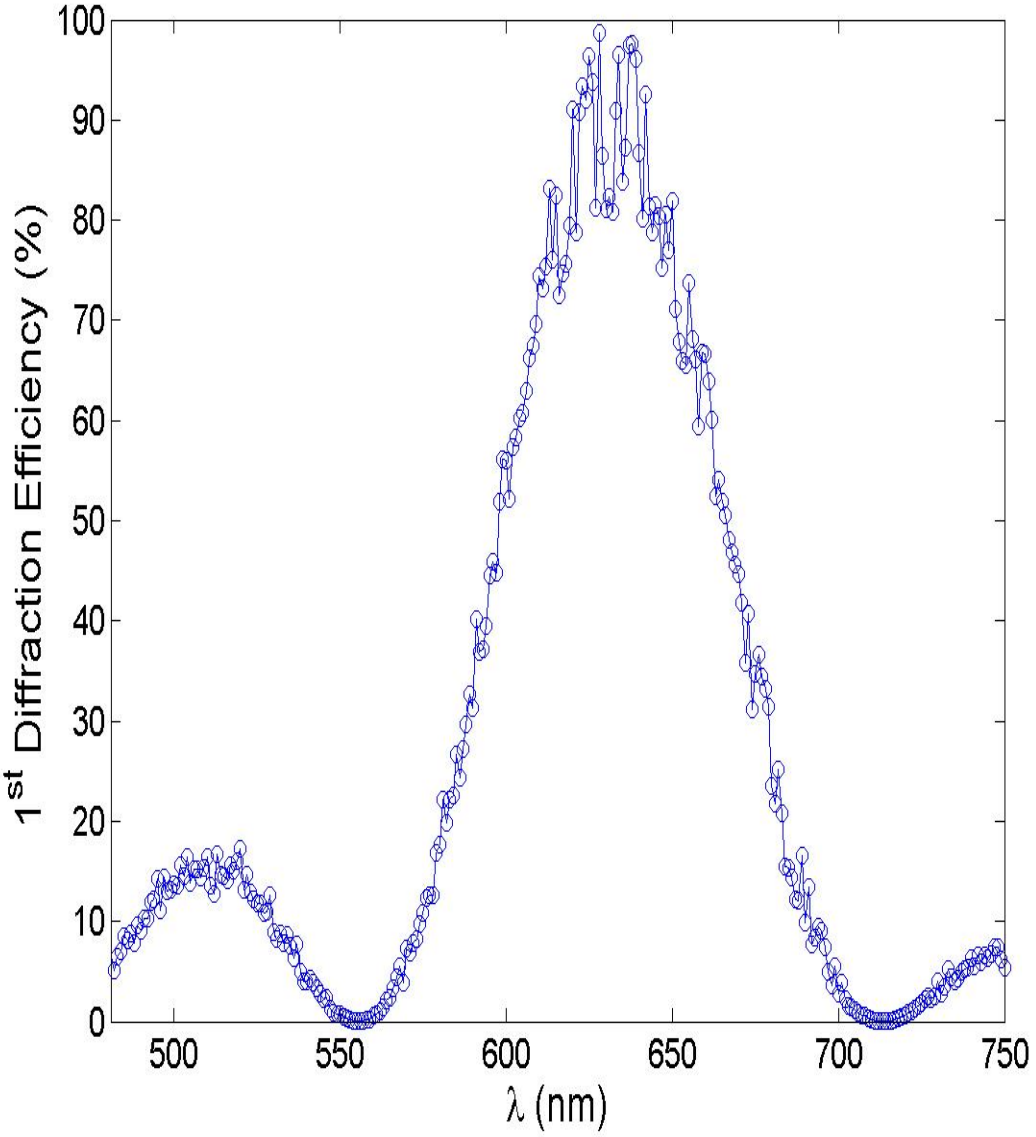

Figure 4.9: Simulated diffraction efficiency versus wavelength using the measured and calculated parameters based on the first prototypes

Figures 4.8 and 4.9 depict the measured and simulated diffraction efficiencies for first order diffraction of the first prototype. The simulated result is calculated using the physical thickness of the prototype as measured using the F20 NIR. The parameters used to simulated the diffraction efficiency plot in Figure 4.9 are a thickness of 22 μm, an average refractive index of 1.5, an index modulation of 0.017, and the incidence angle is 22^o. A comparison between the simulated and measured diffraction efficiencies is done on the next sub-section.

4.6.2 Comparison between the Simulated and Experimental Data

Although, experimental diffraction efficienies were measured for the written prototype, this dissertation will talk in detail about the differences and similarities between the simulated data and the measured ones. Measurements of the average thickness of the dichromated gelatin thin film yielded a value almost twice the nominal value of $12\mu m$. Based on this result and Equation 3.4, it is expected that the bandwidth of the diffraction efficiency as a function of wavelength to be half of the nominal value. Since the thickness of the film is different for the theoretically design hologram from the thickness of the physically written hologram, it is wise to re-simulate the diffraction efficiencies using the known parameters. In this case, the wavelength of light, the incidence angle, and the thickness of the prototype are known; however the refractive index modulation is unknown but can be calculated from the known parameters. Figure 4.10 shows three different plots of diffraction efficiencies versus wavelength on one axis. The plots shown on this figure depict the measured and simulated diffraction efficiencies as a function of wavelength, when the design wavelength is $632nm$. The plot specified by the black line with diamonds is the theoretically

simulated diffraction efficiency versus wavelength, when the thickness of the thin film used is d = $12\mu m$. The blue line with circular annotation is the simulated diffraction efficiency using the measured thickness, d = $22\mu m$, of the prototype, and the red line with asterisk is the measured diffraction efficiency of the prototype.

Comparison of these plots shows that the spectral bandwidth of the measured data (blue line) is near half of the bandwidth of the simulated data (black line) based on the original design parameters; however the bandwidths of the measured data (blue line), and the simulated data using the measured parameters are almost equal, but not quite. The mismatches between the latter two plots could be resulting from several factors that could range from misalignment of writing set up to improper chemical development of the hologram. Another factor that may have lead to the difference in the diffraction efficiencies between the experimental and simulated results could be the fact the laser beam was not spatial filtered and collimated before reflection off of the first mirror M1, Figure 4.1.

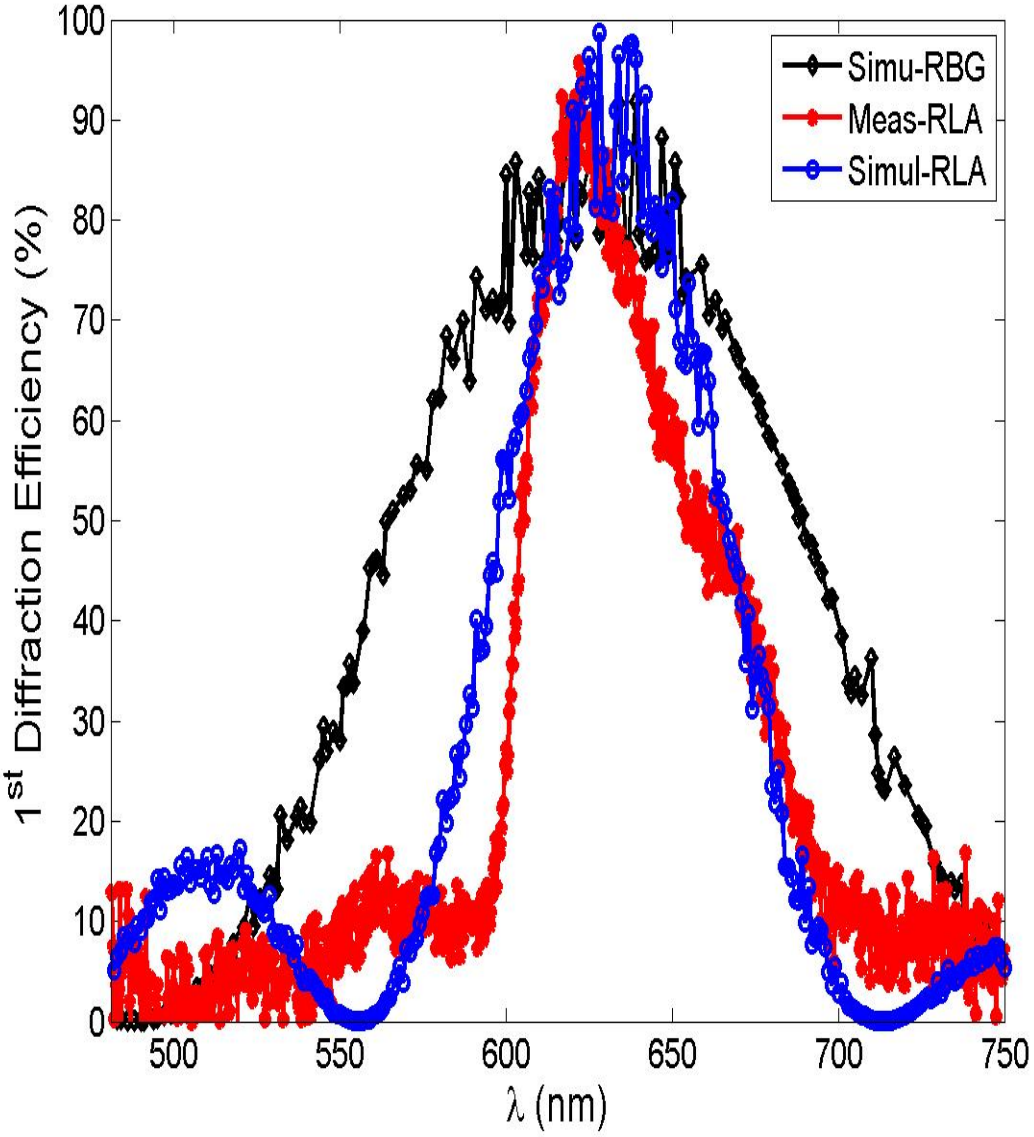

Figure 4.10: Plot of the diffraction efficiency versus wavelength for the simulated RGB optimized design diffraction as well as the simulated and diffraction measured for the first prototype.The Black line with diamond is the simulated RGB diffraction efficiency, and the blue with the asterisk, and the red with circles are the simulated and measured diffraction efficiencies for the prototype, respectively.

4.6.3 Conclusion

In this chapter the writing, chemical development, and experimental measurement of the diffraction efficiency for the designed hologram were discussed. The results of the comparison between the simulated and measured data showed that a great knowledge of the chemical development process is very important for making a good hologram. The experimentally measured data for the first prototype did not perfectly match simulated data; however, it is obvious that we need proper control of the development to produce better holograms.

Chapter 5

Polarimetric Characterization of the Volume Hologram

5.1 Introduction

Volume phase holographic gratings have been used in many applications for their diffractive nature. Although they diffract light via use of refractive index modulation within their active region, they also could introduce a phase shift to the waves that diffract through them. (Rytov, 1956; Born and Wolf, 1970; Yariv and Yeh, 1977; Kim et al., 1995) showed that infinetely stratified media, with sub-wavelength periods can behave like uni-axial crystals due their lamellar structure. Based on these facts, the volume hologram's refractive index modulation could be seen to be a lamellar structure of refractive index changes with sub-wavelength periods. When the period of the refractive index modulation is about an order of magnitude less than the wavelength of light, the periodic structure would introduce a phase shift between the TE and TM modes. This phase shift mostly affects the $\vec{\boldsymbol{E}}$-field waves, hence the polarization state of the incident light. Furthermore, there are other complicated factors that could add phase factors to the fields, such as surface non-uniformities at the interface between the BK7 cover glass and the DCG thin film. The phase retardances mark the birefringence property of the volume holographic gratings. The rise of birefringence in crystals is a consequence of the molecular structure of its composite materials, which would affect the propagation of light with different polarization properties. However birefringence can also arise from periodic arrangement of isotropic materials. This

alternating composition of isotropic materials could be viewed as one anisotropic medium.

The purpose of this chapter, is to investigate the polarimetric behavior of the transmission volume holographic grating. Moreover, the design of this volume hologram focused more on the demonstration of high efficiency when unpolarized light is incident; it did not constraint the hologram for 100% diffraction efficiency at this polarization state. Thus it is expected that the hologram will behave as a polarizer or retarder for wavelengths away from the design wavelengths, which are the Bragg wavelengths at specific angles of incidence.

5.2 Phase Difference and Birefringence

The volume hologram's refractive index modulation within the active region, is said to induce a phase retardance between the TE and TM modes of incident waves. The retardation is the difference between the phases of the polarization components of the field along the fast and slow axis of the hologram. This phase shift can be calculated using Equation 5.1 given by (Kim et al., 1995)

$$\Delta\Phi_{(TE-TM)_m} = \Phi_{TE_m} - \Phi_{TM_m}, \tag{5.1}$$

where $\Delta\Phi$ is the phase shift, Φ_{TE} and Φ_{TM} are the field phases for the cases of TE and TM incident waves, respectively, and m is the order of diffraction. The phase of the TE and TM modes were determined using the results of the rigorous coupled-wave analysis. Figure 5.1 depicts the phase retardance induced by the volume hologram ,between the TE and TM modes, as functions of wavelength.

The results of Figure 5.1 indicate that the first order forward diffracted orders through the volume hologram exhibit some phase shift at some wavelengths. This phase shift is mainly at wavelengths different than the design wavelengths. The reason for the low phase shift around the design wavelengths is because the volume hologram's refractive index modulation was optimized for unpolarized light as shown in Chapter 3, Section 3.3. Based on these results one can say that the volume hologram behaves like a crystal, which has an ordinary refractive index n_o for the case of the TE polarization, and an extraordinary refractive index n_e for the case of TM polarization. The difference between the ordinary and extraordinary refractive indices is the birefringence exhibited by the volume hologram.

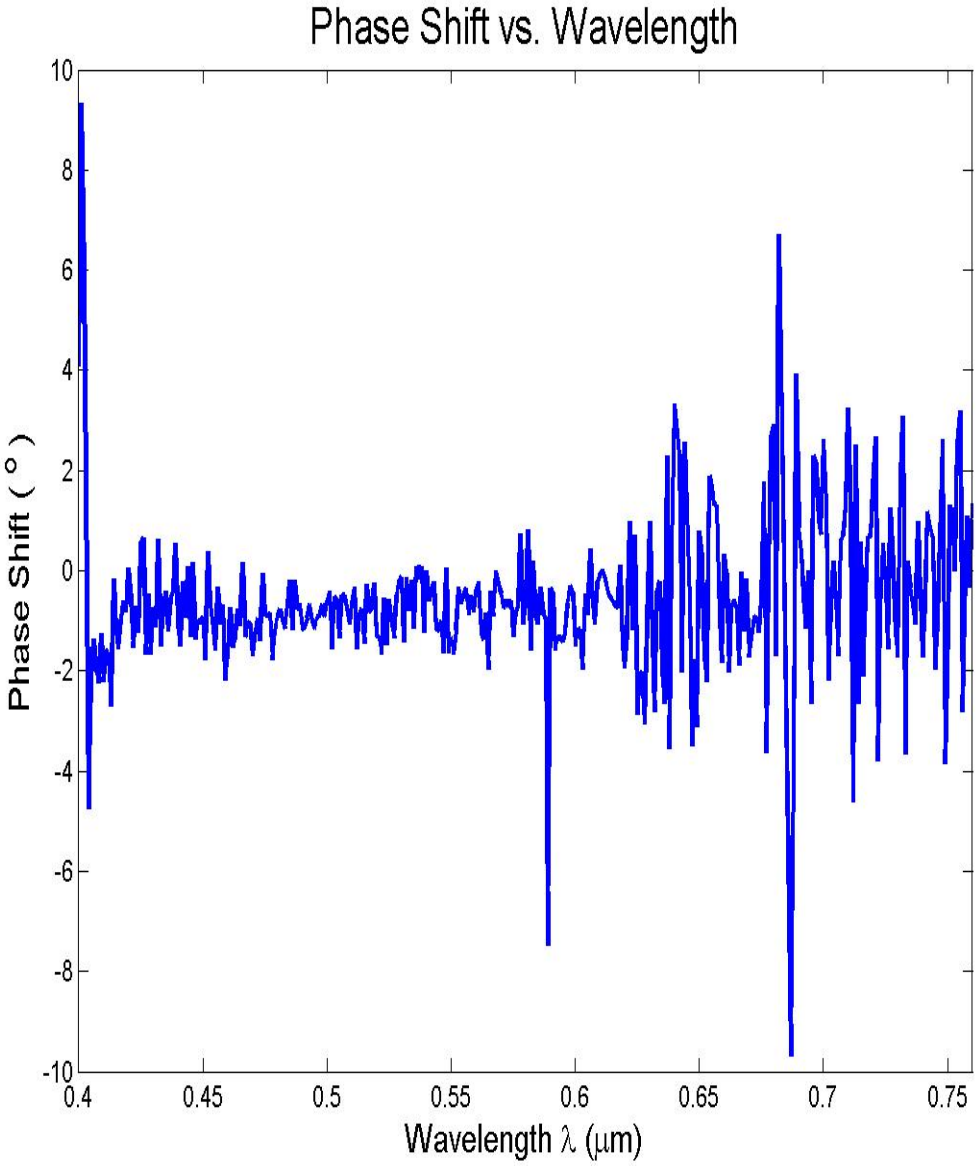

Figure 5.1: Phase retardation between the TE and TM modes as a function of wavelength.

5.3 Non-depolarizing Coherent Mueller Matrix

In the previous section, Figure 5.1 showed that the volume hologram can introduce a phase shift between TE and TM components of a propagating wave. In order to have a complete understanding of how the volume hologram's architectural form affects the optical properties of incident light, it is wise to investigate its Mueller matrix polarization signature, which is a 4×4 matrix. The Mueller matrix of the volume hologram can be calculated via the method of generalized ellipsometry, using the results obtained from the rigorous coupled-wave analysis. Generalized ellipsometry requires six polarization states: three incident states and their three corresponding diffracted polarization states. For the calculation of the phase retardation properties of the volume hologram, the complex waves used were determined for the case of TE and TM polarized incident waves. However, in order to prove the consistency between the results from Figure 5.1, and the calculated the Mueller matrix of the volume hologram, three new incident polarization states were considered, a wave polarized at 8.75^o, a wave polarized at 31.25^o, and a wave polarized at 62.5^o, rather than the TE and TM polarizations. For each of these polarization states, the rigorous coupled-wave analysis yielded another polarization state at the first order forward diffraction.

Substituting the incident and diffracted fields determined by the RCWA into the expressions of Equations 2.61-64 yielded the ratios of the elements of the coherent Jones matrix J, which can be used to calculate the coherent Mueller matrix via the method of (Azzam and Bashara, 1977). This coherent Mueller matrix is a nondepolarizing Mueller matrix which transforms a fully polarized incident beam of light into a fully polarized exiting beam of light (Azzam and Bashara, 1977; Chipman, 2005).

For a polarization element to be nondepolarizing, it must be an ideal polarization element.

In the general, a complete Mueller matrix has 16 elements, and is put in a 4×4 matrix form as,

$$MM = \begin{bmatrix} M_{00} & M_{01} & M_{02} & M_{03} \\ M_{10} & M_{11} & M_{12} & M_{13} \\ M_{20} & M_{21} & M_{22} & M_{23} \\ M_{30} & M_{31} & M_{23} & M_{33} \end{bmatrix}, \tag{5.2}$$

where the elements of the Mueller matrix are related to the following properties:

- M_{00} is the average intensity transmittance over all polarizations.
- M_{11} is the intensity transmittance when incident light is polarized horizontal or vertical.
- M_{22} is the average intensity transmittance when incident light is polarized 45^o or 135^o.
- M_{33} is the average intensity transmittance when incident light is polarized right or left circular.
- M_{01} and M_{10} represent the linear diattenuations oriented at 0^o and 90^o respectively.
- M_{02} and M_{20} represent the linear diattenuations oriented at 45^o and 135^o respectively.
- M_{03} and M_{30} represent the circular diattenuation.

- M_{21} and M_{12} represent the linear retardances oriented at 0^o and 90^o respectively.
- M_{31} and M_{13} represent the linear retardances oriented at 45^o and 135^o respectively.
- M_{23} and M_{32} represent the circular retardance.

Diattenuation is the property of optical elements or systems whereby the intensity transmittance of the exiting light is a function of the state of polarization of the incident light. It takes values between 0 and 1, and can be calculated using Equation 5.3,

$$\boldsymbol{D} = \frac{T_{max} - T_{min}}{T_{max} + T_{min}} = \frac{\sqrt{M_{01}^2 + M_{02}^2 + M_{03}^2}}{M_{00}}, \tag{5.3}$$

where D is the diattenuation, T_{max} is the maximum transmission and T_{min} is the minimum transmission.

Figure 5.2 depicts the coherent Jones-Mueller matrix of the volume hologram. This matrix is coherent, non-depolarizing, and can never be obtained exactly as it is using a polarization measurement device; that is because polarimetric systems tend to average over limited bandwidths. Figure 5.3 is the same as in Figure 5.2 except it only displays the elements of the Mueller matrix that mark the diattenuation and retardation properties of the volume hologram.

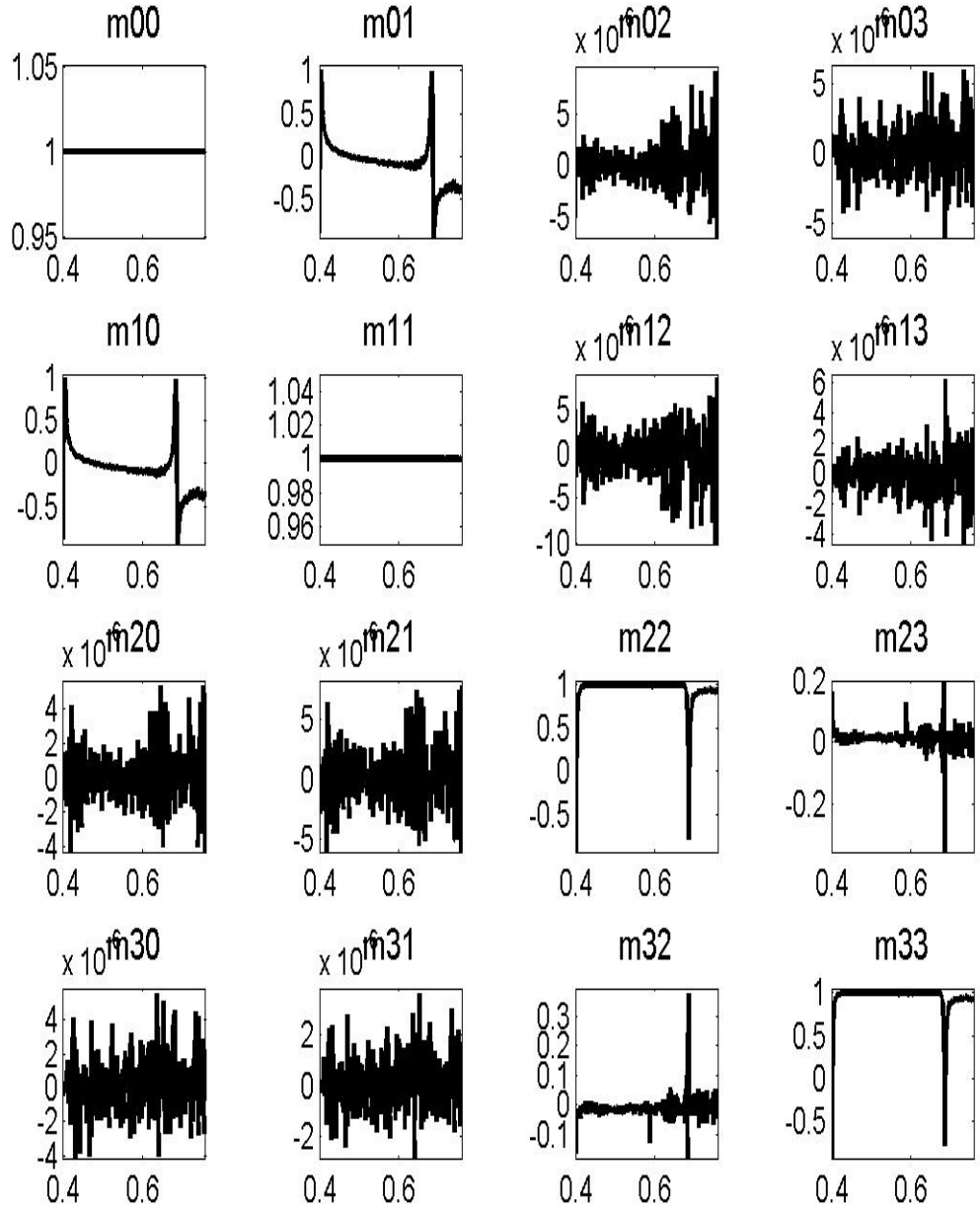

Figure 5.2: The Coherent Mueller matrix signature of the Transmission Volume holographic grating as a function of wavelength.

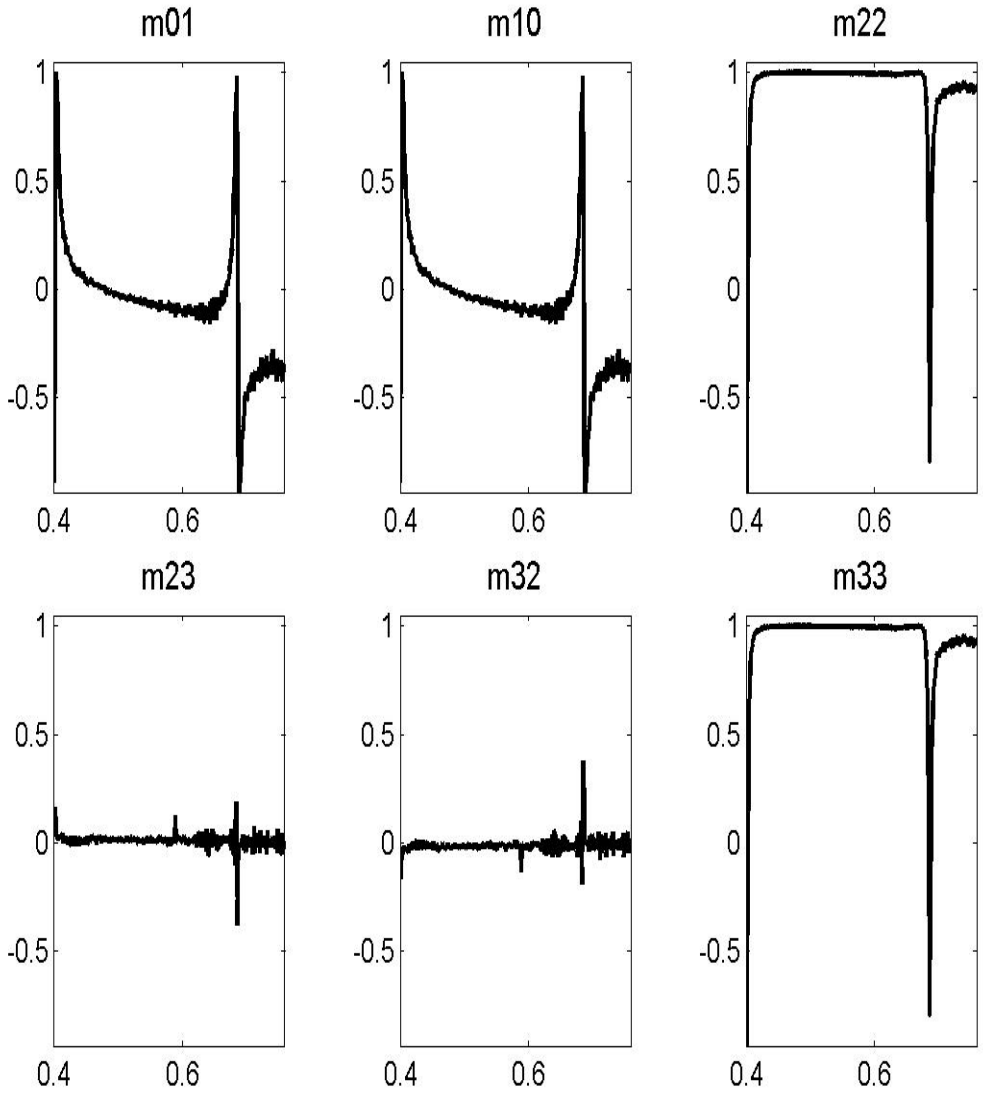

Figure 5.3: This plot shows the elements of the coherent Mueller matrix that represent the linear diattenuations in m_{01} and m_{10}, the average intensity transmittance when incident light is polarized 45° or 135° in m_{22} and m_{33} respectively. The element representing linear retardance are represented by m_{23} and m_{32}.

In order to obtain a Mueller matrix that makes sense, it is necessary to incorporate some depolarization properties (Chen et al., 2013, 2014; Otani, 2009).

5.4 Incoherent Mueller Matrix

The simulation of the Mueller matrix of the hologram has given us a 16 element Mueller matrix for each of the wavelengths; however, when an polarimetric system collects data it often does not consider each wavelength individually; it collects data by averaging over a spectral bandwidth, $\Delta\lambda$. As a proof of concept the results shown in Figures 5.2 and 5.3 are smoothed by convolution of the coherent Mueller matrix data with a rectangular filter of width $\Delta\lambda = 5nm$ in order to incorporate the depolarization properties of the spectral band limitation. The result obtained after convolution is a quasi-incoherent Mueller matrix that could be assumed to be similar to a measured data, if no other depolarization factors exist. Although this approach seem reasonable, the computed Mueller matrix will differ from a measured Mueller matrix data, due to the fact that measurement systems and environment add more depolarization properties; however if the polarimeter is known, using its spectral and angular bandwidths, one can simulate an incoherent Mueller matrix that is close enough to the measured one.

Recalling that the chemical development of volume hologram plays a big role on its functionality in terms of spectral and angular response (Schutte and Stojanoff, 1997; Stojanoff et al., 1991; Sobolev and Soboleva, 1994; Markova et al., 2011); it could also be a big factor in the polarimetric response of the hologram. While under chemical development, the thickness of the thin film can change and must be controlled else it will create a source of depolarization based on the non-uniform swelling of the DCG.

Figure 5.4 shows the plot of the sixteen elements of the incoherent Mueller matrix of the volume hologram, incorporating the depolarization effects induced by the spectral band limit of an imaging system with a bandwidth of $\Delta\lambda = 5nm$. Figure 5.5 is the same as in Figure 5.4 except it only displays the elements of the Mueller matrix that mark the diattenuation and retardance properties of the volume hologram. Figures 5.6-5.8 show the sixteen elements of the Mueller matrices at the wavelengths of $460nm$, $532nm$, and $632nm$, respectively.

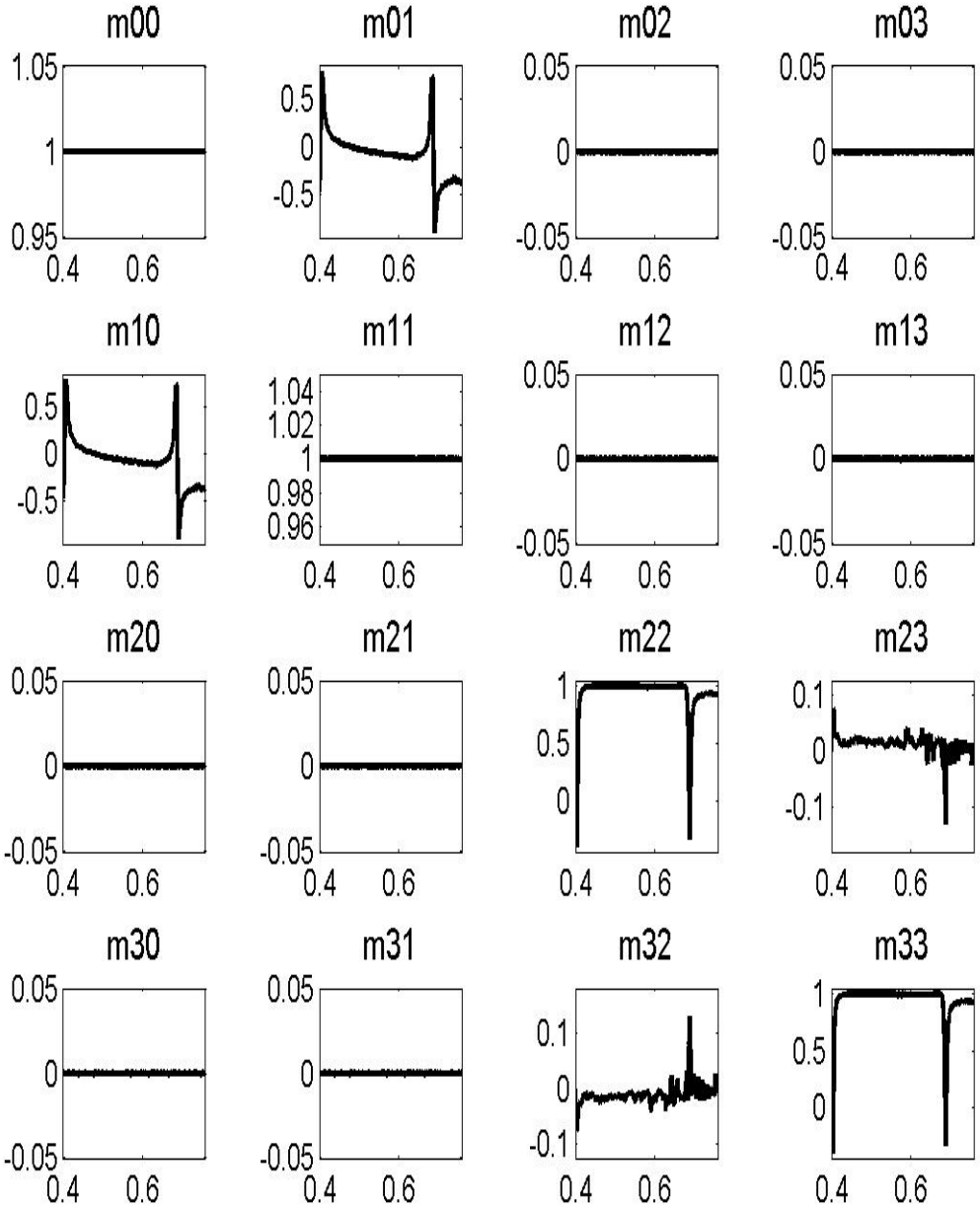

Figure 5.4: The Incoherent Mueller matrix signature of the Transmission Volume holographic grating as a function of wavelength.

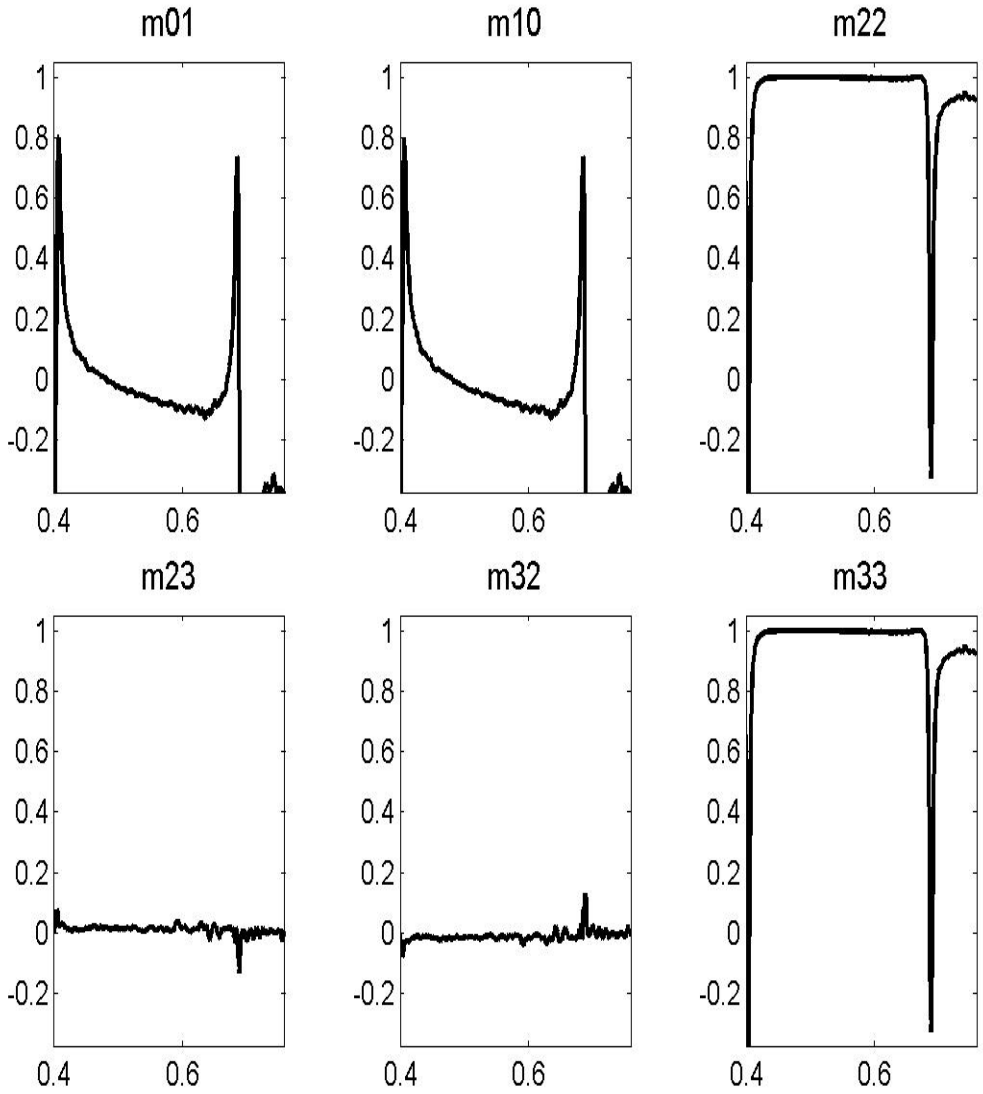

Figure 5.5: This plot shows the elements of the incoherent Mueller matrix that represent the linear diattenuations in m_{01} and m_{10}, the average intensity transmittance when incident light is polarized 45° or 135° in m_{22} and m_{33} respectively. The element representing linear retardance are represented by m_{23} and m_{32}.

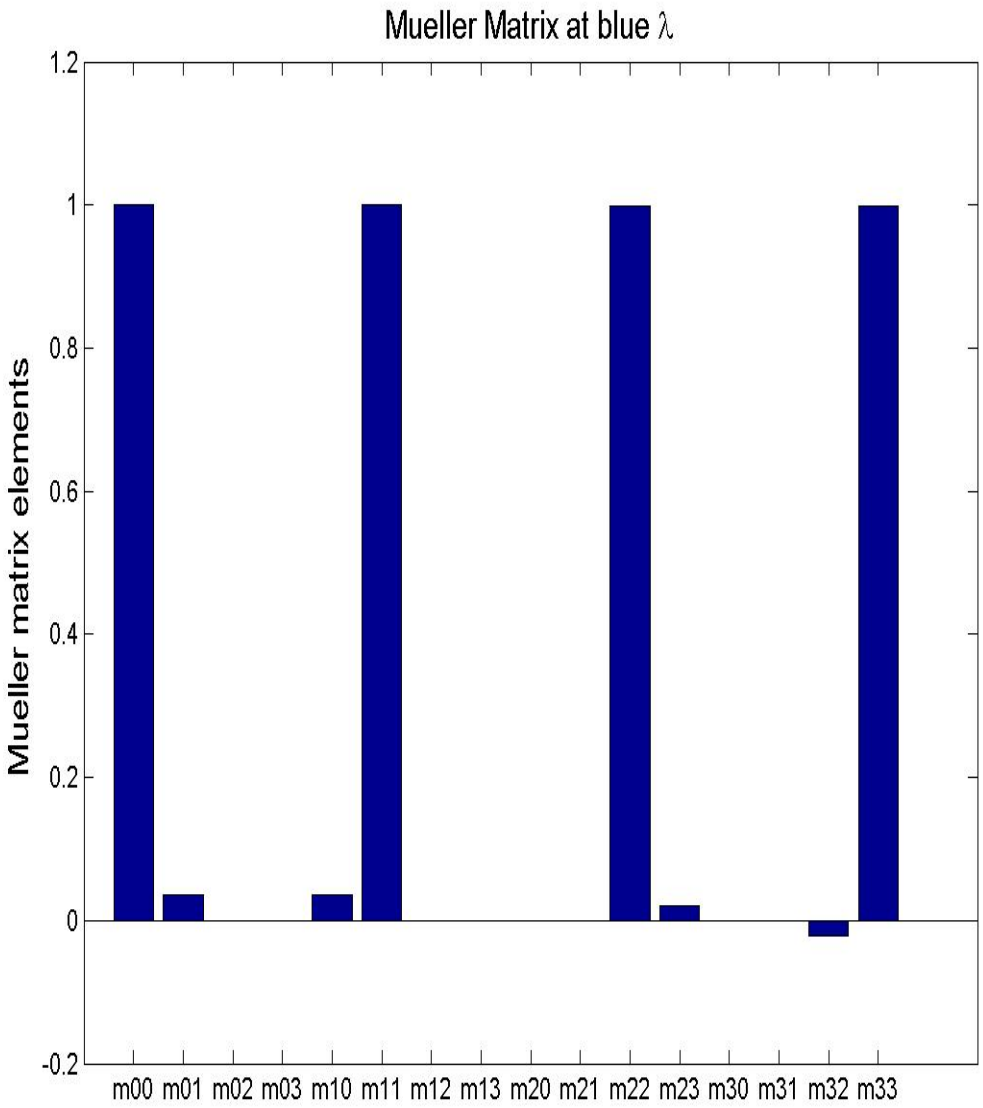

Figure 5.6: The Incoherent Mueller matrix signature of the Transmission Volume holographic grating when blue light is incident.

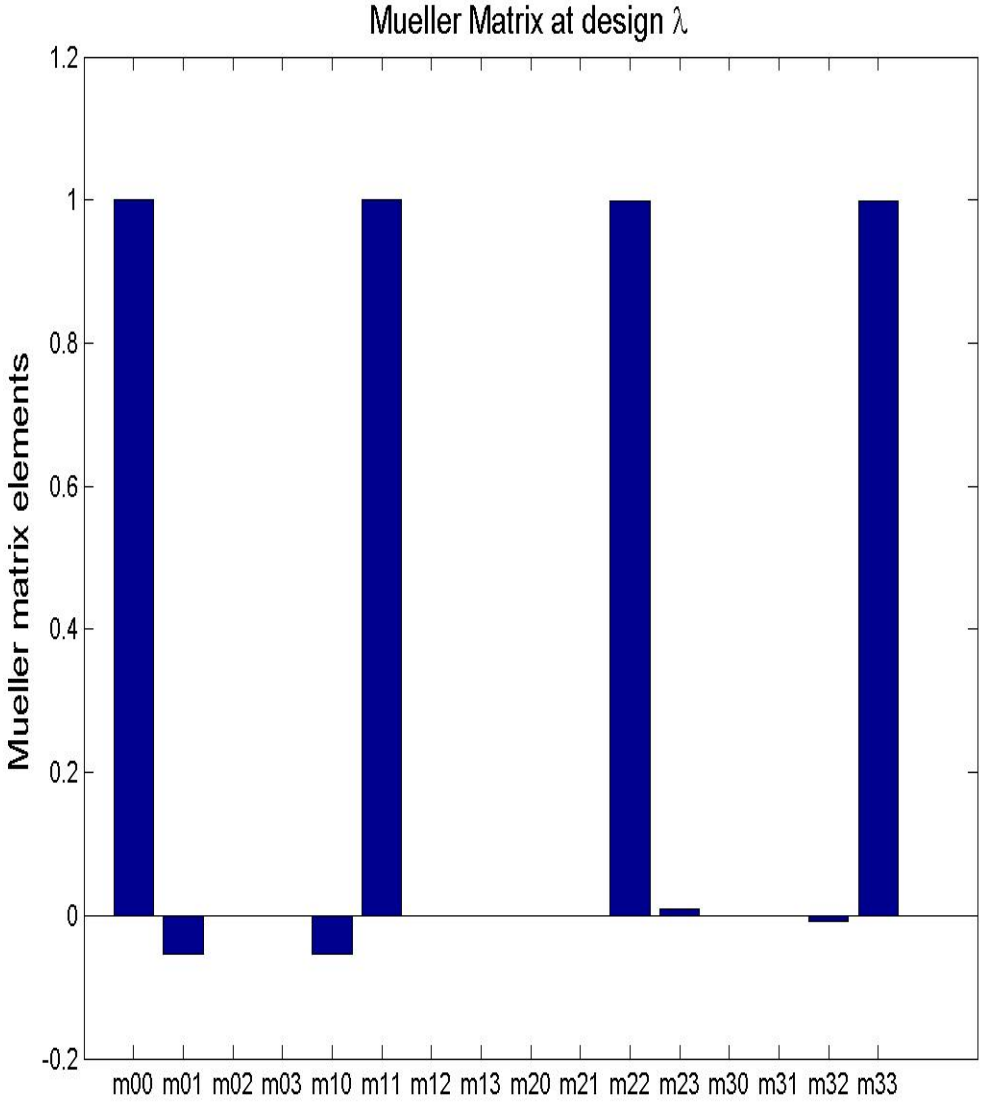

Figure 5.7: The Incoherent Mueller matrix signature of the Transmission Volume holographic grating when green light is incident.

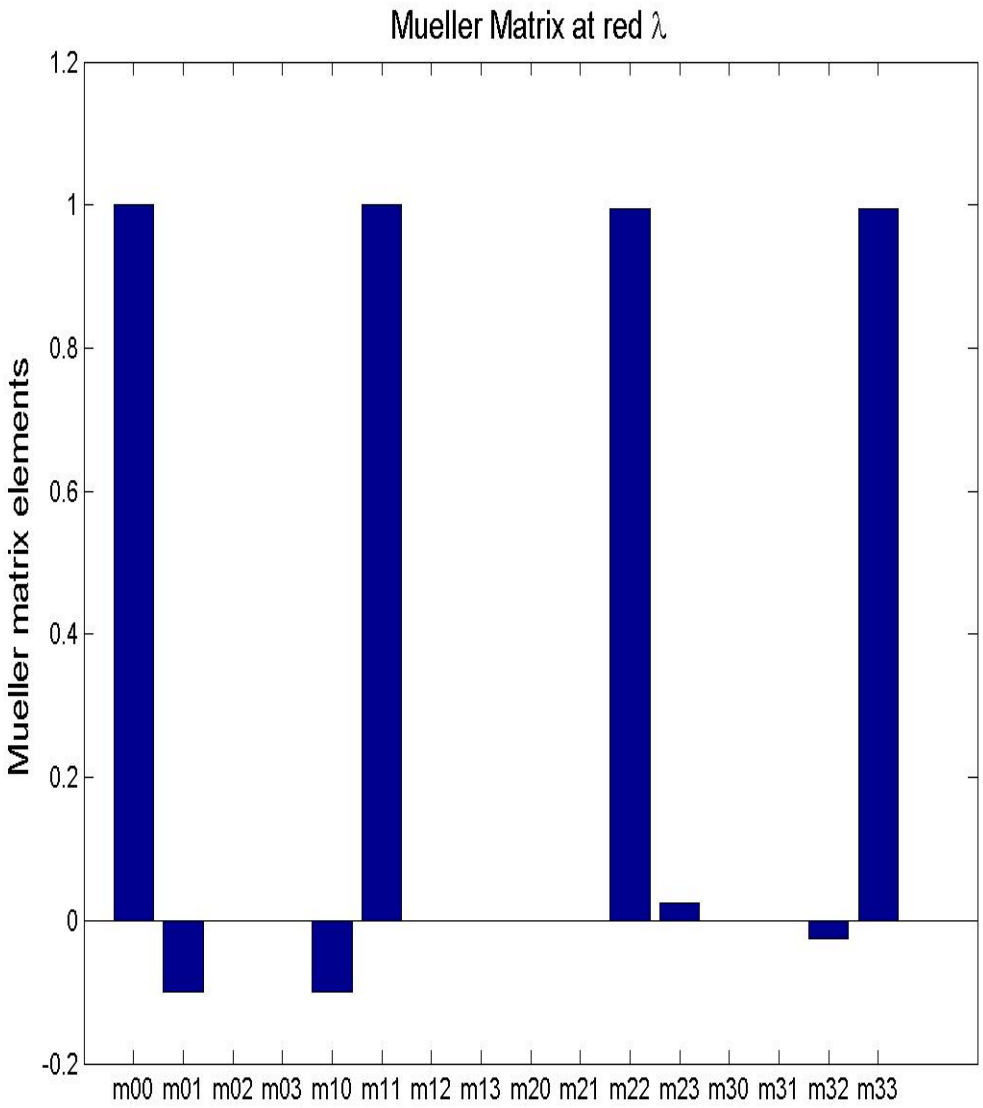

Figure 5.8: The Incoherent Mueller matrix signature of the Transmission Volume holographic grating when red light is incident.

The Mueller matrix bar plot depicted by Figure 5.6 shows that when blue light is incident at its Bragg angle, the elements of the Mueller matrix, m_{01} and m_{10}, which mark its diattenuation property are about 6%; and the elements, m_{23} and m_{32}, which show its retardance behavior are less than 5%. The Figure 5.7 also show results that are almost similar to the results of previous figure; however in this case, since the refractive index modulation was optimized for green wavelengths, it can be seen that the volume hologram act more like a weak polarizer rather a weak retarder as well. As the results of Figure 5.1 showed that the volume hologram exhibits more phase retardance in the regions between $600nm$ and $750nm$, it is expected that it will behave more like a retarder when red light is used, and one can notice it looking at the results of Figure 5.8; however the hologram acts like a weak polarizer as well, at this wavelength.

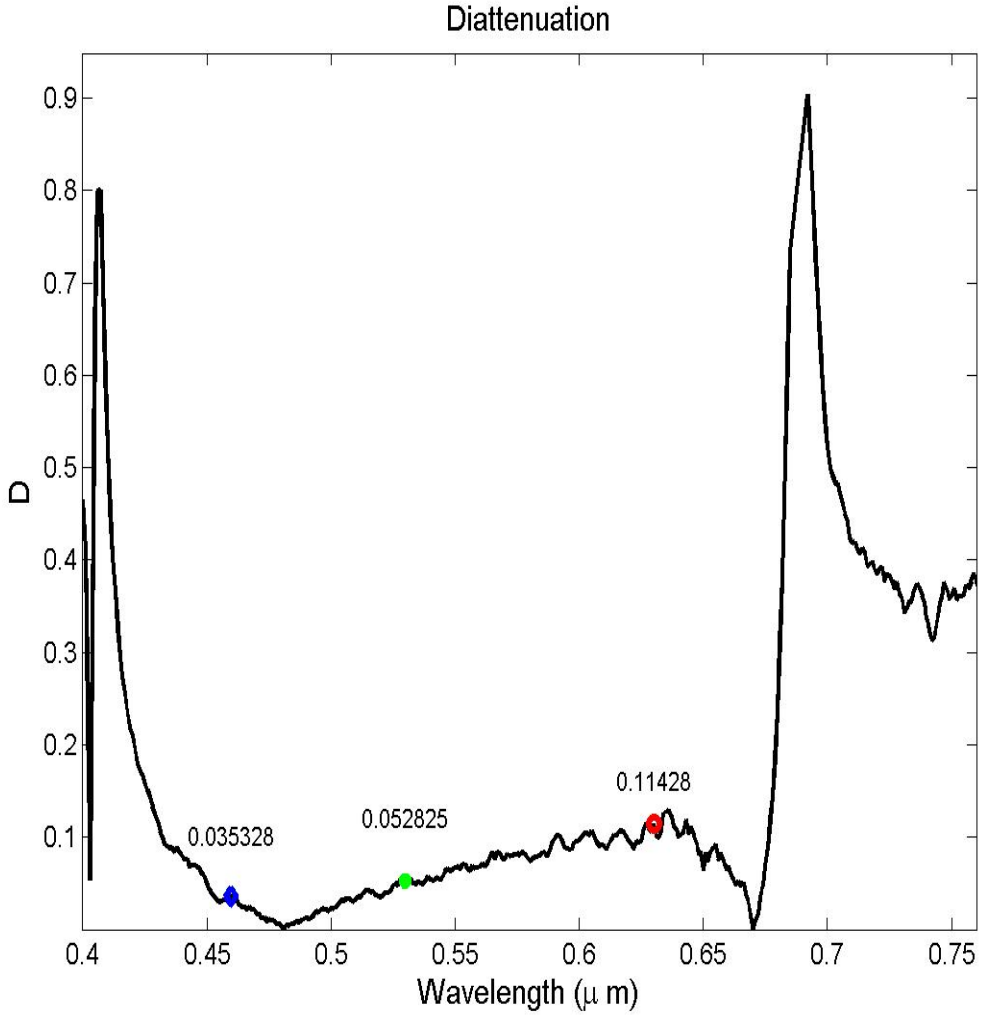

Figure 5.9: Diattenuation of the Transmission Volume holographic grating as a function of wavelength.

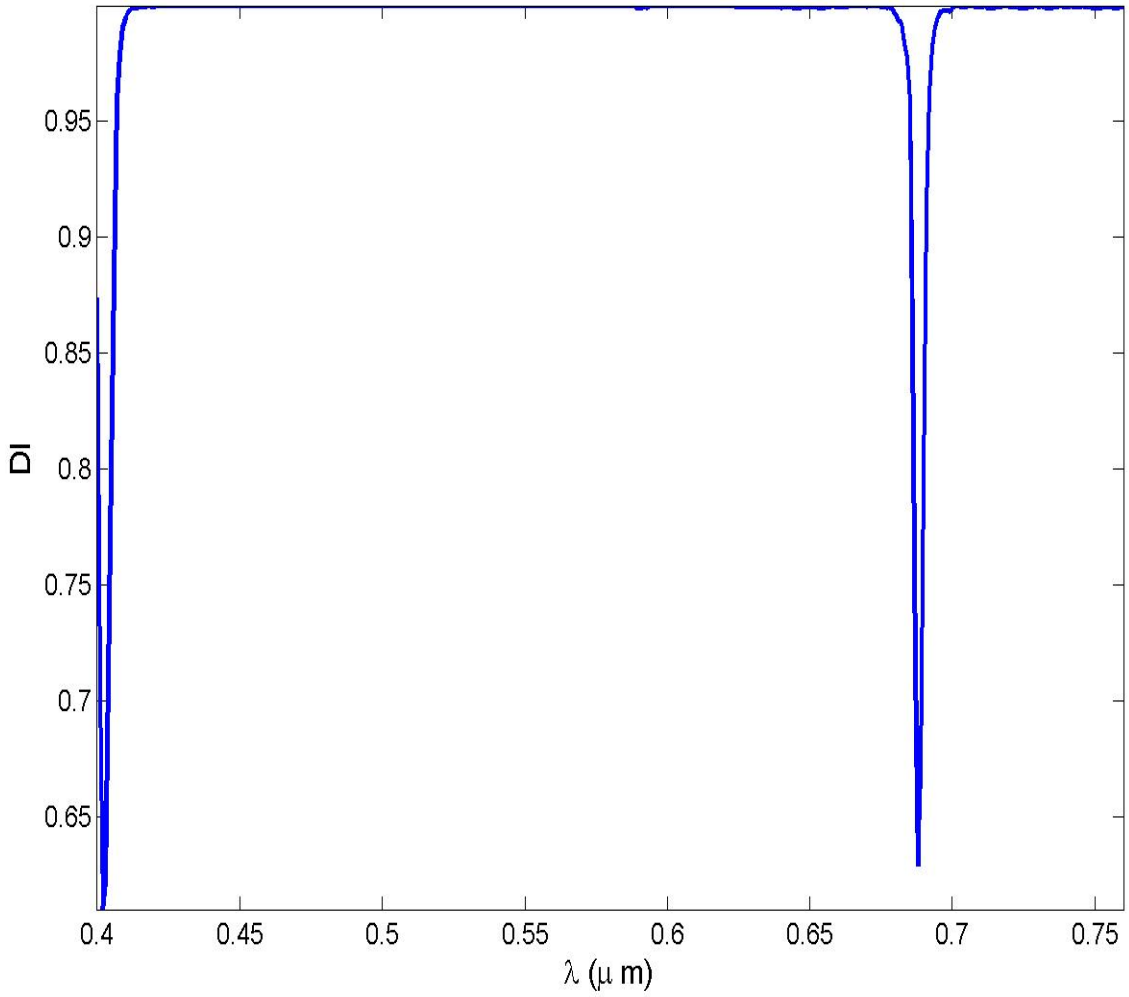

Figure 5.10: Depolarization index of the volume hologram's spectral band limitation. The spectral bandwidth is assumed to be $\Delta\lambda = 5nm$.

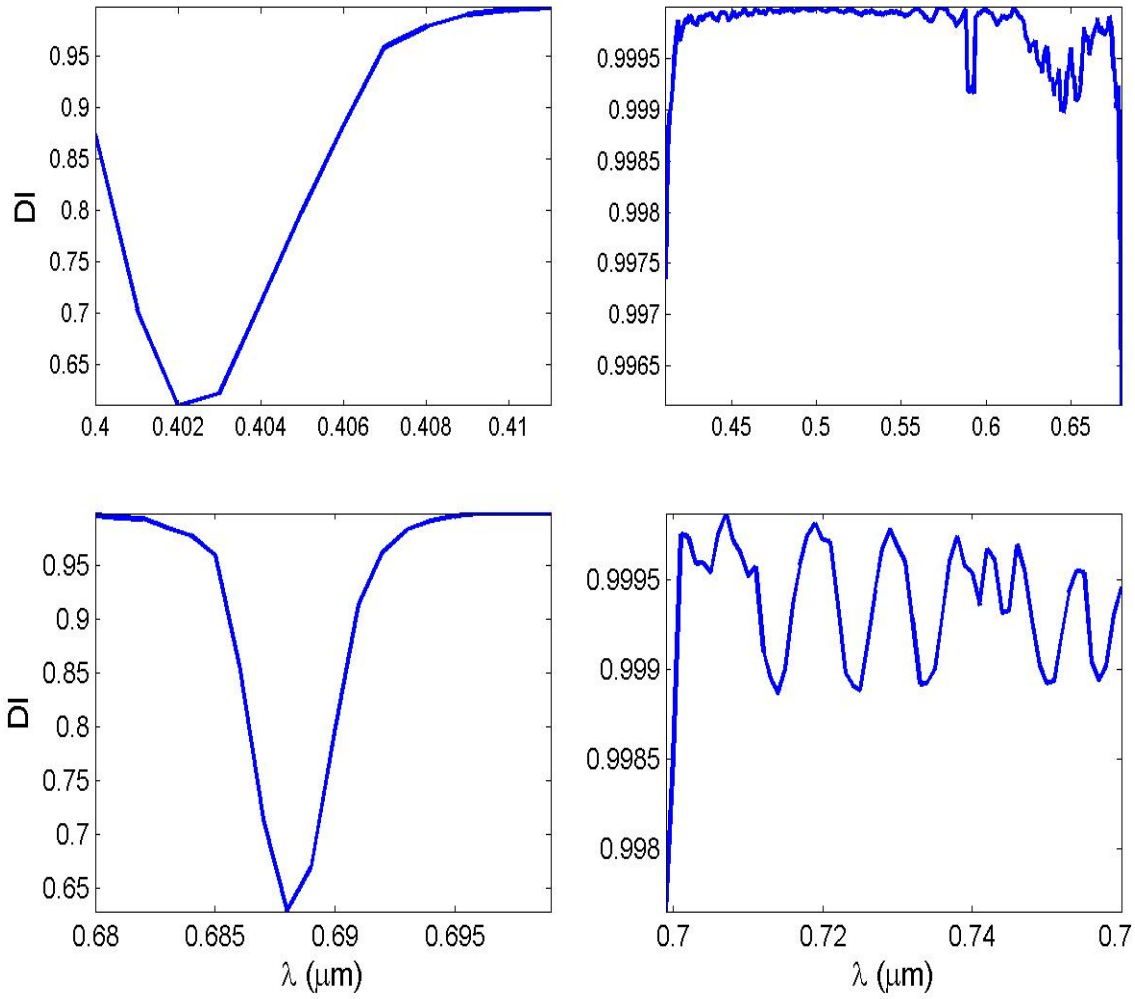

Figure 5.11: Spectral bandwidth depolarization index as a function of wavelength.

The result of Figure 5.9 depicts the plot of the diattenuation versus wavelength for all wavelengths of the visible spectrum. It can be seen that the diattenuation property of the volume hologram is reduced in the wavelength ranges between 450 nm and 650 nm. This reduction is due to the fact that, in the initial design of the volume, the refractive modulation within the active region of the hologram is optimized to produce high diffraction efficiency independent of the polarization state of the incident beam. The diattenuation property of the hologram increases for wavelengths lower than 450 nm and for wavelengths higher than 680 nm. There are also two wavelengths where the diattenuation is exactly zero, which means that all incident polarization is transmitted with equal loss. Figures 5.10 and 5.11 show the plots of the depolarization index of the volume hologram, due to the spectral band limitation. The plots shows that depolarization effects from the spectral bandwidth, particularly for $\Delta\lambda = 5nm$, is close to one. However if one includes all depolarization factors into the coherent Mueller matrix, the depolarization index will decrease.

5.5 Conclusion:

As a conclusion to the polarimetric characterization, we can say that although the simulation of the Mueller matrix of the volume hologram did include all possible depolarization properties, we were able to show that the volume hologram does not only behave as diffractive optical element; it also behaves as a combination of a weak polarizer and a weak retarder. The polarization element nature of the volume hologram is the result of several factors that include the lamellar structure in the active region of grating, and the chemical development of the holographic optical element.

Chapter 6

Conclusion and Future Work

The work in this dissertation focused more into the development of a transmission volume holographic phase grating that will provide at least 70% efficiency for all wavelengths in the visible region of the electromagnetic spectrum. This volume hologram is required to perform well independent of the polarization state of incident light. The design of the hologram has the intend of determining a refractive index modulation that will increase the diffraction efficiencies of visible wavelengths that are different than the Bragg wavelengths by optimization of the diffraction efficiencies of the first order of diffraction. A complete design, simulation, characterization, and measurements of the hologram's performance was done to help understand its overall performance. The content of the work presented in this dissertation may be summarized as:

- The architectural design parameters of the volume hologram were calculated based on Kogelnik's two wave coupled-wave analysis (Kogelnik, 1969).

- Simulation of the electromagnetic properties of the light diffracted in the first order of diffraction, mainly the transmission coefficients of the $\vec{\boldsymbol{E}}$-field and the diffraction efficiencies, are obtained using the rigorous coupled-wave analysis (Moharam and Gaylord, 1981; Moharam et al., 1995b,a); since this rigorous method does not use any approximation and takes consideration of the wavelength dependent absorption from BK7 cover glasses. The cover glasses' purpose

is to protect the holographic optical element from physical damages, dust, and humidity.

- Measurements of the physical thickness of the thin film and the diffraction efficiencies were also done to get a comparison between the experimental and simulated performance of the volume hologram.

- The Mueller matrix signature incorporating the depolarization properties resulting from spectral band limit were determined using the methods of Azzam and Bashara, Gil and Bernabeu, and Chipman (Azzam and Bashara, 1974, 1975; Azzam, 1986; Azzam and Bashara, 1977; Gil and Bernabeu, 1985; Chipman, 2005).

6.0.1 Summary of the Dissertation

A summary of prior work and application of the volume holographic gratings in several fields of science and engineering, and the motivation for the development of single volume hologram for use in multiple tasks within the visible region of the electromagnetic spectrum, was presented in the first chapter of this dissertation. Volume phase holograms have been used in optical and astronomical application (Wakayama et al., 2013; Barden et al., 1998; Bianco et al., 2012; Arns and Dekker, 2008) and have grown to be used in many other fields. To facilitate the application, and reduce the amount of cost we were lead into the development of a single transmission hologram for multi-disciplinary use within the entire visible spectrum. Most volume holograms are design based on Bragg's condition at one wavelength (Blanche et al., 2004) and others looked into the determination of a refractive index modulation based on an

unpolarized incident light (Baldry et al., 2004; Barden et al., 1998; Blais-Ouellette, 2004; Bianco et al., 2012; Arns and Dekker, 2008); but to our knowledge, none of them investigated a refractive index modulation that produces high diffraction efficiencies in the entire visible spectrum.

In Chapter 2 of this dissertation, review of the theory and concepts used for the design and simulations were given. The background theory and formulation chapter consists of three very important sections needed for the completion of this study.

- Kogelnik's Coupled-Wave Analysis
- The Rigorous Coupled-Wave Analysis
- Review of Polarization based on the generalized ellipsometry

A review of Kogelnik's two wave coupled-wave analysis (Kogelnik, 1969; Mihaylova, 2013a,b) which is derived based on the assumption that only two waves, the reference and signal waves, propagate does not incorporate the wavelength dependent absorption from the cover glasses. This method was used for the calculation of the design parameters as well as to determine the refractive index modulation required to produce the holographic optical element suitable for our design objectives. Although this method is used to determine the design parameters, it is not used to determine the actual electromagnetic properties of the diffracted light. In order to have a better understanding of the volume hologram's actual performance, it is important to do all simulations using an electromagnetic solution method that considers all factors and free of unnecessary approximation. There are several methods for solving the electromagnetic properties of meta-materials, volume holograms, and surface relief grating; however for the purpose of this dissertation, we have used the rigorous coupled-wave

analysis (RCWA) (Moharam and Gaylord, 1981; Moharam et al., 1995b,a; Gaylord and Moharam, 1982; Moharam et al., 1981; Gaylord and Moharam, 1981), which is the most commonly used and proved to perform better than others (Kogelnik, 1969). To complete the characterization and understanding of how the volume hologram works, a simulation of its polarization signature was required; thus in the last section of Chapter 2 a review of the generalized ellipsometry (Azzam and Bashara, 1974, 1975; Azzam, 1986; Azzam and Bashara, 1977), which helped to calculate the Mueller matrix signature of the hologram was introduced.

The complete simulation and characterization of the RGB transmission volume hologram was presented in Chapter 3. The RGB transmission volume hologram was designed such that it gives at least 70% diffraction efficiency for all wavelengths in the visible region of the electromagnetic spectrum, and a 98% theoretical diffraction efficiency when green light is incident. The spectral and angular responses in the first order of diffraction were calculated to determine the spectral and angular bandwidth.

Chapter 4 presented the recording and chemical development of the hologram, along with the measurements of the physical thicknesses and diffraction efficiecnies of the first two prototypes. It was determined that the thickness of the dichromated gelatin thin film was not uniform and its average thickness was almost double of the theoretical thickness. Using the measured thickness, a refractive index modulation of 0.017, and all other parameter kept the same, we were able to simulate the spectral response in the first order of diffraction that was close to the measured diffraction efficiencies as functions of wavelength, see Figure 4.9.

A review of the polarimetric response of the volume hologram was investigated in Chapter 5. The main reason behind the investigation into the polarization signature

of the hologram was due to the fact that the refractive index modulation within the active region would exhibit a form birefringence (Rytov, 1956; Born and Wolf, 1970; Yariv and Yeh, 1977; Kim et al., 1995; Rytov, 1956). Although the design parameters were determined with unpolarized incident plane wave, the form birefringence resulting from the lamellar structure due to the refractive index modulation would introduce a phase shift between the TE and TM polarization; hence it was determined that the hologram still has some effects on the polarization state of incident light.

6.0.2 Future Work Plan

The work done in this dissertation proved that it is possible to design a single volume hologram that can be used to do several tasks. We were also able to show that the structure of the refractive index modulation will create a phase shift between the TE and TM polarization components of incident light, which will result in a change of polarization state; however this design and characterization can be further expanded to include more depolarization properties to enhance the accuracy of the design and knowledge of the behavior of the hologram. The next step in this work, is to design, optimize, and write volume holograms by interfering two different waves, such as: plane and spherical waves and two spherical waves. We also want to develop our in house holography lab, and measure the complete polarization data using a Mueller matrix polarimeter.

References

Arns, J. A. and H. Dekker (2008). Slanted fringe volume phase holographic gratings in astronomical instrumentation. In *Society of Photo-Optical Instrumentation Engineers (SPIE) Conference Series*, volume 7014 of *Society of Photo-Optical Instrumentation Engineers (SPIE) Conference Series*, p. 1. doi:10.1117/12.788804.

Azzam, R. and N. Bashara (1977). *Ellipsometry and Polarized light*.

Azzam, R. M. A. (1986). Ellipsometric Methods of Characterization of Optical Thin Films. In Jacobsson, J. R. (ed.) *Thin Film Technologies II*, volume 652 of *Society of Photo-Optical Instrumentation Engineers (SPIE) Conference Series*, p. 198. doi: 10.1117/12.938378.

Azzam, R. M. A. and N. M. Bashara (1974). Application of generalized ellipsometry to anisotropic crystals. *Journal of the Optical Society of America (1917-1983)*, **64**, p. 128.

Azzam, R. M. A. and N. M. Bashara (1975). Application of generalized ellipsometry to anisotropic crystals (T). *Journal of the Optical Society of America (1917-1983)*, **65**, p. 462.

Baldry, I. K., J. Bland-Hawthorn, and J. G. Robertson (2004). Volume Phase Holographic Gratings: Polarization Properties and Diffraction Efficiency. *pasp*, **116**, pp. 403–414. doi:10.1086/383622.

Barden, S. C., J. A. Arns, and W. S. Colburn (1998). Volume-phase holographic gratings and their potential for astronomical applications. In D'Odorico, S. (ed.) *Optical Astronomical Instrumentation*, volume 3355 of *Society of Photo-Optical Instrumentation Engineers (SPIE) Conference Series*, pp. 866–876.

Bianco, A., J. Arns, H. Dekker, P. Spanò, A. Zanutta, and F. M. Zerbi (2012). Slanted VPHGs in astronomical instrumentation: tests and perspectives. In *Society of Photo-Optical Instrumentation Engineers (SPIE) Conference Series*, volume 8450 of *Society of Photo-Optical Instrumentation Engineers (SPIE) Conference Series*, p. 3. doi:10.1117/12.925389.

Billmers, L. (2015). Chemical processing procedures from RLA. In *RLA Writing Document*. RL Associates.

Blais-Ouellette, S. (2004). Holographic gratings for astronomy: atmospheric lines suppression and tunable filter. In Armitage, J. C., R. A. Lessard, and G. A. Lampropoulos (eds.) *Photonics North 2004: Photonic Applications in Astronomy, Biomedicine, Imaging, Materials Processing, and Education*, volume 5578 of *Society of Photo-Optical Instrumentation Engineers (SPIE) Conference Series*, pp. 23–28. doi:10.1117/12.567440.

Blanche, P.-A., P. Gailly, S. L. Habraken, P. C. Lemaire, and C. A. J. Jamar (2004). Volume phase holographic gratings: large size and high diffraction efficiency. *Optical Engineering*, **43**, pp. 2603–2612. doi:10.1117/1.1803557.

Born, M. and E. Wolf (1970). *Principles of optics. Electromagnetic theory of propagation, interference and diffraction of light*.

Bragg, W. L. (1912). The diffraction of short electromagnetic waves by a crystal. volume 7 of *Proc. Camb. Phil. Soc. B*, p. 43.

Campbell, G. (1994). What to do after the poster session. In *PhD Dissertation, The University of Arizona, Tucson. Arizona, 1994*. The University of Arizona, Optical Sciences.

Chang, B. J. and C. D. Leonard (1979). Dichromated gelatin for the fabrication of holographic optical elements. *ao*, **18**, pp. 2407–2417. doi:10.1364/AO.18.002407.

Chen, X., S. Liu, C. Zhang, H. Jiang, Z. Ma, T. Sun, and Z. Xu (2014). Accurate characterization of nanoimprinted resist patterns using Mueller matrix ellipsometry. *Optics Express*, **22**, p. 15165. doi:10.1364/OE.22.015165.

Chen, X., C. Zhang, and S. Liu (2013). Depolarization effects from nanoimprinted grating structures as measured by Mueller matrix polarimetry. *Applied Physics Letters*, **103**(15), 151605. doi:10.1063/1.4824760.

Chipman, R. A. (2005). Depolarization index and the average degree of polarization. *ao*, **44**, pp. 2490–2495. doi:10.1364/AO.44.002490.

Collin, R. E. and H. Chang (1960). Field Theory of Guided Waves. p. 368.

de Smet, D. J. (1975). Application of generalized ellipsometry to anisotropic crystals (T). *Journal of the Optical Society of America (1917-1983)*, **65**, p. 461.

Denisyuk, Y. N. (1963). On the reproduction of the optical properties of an object by wave field of its scattered radiation, Part I. *Opt. Spect*, **15**, p. 279.

Gabor, D. (1949). Microscopy by reconstructed wavefronts. volume 197 of *Proc. R. Soc. A*, pp. 454–487.

Gaylord, T. K. and M. G. Moharam (1981). Thin and thick gratings: terminology clarification. *ao*, **20**, pp. 3271–3273. doi:10.1364/AO.20.003271.

Gaylord, T. K. and M. G. Moharam (1982). Planar dielectric grating diffraction theories. *Applied Physics B: Lasers and Optics*, **28**, pp. 1–14. doi:10.1007/BF00693885.

Gil, J. J. and E. Bernabeu (1985). A Depolarization Criterion in Mueller Matrices. *Optica Acta*, **32**, pp. 259–261. doi:10.1080/713821732.

Kim, T. J., G. Campbell, and R. K. Kostuk (1995). Volume holographic phase-retardation elements. *Optics Letters*, **20**, pp. 2030–2032. doi:10.1364/OL.20.002030.

Kogelnik, H. (1969). Coupled wave theory for thick hologram gratings. *The Bell System Technical Journal, Vol. 48, no. 9, November 1969, pp. 2909-2947*, **48**, pp. 2909–2947.

Lippmann, G. (1897). Sur la theorie de la photographie des couleurs simples et composees par la method interferentielle. *J. Physique*, **3**, pp. 97–107.

Markova, B., D. Nazarova, and P. Sharlandjiev (2011). Control of the spectral position of dichromated gelatin reflection holograms. *ao*, **50**, p. 5534. doi:10.1364/AO.50.005534.

Mihaylova, E. (2013a). Holography - Basic Principles and Contemporary Applications. In Mihaylova, E. (ed.) *InTech*, pp. 3–36.

Mihaylova, E. (2013b). Holography - Basic Principles and Contemporary Applications. In Mihaylova, E. (ed.) *InTech*, pp. 37–60.

Moharam, M. G. and T. K. Gaylord (1981). Rigorous coupled-wave analysis of planar-grating diffraction. *Journal of the Optical Society of America (1917-1983)*, **71**, p. 811.

Moharam, M. G., T. K. Gaylord, and R. Magnusson (1981). Planar Grating Diffraction: Multiwave Coupled-Wave Theory And Modal Theory. In Chi, C. H., E. G. Loewen, and C. L. O'Bryan (eds.) *Society of Photo-Optical Instrumentation Engineers (SPIE) Conference Series*, volume 240 of *Society of Photo-Optical Instrumentation Engineers (SPIE) Conference Series*, pp. 132–138. doi:10.1117/12.965647.

Moharam, M. G., E. B. Grann, D. A. Pommet, and T. K. Gaylor (1995a). Formulation for stable and efficient implementation of the rigorous coupled-wave analysis of binary gratings. *Journal of the Optical Society of America A*, **12**, pp. 1068–1076. doi:10.1364/JOSAA.12.001068.

Moharam, M. G., D. A. Pommet, E. B. Grann, and T. K. Gaylord (1995b). Stable implementation of the rigorous coupled-wave analysis for surface-relief gratings: enhanced transmittance matrix approach. *Journal of the Optical Society of America A*, **12**, pp. 1077–1086. doi:10.1364/JOSAA.12.001077.

Newell, J. C., L. Solymar, and A. A. Ward (1985). Holograms in dichromated gelatin: real-time effects. *ao*, **24**, pp. 4460–4467. doi:10.1364/AO.24.004460.

Newell, J. C. W. (1987). Optical Holography in Dichromated Gelatin. In *PhD Thesis, University of Oxford, Hilary Term, 1987*. University of Oxford.

Otani, Y. (2009). Mueller matrix polarimeter for nano-structure measurement. *CLEO Pacific Rim*, **282**.

Rytov, S. M. (1956). Electromagnetic Properties of Finely Stratified Medium. *Sov. Phys. JETP*, **2**(3), pp. 466–475.

Schutte, H. and C. G. Stojanoff (1997). Effects of process control and exposure energy upon the inner structure and the optical properties of volume holograms in dichromated gelatin films. In Benton, S. A. and T. J. Trout (eds.) *Practical Holography XI and Holographic Materials III*, volume 3011 of *Society of Photo-Optical Instrumentation Engineers (SPIE) Conference Series*, pp. 255–266. doi: 10.1117/12.271361.

Shankoff, T. A. (1968). Phase holograms in dichromated gelatin. *ao*, **7**, p. 2101. doi:10.1364/AO.7.002101.

Sheel, D. W. (1990). Dichromated gelatin for holographic optical elements. In Benton, S. A. (ed.) *Practical Holography IV*, volume 1212 of *Society of Photo-Optical Instrumentation Engineers (SPIE) Conference Series*, pp. 2–12.

Sobolev, G. A. and S. B. Soboleva (1994). Properties and processing of the layers of dichromated gelatin for holography. In Jeong, T. H. (ed.) *Holographic Imaging and Materials*, volume 2043 of *Society of Photo-Optical Instrumentation Engineers (SPIE) Conference Series*, pp. 207–216.

Stojanoff, C. G. (1997). Review of the technology for the manufacturing of large-format DCG holograms for technical applications. In Benton, S. A. and T. J.

Trout (eds.) *Practical Holography XI and Holographic Materials III*, volume 3011 of *Society of Photo-Optical Instrumentation Engineers (SPIE) Conference Series*, pp. 267–278. doi:10.1117/12.271375.

Stojanoff, C. G., O. Brasseur, S. Tropartz, and H. Schuette (1994). Conceptual design and practical implementation of dichromated gelatin films as an optimal holographic recording material for large-format holograms. In Lessard, R. A. (ed.) *Photopolymers and Applications in Holography, Optical Data Storage, Optical Sensors, and Interconnects*, volume 2042 of *Society of Photo-Optical Instrumentation Engineers (SPIE) Conference Series*, pp. 301–311. doi:10.1117/12.166349.

Stojanoff, C. G., H. Schuette, O. Brasseur, R. Kubitzek, and S. Tropartz (1991). Photochemical and thermal treatment of dichromated gelatin film for the manufacturing of holographic optical elements for operation in the IR. In Lessard, R. A. (ed.) *Photopolymer Device Physics, Chemistry, and Applications II*, volume 1559 of *Society of Photo-Optical Instrumentation Engineers (SPIE) Conference Series*, pp. 321–330. doi:10.1117/12.50682.

Tholl, H. D., M. Dohmen, and C. G. Stojanoff (1995). Determination of the mean refractive index and the thickness of dichromated gelatin holographic films using the thin film resonance method. In Trout, T. J. (ed.) *Holographic materials*, volume 2405 of *Society of Photo-Optical Instrumentation Engineers (SPIE) Conference Series*, pp. 76–87. doi:10.1117/12.205351.

Tropartz, S., O. Brasseur, R. Kubitzek, and C. G. Stojanoff (1991). Development and investigation of dichromated gelatin film for the fabrication of large-format holograms operating at 400-900 nm. In Morris, G. M. (ed.) *Holographic Optics III: Principles and Applications*, volume 1507 of *Society of Photo-Optical Instrumentation Engineers (SPIE) Conference Series*, pp. 345–353. doi:10.1117/12.47055.

Wakayama, Y., A. Okamoto, K. Kawabata, A. Tomita, and K. Sato (2013). Mode demultiplexer using angularly multiplexed volume holograms. *Optics Express*, **21**, p. 12920. doi:10.1364/OE.21.012920.

Yariv, A. and P. Yeh (1977). Electromagnetic propagation in periodic stratified media. II - Birefringence, phase matching, and X-ray lasers. *Journal of the Optical Society of America (1917-1983)*, **67**, pp. 438–448.

Yeh, P., A. Yariv, and C.-S. Hong (1977). Electromagnetic propagation in periodic stratified media. I - General theory. *Journal of the Optical Society of America (1917-1983)*, **67**, pp. 423–438.